國立臺灣大學工學院工程科學及海洋工程學系

碩士論文

Department of Engineering Science and Ocean Engineering

College of Engineering

National Taiwan University

Master's Thesis

15 MW 半潛式浮式風機系統新竹外海場址性能預測

Performance Prediction of a 15 MW Semi-Submersible Floating Wind Turbine System in the Hsinchu Offshore Area

蔡博彥

Po-Yen Tsai

指導教授：趙修武 博士

Advisor: Dr.-Ing. Shiu-Wu Chau

中華民國 113 年 7 月

July, 2024

doi:10.6342/NTU202403052

doi:10.6342/NTU202403052

Abstract

This study explores the operational performance and capacity factor of a semi-submersible TaidaFloat platform featuring an IEA 15-MW offshore wind turbine and a 3×3 mooring configuration in the Hsinchu offshore area. Hydrodynamic properties are predicted using Ansys Aqwa and STAR-CCM+, while OrcaFlex is employed to estimate mooring loads, predict wind turbine aerodynamics, and solve motion equations for evaluating motion response, power output, and dynamic responses of the mooring system and wind turbine. Assuming alignment between wave and wind directions, the potential flow method (P) and two viscous methods are utilized to calculate the hydrodynamic properties of the studied FOWT system for predicting its operational performance under common and extreme wave conditions. Statistical analysis is used to bluid the scatter diagram of long-term conditions off Hsinchu for comparing hydrodynamic properties using both potential and viscous methods under a constant wind speed and API spectrum. The simulations reveal that the motion response of the platform is underestimated with the sigle-point method, where the motion magnitude is related to damping at the wave spectral density peak under specific metocean conditions. Under the extreme condition, the maximum offset using the fully viscous method is 8.293 m, with the highest mooring line tension at 6.519 MN. For long-term conditions, maximum values of motion response and mooring line tension were generally higher with the API wind spectrum compared to a constant wind speed. Employing the API wind spectrum and the fully viscous method, the annual average capacity factor was found to be 0.512, differing by 1.8% from the theoretical value.

Keywords: Floating Offshore Wind Turbine, Semi-Submersible, Motion Response, Hydrodynamic Properties, Mooring Line Tension, Capacity Factor, Taiwan Strait

doi:10.6342/NTU202403052

摘要

本研究探討在新竹外海地區使用半潛式臺大浮台、IEA 15-MW 離岸風機以及3×3 型式繫纜佈置之浮式風機系統的運轉性能及年平均發電功率。先以 Ansys Aqwa 和 STAR-CCM+預測了水動力特性，再使用 OrcaFlex 預測繫纜受力及風機的空氣動力，最後通過運動方程式求解浮式風機系統的運動響應及發電功率。本研究假設波向與風向相同，使用了勢流方法及兩種黏性流方法預測水動力，計算在一般海況及極端條件下條件下的風機系統性能；對統計新竹外海長期的波況機率分佈，比較勢流與黏性流方法預測的下的水動力特性以及使用固定風速和 API 風譜的風機系統性能。模擬結果顯示，浮台的運動在使用單點黏性流方法下皆有低估的結果，並發現運動的大小與該海況的波能量尖峰處的阻尼大小相關。在極端海況下，使用全域黏性流方法的最大位移為 8.293 m；最大纜繩張力為 6.519 MN。在長期的情況下，使用 API 風譜的運動響應及繫纜張力最大值一般高於使用固定風速。在使用 API 風譜與全域黏性流方法的情況下，年平均容量因子可達 0.512，與理論值相差 1.8%。

關鍵字：浮式風機、半潛式浮台、運動響應、水動力特性、纜繩張力、容量因子、台灣海峽

doi:10.6342/NTU202403052

doi:10.6342/NTU202403052

Content

doi:10.6342/NTU202403052

doi:10.6342/NTU202403052

Nomenclature

Latin Symbols

A	Disk area	[m^2]
A_{ij}	Added mass in translation/rotation	[kg]/[kg·m^2/rad]
A_k	Predicted added mass in translation/rotation	[kg]/[kg·m^2/rad]
a	Axial induction factor	[-]
a	Area vector	[m^2]
a'	Angular velocity induction factor	[-]
a_{ex}	External cross-sectional stress area	[m^2]
a_{in}	Internal cross-sectional stress area	[m^2]
a_w	Amplitude of the incident wave	[m]
B_{ij}	Damping in translation/rotation	[N·s/m]/[N·m·s/rad]
B_k	Predicted damping in translation/rotation	[N·s/m]/[N·m·s/rad]
B_w	Wave direction	[rad]
C_d	Drag coefficient	[-]
C_{ij}	Stiffness of floating body in translation/rotation	[N/m]/[N·m/rad]
C_k	Stiffness of floating body in translation/rotation	[N/m] /[N·m/rad]
C_l	Lift coefficient	[-]
C_α	Sharpening factor	[-]
C_θ	Angle factor	[-]
$CD_{k\omega}$	Cross-diffusion coefficient	[-]
CG	Center of gravity of wind turbine system	[m]
Co	Courant number	[-]
c	Chord length of blade section	[m]
c_c	Critical damping value for segment	[s]
c_d	Damping for mooring line	[s]
D	Wave drift amplitude	[m]
d	Distance to wall	[m]
EA	Axial stiffness of line	[N]
F_a	Axial force	[N]
F_d	Force/Moment generated by diffracting wave	[N]/[N·m]
F_E	Wave exciting force/moment	[N]/[N·m]
$\bar{F}_{E,1}^{(2)}$	Second-order wave exciting force in x direction	[N]
$\bar{F}_{E,2}^{(2)}$	Second-order wave exciting force in y direction	[N]
F_I	Froude-Krylov force/moment	[N]/[N·m]
F_o	Total force acting on the floater	[N]/[N·m]
$F_{o,i}$	Force/Moment other than fluid force	[N]/[N·m]

doi:10.6342/NTU202403052

F_r	Radiation force	[N]
F_t	Tangential force	[N]
f	Wave frequency	[1/s]
f_p	Wave angular peak frequency	[1/s]
G	Green's function	[1/m]
GK	Dimensionless gain correction factor	[-]
g	Gravitational acceleration	[m/s^2]
g_i	Gravity component in i-direction	[m/s^2]
H_h	Hub height	[m]
H_s	Significant wave height	[m]
h	Water depth	[m]
I	Moment of inertia	[kg·m^2]
I_d	Drivetrain inertia	[kg·m^2]
I_g	Generator inertia	[kg·m^2]
I_r	Rotor inertia	[kg·m^2]
I_z	Turbulence intensity	[-]
J_o	Bessel function of the first kind	[m^2]
K_d	Blade-pitch controller derivative gain	[m^2]
K_i	Blade-pitch controller integral gain	[-]
K_p	Blade-pitch controller proportional gain	[s]
k	Turbulent kinetic energy	[J]
k_{tt}	Coefficient for torque coupling tension	[N·m/°]
k_w	Wave number	[1/m]
L	Characteristic length	[m]
l	Segment length	[m]
l_0	Initial segment length	[m]
M	Floating body mass	[kg]
$\bar{M}_{E,6}^{(2)}$	Second-order wave exciting force in the direction of rotation around the z-axis	[N·m]
m	Segment mass	[kg]
N	Number of fluids	[-]
N_p	Number of panels over immersed body surface	[-]
N_g	High-speed to low-speed gearbox ratio	[-]
n	Discrete-time-step counter	[-]
$\mathbf{n}$	Normal vector	[-]
n_b	Number of blades	[-]
P_0	Rated mechanical power	[W]
P_1	Pressure before actuator disk	[Pa]
P_2	Pressure behind actuator disk	[Pa]
P_g	Generator power	[W]
P^m	Mean value of generator power	[W]

doi:10.6342/NTU202403052

P_{in}	Fluid pressure before system	[Pa]
P_{out}	Fluid pressure behind system	[Pa]
$\bar{p}$	Mean fluid pressure in viscous flow	[Pa]
p_{ex}	External pressure	[Pa]
p_{in}	Internal pressure	[Pa]
Q	Moment	[N·m]
Q_d	Wave drift QTF in translation/rotation	[N/m^2]/[N/m]
RAO_i	Response amplitude operator in translation/rotation	[m/m]/[°/m]
R	Blade length	[m]
R_r	Rotor radius	[m]
R_w	Flow field radius	[m]
r	Cross section radius	[m]
r_h	Hub radius	[m]
$\mathbf{S}$	Mean strain rate tensor	[1/s]
S_0	Mean immersed area of floating body	[m^2]
S_A	Wind spectral density	[m^2/Hz]
T	Wave period	[s]
T_a	Low-speed shaft aerodynamic torque	[N·m]
T_e	Effective tension	[N]
T_g	High-speed shaft generator torque	[N·m]
T_i^M	Maximum value of mooring line tension	[N]
T_i^m	Mean value of mooring line tension	[N]
T_p	wave peak period	[s]
T_r	Thrust force	[N]
T_s	Discrete time step	[s]
T_w	Wall tension	[N]
T_z	Zero-crossing period	[s]
t	Time	[s]
U_1	Flow velocity before system	[m/s]
U_2	Flow velocity behind system	[m/s]
U_{10}	Wind speed 10 m above the mean sea level	[m/s]
U_{hub}	Wind speed at the hub height	[m/s]
U_{in}	Inflow velocity	[m/s]
U_{out}	Outflow velocity	[m/s]
U_w	Wind speed at hub height	[m/s]
$u_{f,n}$	Unfiltered generator speed	[rad/s]
$\bar{u}_i$	Mean velocity component in i-direction	[m/s]
u_i'	Turbulent velocity component in i-direction	[m/s]
V	Cell Volume	[m^3]
V_c	Characteristic velocity	[m/s]

doi:10.6342/NTU202403052

V_f	Forced motion velocity in translation/rotation	[m/s]/[°/s]
V_i	Volume of the i-th fluid in a cell	[m^3]
$\mathbf{v}$	Flow field velocity	[m/s]
$\bar{\mathbf{v}}$	Mean velocity	[m/s]
$\mathbf{v}_{c,i}$	Boundary sharpening velocity of the i-th fluid	[m/s]
$\mathbf{v}_{d,i}$	Diffusion velocity of the i-th fluid	[m/s]
x_i	Displacement in i-direction	[m]/[°]
$\dot{x}_i$	Velocity in i-direction	[m/s]/[°/s]
$\ddot{x}_i$	Acceleration in i-direction	[m/s^2]/[°/s^2]
x_k	Generalized displacement in translation/rotation	[m]/[°]
$y_{f,n}$	Filtered generator speed	[rad/s]
z_i	Coordinate	[m]

doi:10.6342/NTU202403052

Greek Symbols

α	Angle of attack	[°]
α_i	Volume fraction of the i-th fluid	[-]
α_c	Volume fraction of central cell	[-]
α_d	Volume fraction of downwind cell	[-]
α_f	Low-pass filter coefficient	[-]
α_f^{HRIC}	Modified volume fraction at cell interface	[-]
α_u	Volume fraction of upwind cell	[-]
α_w	Angle of incident wave	[°]
β_b	Blade pitch angle	[°]
$\beta_{b,k}$	Blade pitch angle when pitch sensitivity has doubled from its value at rated operating point	[°]
$\Delta\beta_b$	Small perturbation of blade pitch angle	[°]
γ	Parameter of the JONSWAP spectrum	[-]
ζ	Amplitude of forced motion in translation/rotation	[m]/[°]
ζ_φ	Damping ratio	[-]
η_i^M	Maximum value of translation/rotation	[m]/[°]
η_i^m	Mean value of translation/rotation	[m]/[°]
θ	Relative inflow angle	[°]
θ_p	Angle between fluid interface and cell interface	[°]
θ_w	Wind/wave direction	[°]
λ_a	Target tension damping	[-]
λ_s	Expansion factor of segment	[-]
μ	Viscosity	[kg/(m·s)]
μ_i	Fluid viscosity of the i-th fluid	[kg/(m·s)]
μ_t	Eddy viscosity	[kg/(m·s)]
ν	Kinematic viscosity	[m^2/s]
ν_P	Poisson ratio	[-]
$\boldsymbol{\xi}$	Position of a source	[m]
ξ_c	Normalized volume fraction of central cell	[-]
ξ_f	Normalized volume fraction at cell interface	[-]
ξ_f^*	Normalized volume fraction modified by Courant number	[-]
ξ_f^{**}	Normalized volume fraction modified by angle	[-]
ρ	Fluid density	[kg/m^3]
ρ_i	Fluid density of the i-th fluid	[kg/m^3]
σ	Local solidity	[m]
σ_p	Standard deviation of generator power	[W]
σ_{T_i}	Standard deviation of mooring line tension	[N]
σ_{η_i}	Standard deviation of translation/rotation	[m]/[°]

doi:10.6342/NTU202403052

τ	Segment twist angle	[°]
τ_{ij}	Shear stress	[Pa]
Φ	Unit amplitude of velocity potential	[m^2/s]
$\mathbf{\Phi}$	Velocity potential	[m^2/s]
Φ_d	Diffraction wave velocity potential	[m^2/s]
Φ_i	Unit amplitude of first-order incident wave velocity potential	[m^2/s]
Φ_r	Radiation velocity potential	[m^2/s]
φ	Phase lag	[s]
Ω	Low-speed shaft rotational speed	[rad/s]
Ω_0	Low-speed shaft rated rotational speed	[rad/s]
Ω_r	Rotor speed	[rad/s]
$\Delta\dot{\Omega}$	Low-speed shaft rotational acceleration	[rad/s^2]
ω	Specific turbulence dissipation rate	[1/s]
ω'	Induced angular frequency	[rad/s]
ω_0	Incident wave frequency	[rad/s]
ω_a	Angular frequency	[rad/s]
ω_s	Corner frequency	[rad/s]
ω_n	Natural frequency	[rad/s]

doi:10.6342/NTU202403052

List of Figures

doi:10.6342/NTU202403052

doi:10.6342/NTU202403052

List of Tables

doi:10.6342/NTU202403052

doi:10.6342/NTU202403052

1 Introduction

1.1 Motivation

In recent years, the rise in fossil fuel prices and energy supply shortages have made the development of renewable energy a global priority. Wind energy, a rapidly growing industry, plays a crucial role in reducing reliance on fossil fuels and decreasing pollution from thermal power generation. According to the World Wind Energy Association (WWEA) [1], there was a 38% increase in new installations in the first half of 2023 compared to 2022. This growth in wind power installation capacity highlights the expanding potential of the wind energy sector, as shown in Fig. 1, which illustrates the cumulative wind power capacity worldwide.

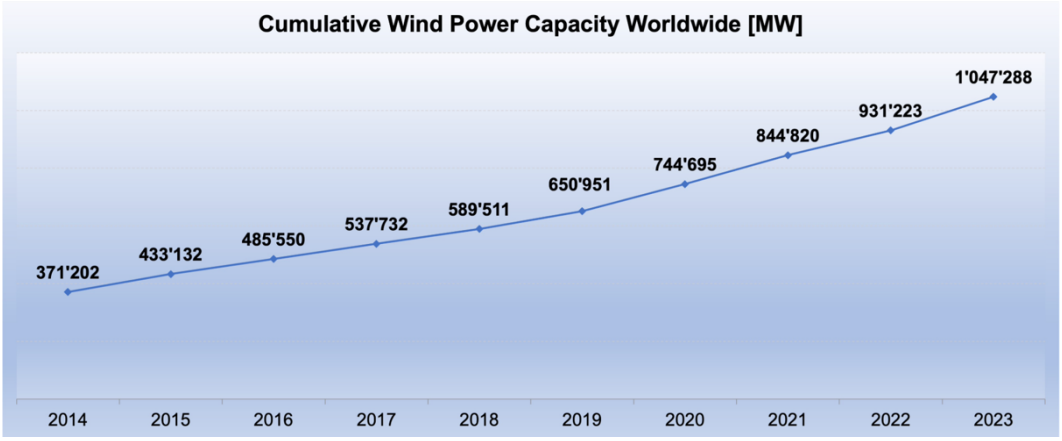

Figure 1 Global cumulative wind power capacity [1]

The Taiwan Strait is known for its rich wind resources. Zhang et al. [2] categorized global wind energy potential into seven levels, with the Taiwan Strait ranked at the highest. Chang et al. [3] reported that wind speeds in the Taiwan Strait at 100 m above mean sea level (MSL) range from 9.32 m/s to 11.24 m/s, and wind power densities vary from 1079 W/m^2 to 2665 W/m^2. Figure 2 and 3, taken from a technical report [4], show the annual

doi:10.6342/NTU202403052

average wind speeds and wind power densities in Taiwan at 80 m above MSL, highlighting the significant potential for wind power generation.

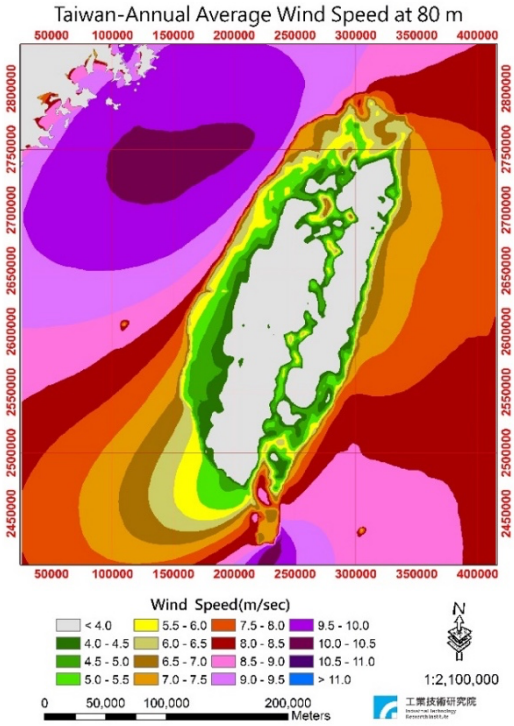

Figure 2 Annual average wind speed at 80 m above MSL in Taiwan.

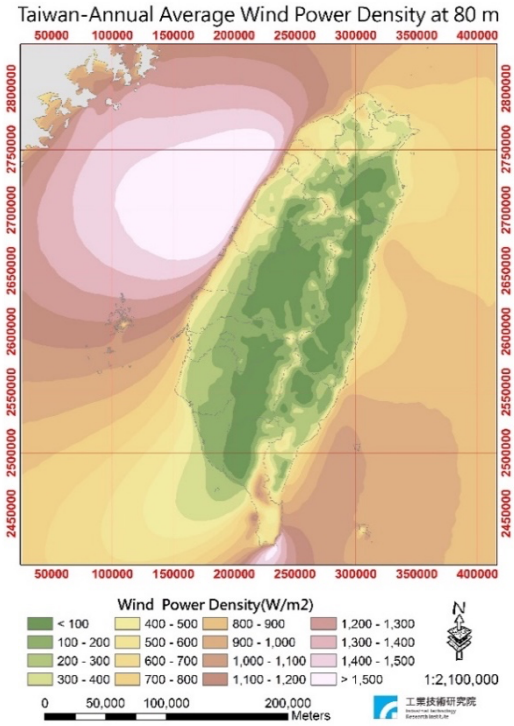

Figure 3 Annual average wind power density at 80 m above MSL in Taiwan

doi:10.6342/NTU202403052

Figure 4 illustrates that the areas with the highest wind potential in the Taiwan Strait are predominantly in deeper waters, suggesting that floating offshore wind turbines (FOWT) might offer an economical solution for deep-water installations, underscoring the necessity of examining the performance of floating offshore wind turbines. This research aims to assess the long-term motion response, mooring line tension, and annual average power output of a FOWT system, integrating the TaidaFloat platform [5], an IEA 15 MW offshore wind turbine, and a 3×3 mooring configuration. The evaluation takes into account meteorological and oceanic conditions over a decade in the Hsinchu offshore region.

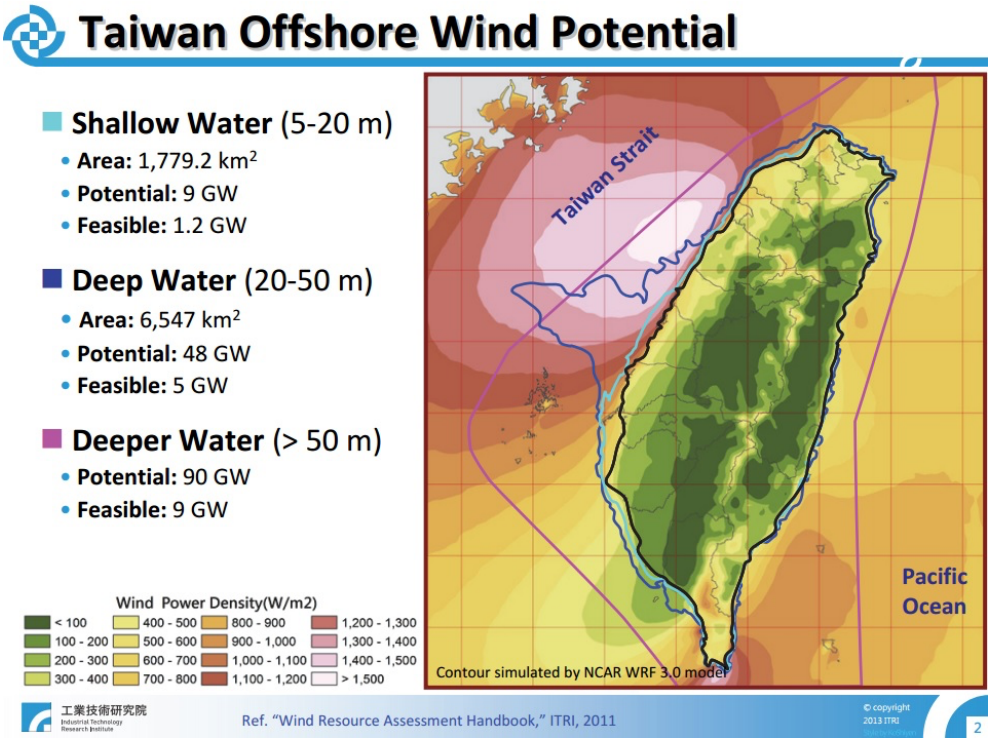

Figure 4 Potential for offshore wind energy in Taiwan

doi:10.6342/NTU202403052

1.2 Literature Review

In 1972, Heronemus [6] first proposed using floating wind turbines to harness wind power. Later, in 1990, World Wind [7] built and commissioned the first offshore wind turbine, with a capacity of 220 kW, in the offshore region of Sweden. Between 1991 and 2008, the capacity of offshore wind power installations in Europe increased steadily, mainly focusing on bottom-fixed wind turbines [8]. Research into floating offshore wind farms commenced in 1990 [8]-[10], resulting in their first installation and operation of FOWTs by 2008 [11].

Previous research has explored the performance of various platform types designed for FOWT, primarily classified into spar buoy, tension leg platform (TLP), and semi-submersible platforms. These platforms differ in their dependences to buoyancy and stability. Lee, Huang, and Wang [12]-[14] have studied the motion response of spar-type platforms. Li et al. [15] assessed and compared the hydrodynamic and motion responses of spar, semi-submersible, and TLP platforms in the South China Sea, concluding that spar-type platforms are generally more suitable for deeper waters. Conversely, the relatively shallow waters of the Taiwan Strait with depth from 50 m to 70 m, make semi-submersible platforms more suitable due to their depth requirements. Additionally, previous research on FOWTs in the Taiwan Strait primarily used the NREL 5-MW [16] and the DTU 10-MW [17] models. However, as larger turbines become more common, employing the IEA 15 MW offshore model [18] in research within the Taiwan Strait has only recently commenced.

Chen [19] evaluated the motion response and generator power of four different floating platforms under the metocean conditions of the Hsinchu offshore area and developed a robust numerical framework. Ansys Aqwa utilizes potential flow theory to

doi:10.6342/NTU202403052

compute hydrodynamic properties, while STAR-CCM+ simulates the forced motion of platforms to account for hydrodynamic properties with viscous effects. OrcaFlex uses blade element momentum theory and finite element methods to calculate the aerodynamics and dynamics of the mooring system. The integration of these tools allows for solving equations of motion to predict the motion response and generator power of the wind turbine system.

Building on this framework, Hong [20] investigated a disk-type semi-submersible FOWT using a 13.2 MW wind turbine in the Hsinchu offshore area of the Taiwan Strait. Kou [21] examined how three semi-submersible platform designs impact operational performance in the same region. Tong [22] forecasted the performance of a 15 MW FOWT system using the semi-submersible TaidaFloat and an IEA 15 MW wind turbine with a 3×2 mooring configuration in the Hsinchu offshore area, analyzing their performance under two normal operating conditions: common wave (CW) and high wave (HW). Cai [23] assessed the performance of 3×2 and 3×3 mooring arrangements for FOWT systems that utilize the semi-submersible TaidaFloat and IEA 15 MW wind turbines, particularly under extreme wave (EW) condition with a 50-year return period in the Hsinchu offshore area. This research emphasizes the annual average power output and long-term motion behavior of a 15 MW semi-submersible FOWT system in Hsinchu, considering different metocean conditions.

doi:10.6342/NTU202403052

2 Wind Turbine System Design

2.1 Floating Platform Design

This research concentrates on the TaidaFloat platform, a semi-submersible floating structure to support 15 MW wind turbines. According to the design criteria detailed in references [5] and [24], the TaidaFloat platform must not exceed a length of 85 m to facilitate construction in a Taiwanese shipyard's dry dock.

The TaidaFloat platform boasts a delta-shaped semi-submersible configuration with three cylindrical columns. The central column, which supports the wind turbine, is about 60% wider than the other two. The platform measures 81.6 m in characteristic length, is 35 m tall, and has a draft of 20 m. It has a total displacement of 21,222 tons, with its center of gravity positioned 1.961 m below the free surface and offset by 4.9429 m along the positive *x*-axis. Detailed specifications of the FOWT is listed in Table 1 and dimensions of the TaidaFloat is depicted in Fig. 5.

Table 1 Specifications of the FOWT

Draft (m)		20
Total System Displacement (t)		21222
CG (m)		(4.9429, 0, -1.961)
Principal Inertias about CG (kg·m^2)	I_{xx}	5.900×10^{10}
	I_{yy}	6.144×10^{10}
	I_{zz}	2.753×10^{10}
	I_{xy}	1.470×10^{7}
	I_{xz}	-1.121×10^{10}
	I_{yz}	7.538×10^{6}

doi:10.6342/NTU202403052

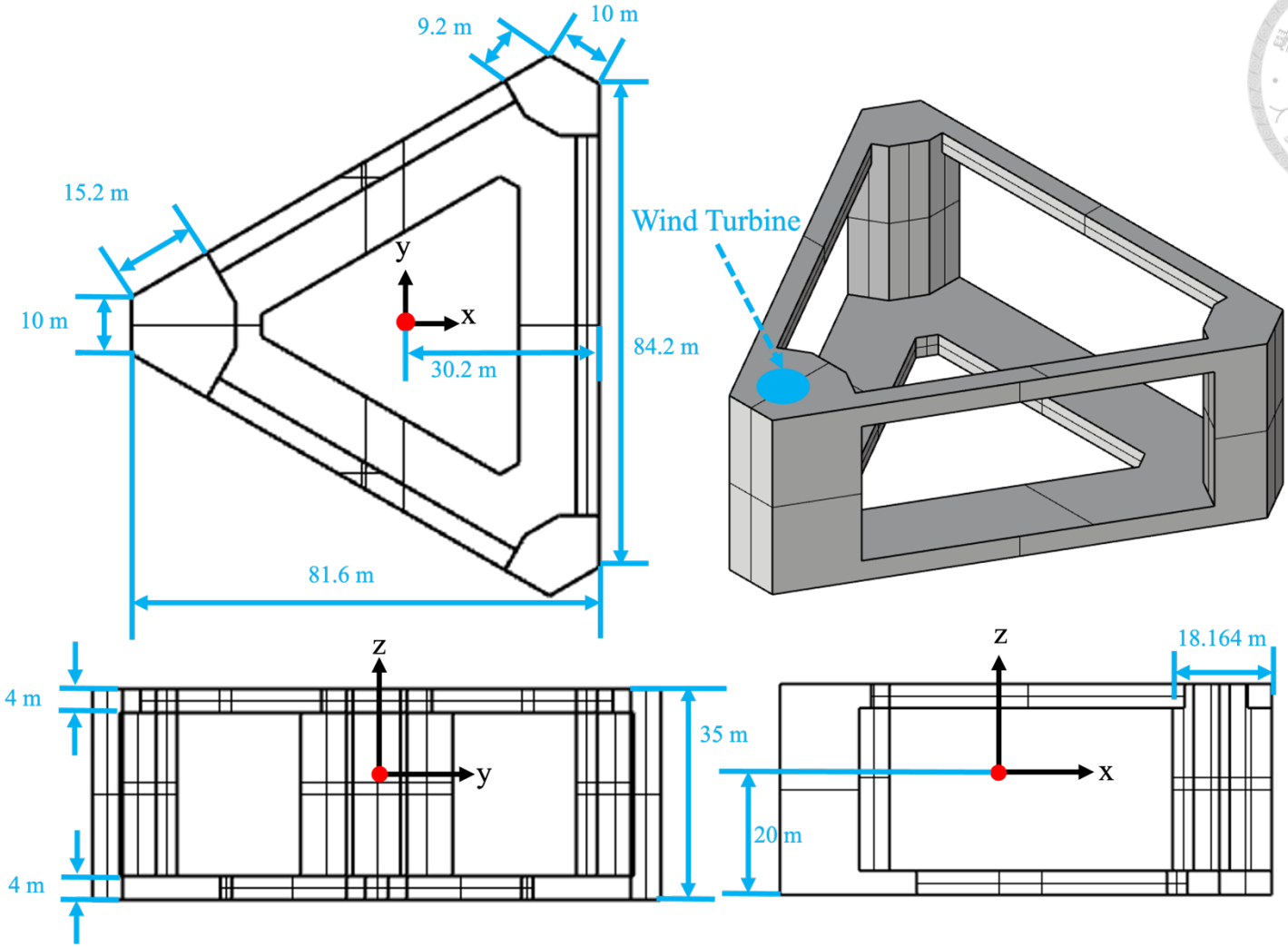

Figure 5 Dimensions of the TaidaFloat platform

doi:10.6342/NTU202403052

2.2 Mooring Design

The catenary mooring system relies on the weight of the mooring lines or chains to provide restoring force, while the taut mooring system maintains stability through the high vertical tension of mooring lines. Since semi-submersible platforms are better suited to catenary mooring systems [25], this approach was selected for the mooring design in this study.

In the 3x3 mooring arrangement, each column is connected to three cables 18 m below the free surface. The water depth is set at 70 m, with an anchor radius of 840 m, and the angle between adjacent mooring lines is 10º. To reduce the maximum tension and enhance the restoring force, each mooring line is fitted with ten 5-ton clump weights between the radii of 241 m and 268 m. Table 2 provides the specifications of the mooring design, which has a minimum breaking load (MBL) of 25.49 MN. Figure 6 depicts the mooring design.

Table 2 Specifications of the mooring design

Number of Mooring Lines	3×3
Angle between Adjacent Lines (°)	10
Depth to Anchors below SWL (m)	70
Depth to Fairleads below SWL (m)	18
Unstretched Mooring Line Length (m)	796
Mooring Line Diameter (m)	0.2466
Mooring Line Mass Density (kg/m)	375
Mooring Line Break Load (MN)	18.85
Number of Clumps	10
Clump Mass (t)	5

doi:10.6342/NTU202403052

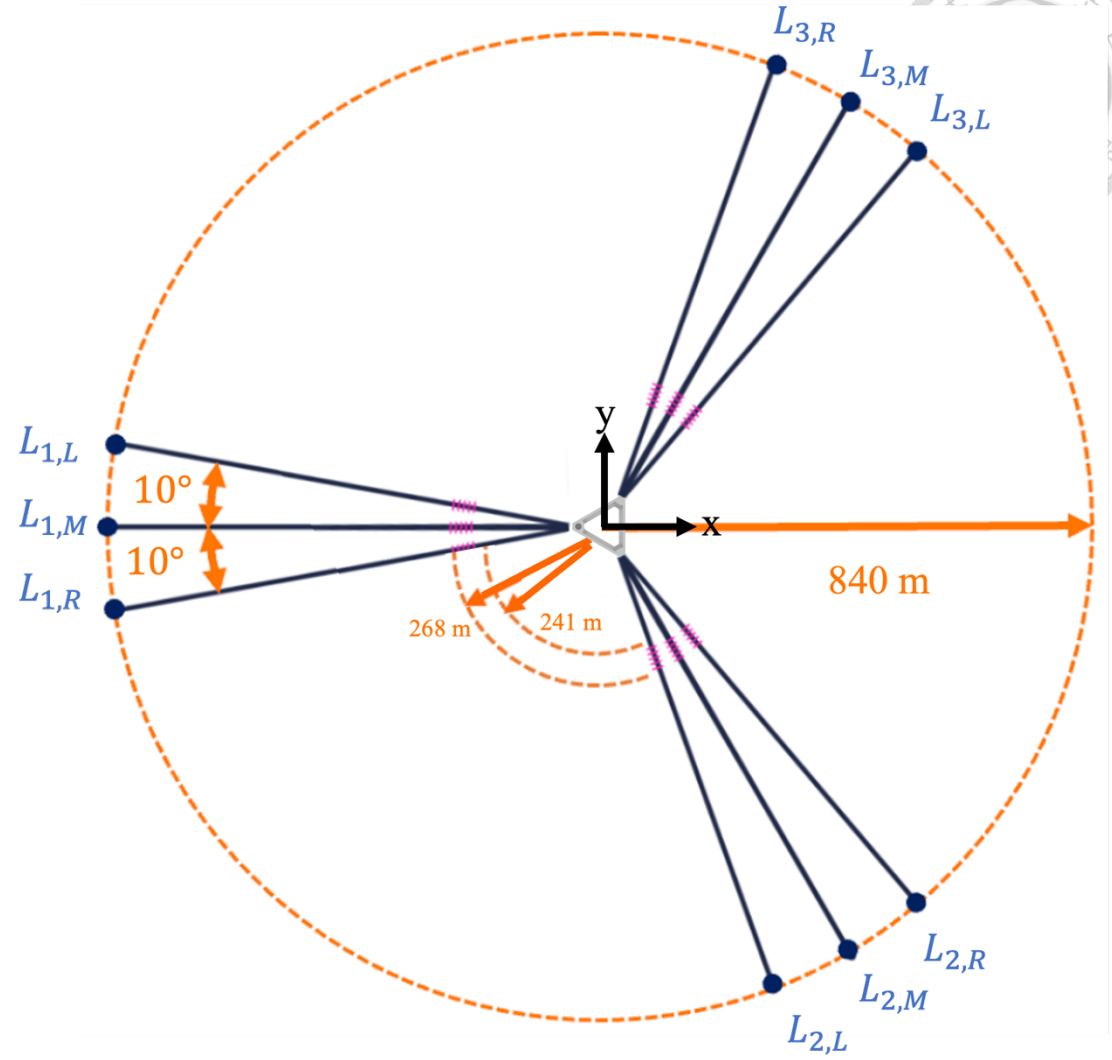

(a)

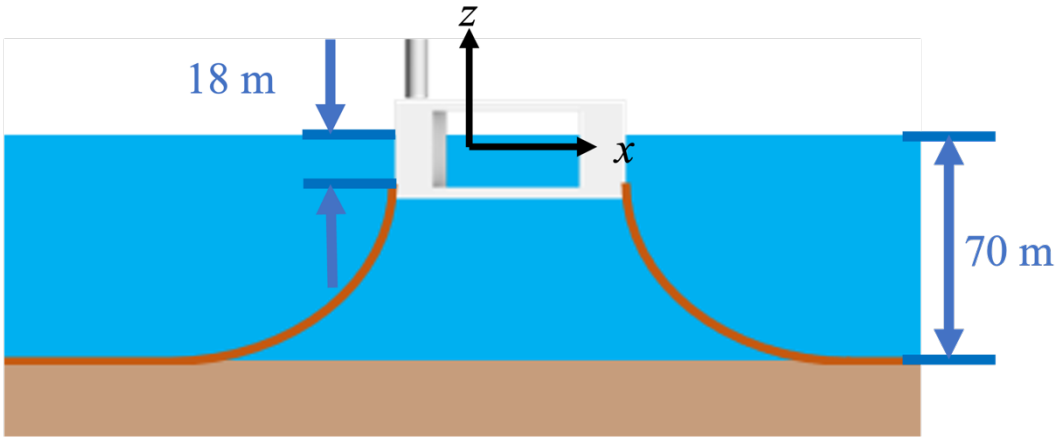

(b)

Figure 6 Mooring design of the wind turbine system, showing (a) the top view and (b) the side view

doi:10.6342/NTU202403052

2.3 Wind Turbine Design

This research focuses on the IEA 15 MW offshore wind turbine [26]. The dimensions and specifications of the wind turbine are detailed in Table 3 with a visual representation of its design provided in Fig. 7. The rotor blade's geometric design, using the DTU FFA-W3 airfoil series, is illustrated in Fig. 8, while the blade's shape is depicted in Fig. 9. Figure 10 demonstrates the aerodynamic properties of the airfoil. The blade geometry details are listed in Table 4. Figure 11 shows the relationship between the wind speed at the hub height U_w and blade pitch angle β_b, generator power P_g, rotor speed Ω_r and rotor thrust T_r.

doi:10.6342/NTU202403052

Table 3 Specifications of the IEA 15-MW offshore wind turbine

Rated Power (MW)	15
Rotor Orientation	Upwind
Configuration	3 Blades
Blade Length (m)	120
Hub Height (m)	150
Hub / Rotor Diameter (m)	7.94 / 240
Tower Base Diameter (m)	10
Hub Overhang (m)	11.35
Cut-in / Rated / Cut-out Wind Speed (m/s)	3 / 10.59 / 25
Cut-in / Rated Rotor Speed (RPM)	5 / 7.56
Shaft Tilt / Pre-Cone Angle (°)	6 / 4
Rotor Nacelle Assembly Mass (t)	1016.6
Tower Mass (t)	860

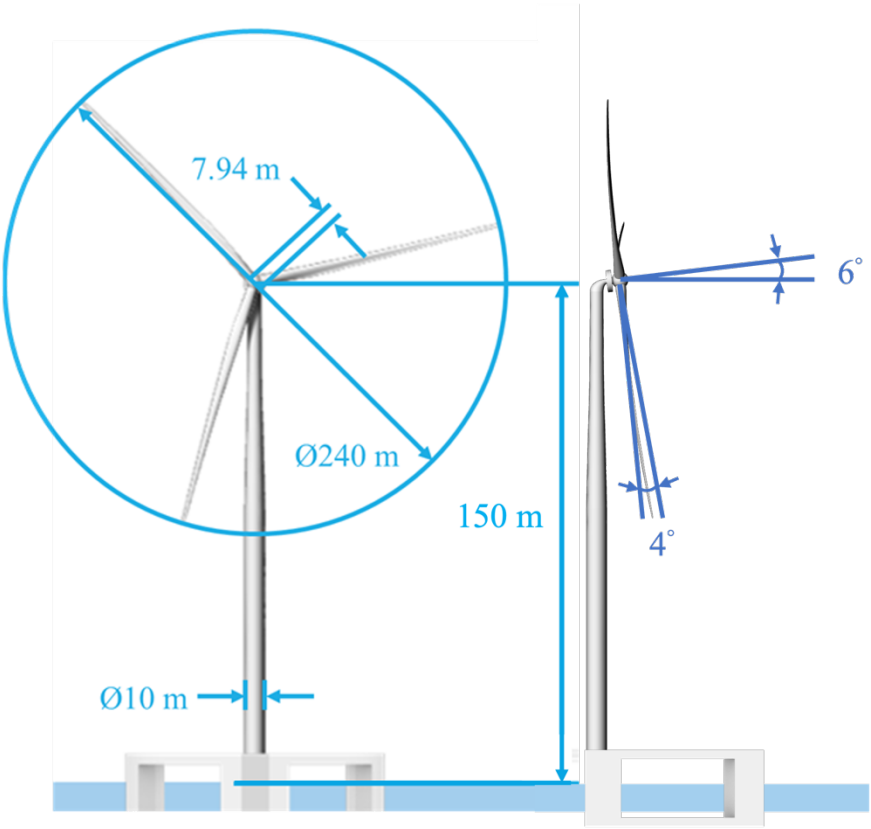

Figure 7 Dimensions of the IEA 15-MW offshore wind turbine

doi:10.6342/NTU202403052

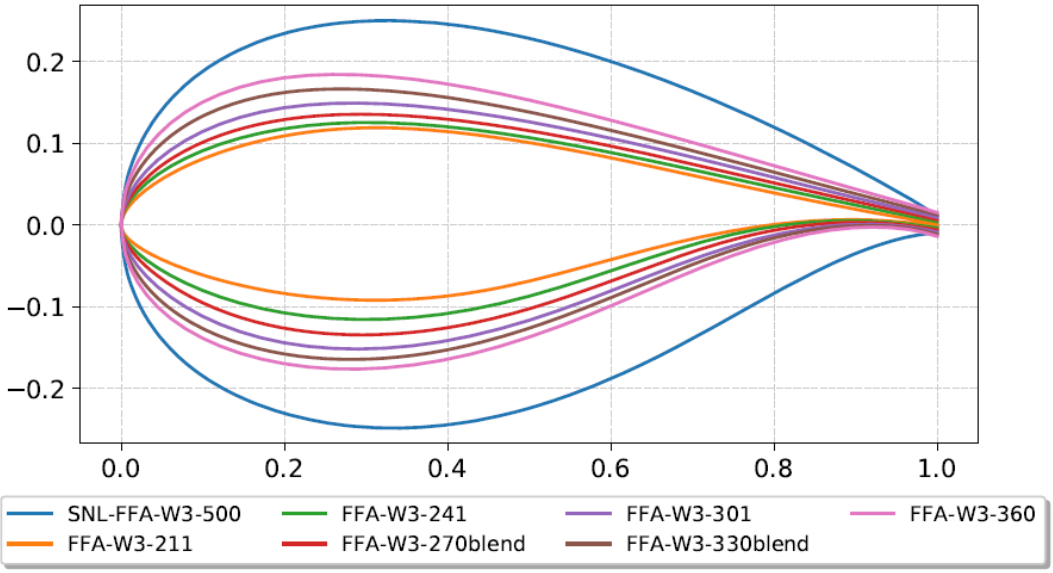

Figure 8 DTU FFA-W3 airfoils utilized in the design of the IEA 15-MW wind turbine blades [26]

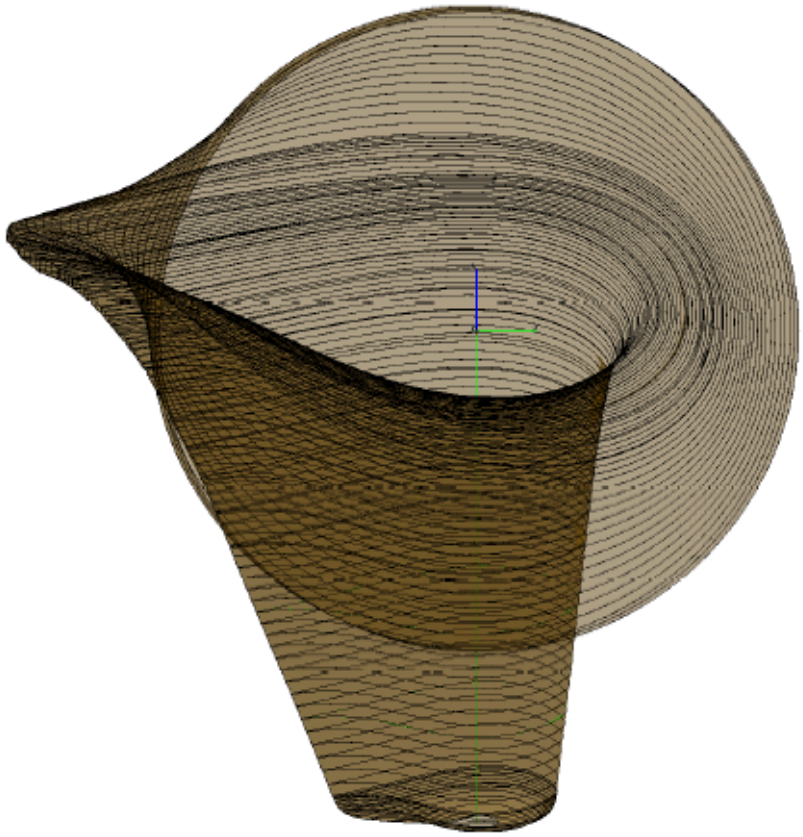

Figure 9 Lofted blade profile of the IEA 15-MW offshore wind turbine [26]

doi:10.6342/NTU202403052

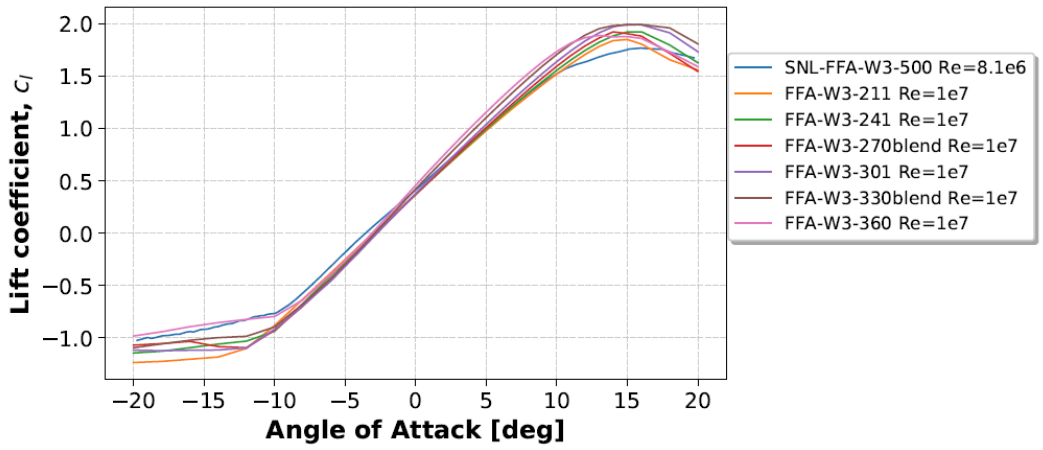

(a)

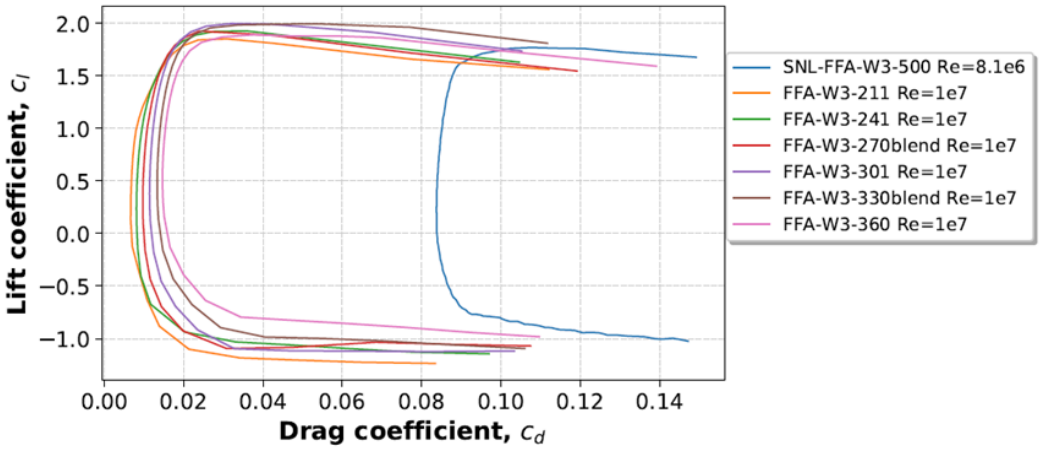

(b)

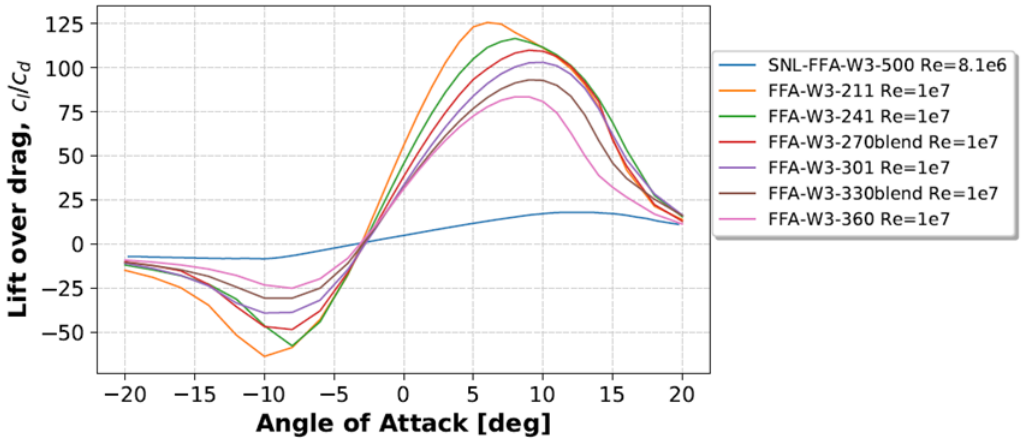

(c)

Figure 10 Aerodynamic characteristics of the DTU FFA-W3 airfoils [26], displaying (a) lift coefficients, (b) lift-drag polars, and (c) lift-to-drag ratios

doi:10.6342/NTU202403052

Table 4 Blade geometry of the IEA 15-MW offshore wind turbine [27]

Blade Fraction	Chord (m)	Twist (°)	Twist Axis Fraction	Airfoil Description
0.000	5.200	7.787	0.505	Circular
0.041	5.238	7.695	0.473	Transition
0.082	5.367	7.119	0.435	Transition
0.122	5.540	6.203	0.398	Transition
0.163	5.693	5.178	0.365	SNL-FFA-W3-500
0.204	5.765	4.270	0.340	SNL-FFA-W3-500
0.245	5.703	3.591	0.324	FFA-W3-360
0.286	5.472	2.963	0.315	FFA-W3-360
0.327	5.166	2.395	0.309	FFA-W3-330 Blend
0.367	4.886	1.921	0.304	FFA-W3-330 Blend
0.408	4.655	1.536	0.299	FFA-W3-330 Blend
0.449	4.428	1.204	0.294	FFA-W3-301
0.490	4.208	0.913	0.290	FFA-W3-301
0.531	3.999	0.650	0.288	FFA-W3-270 Blend
0.571	3.803	0.421	0.288	FFA-W3-270 Blend
0.612	3.617	0.218	0.290	FFA-W3-270 Blend
0.653	3.434	0.020	0.293	FFA-W3-241
0.694	3.249	-0.203	0.298	FFA-W3-241
0.735	3.065	-0.499	0.304	FFA-W3-241
0.776	2.881	-0.811	0.310	FFA-W3-211
0.816	2.691	-1.042	0.316	FFA-W3-211
0.857	2.489	-1.086	0.325	FFA-W3-211
0.898	2.276	-1.050	0.335	FFA-W3-211
0.939	2.053	-0.947	0.346	FFA-W3-211
0.980	1.820	-0.753	0.360	FFA-W3-211
0.990	1.708	-0.689	0.364	FFA-W3-211
1.000	0.500	-0.620	0.368	FFA-W3-211

doi:10.6342/NTU202403052

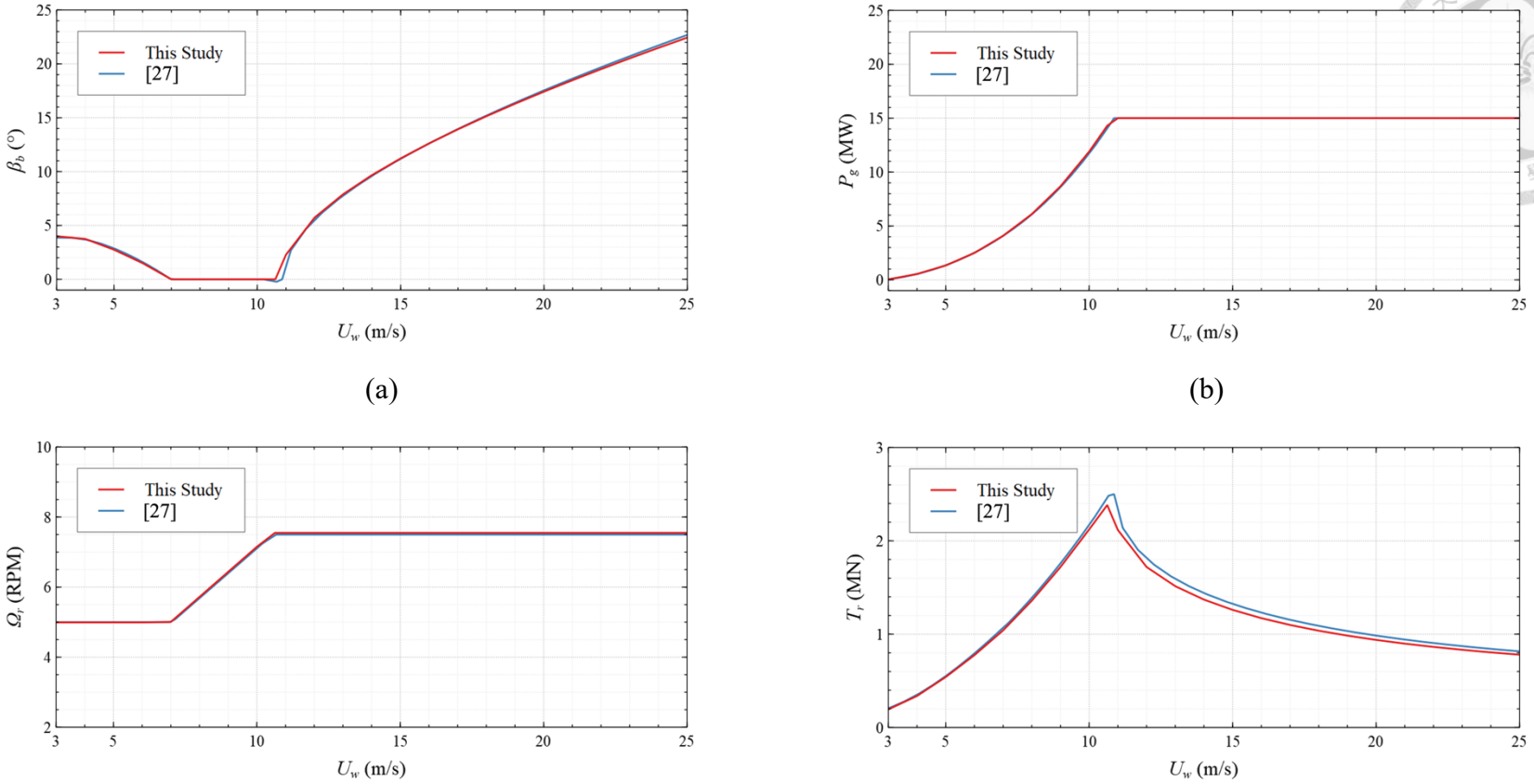

Figure 11 Comparison of wind turbine performance between this study and [26]: (a) Blade pitch angle, (b) Generator power, (c) Rotor speed,(d) Rotor thrust force

doi:10.6342/NTU202403052

3 Numerical Methods

3.1 Numerical Framework

To estimate the motion response and generator power of a FOWT system, the coupled equations of motion are solved using OrcaFlex. The equations of motion for a floating body are expressed as follows:

$$\sum_{j=1}^{6}\left(M + A_{ij}\right)\ddot{x}_j + B_{ij}\dot{x}_j + C_{ij}x_j = F_E + F_{o,i}, \tag{1}$$

where M denotes the body mass, A_{ij} denotes the added mass, B_{ij} denotes the damping, and C_{ij} denotes the stiffness of the floating body. The variables x_j, $\dot{x}_j$, and $\ddot{x}_j$ denote displacement, velocity, and acceleration, respectively. F_E denotes the wave exciting force, and $F_{o,i}$ denotes forces other than fluid force, such as aerodynamic loading and mooring tension. The subscripts $i, j = 1, 2, \ldots, 6$ correspond to surge, sway, heave, roll, pitch, and yaw motions, respectively. The values for A_{ij}, B_{ij}, C_{ij}, and $F_{o,i}$ are obtained from hydrodynamic property, aerodynamic loading, and mooring predictions. Given that the hydrodynamic properties (A_{ij} and B_{ij}) include potential and viscous components, modeling viscous flow in STAR-CCM+ is necessary to predict hydrodynamic properties considering viscous effects. The predicted viscous components are then used in Ansys Aqwa to calculate the load response amplitude operators, incorporating the effects of viscosity. The numerical framework for predicting the motion response and generator power of a FOWT system is illustrated in Fig. 12

Fluid forces can be divided into two categories: hydrostatic and hydrodynamic, as illustrated in Fig. 13. Hydrodynamic forces include the wave exciting force F_E and

doi:10.6342/NTU202403052

radiation force, which consist of the added inertia force $A_{ij}\ddot{x}_j$ and the radiation damping force $B_{ij}\dot{x}_j$. Hydrostatic forces are represented by the restoring force $C_{ij}x_j$. The wave exciting force comprises the Froude-Krylov force and the diffraction force, both of which are caused by incoming waves when the floating body is at rest. Conversely, radiation forces are generated by the motion of the floating body, ignoring the incoming waves. The Froude-Krylov force on the floating body is produced by the fluctuating pressure field of undisturbed waves, while the diffraction force is due to the disturbance of the incoming waves by the floating body.

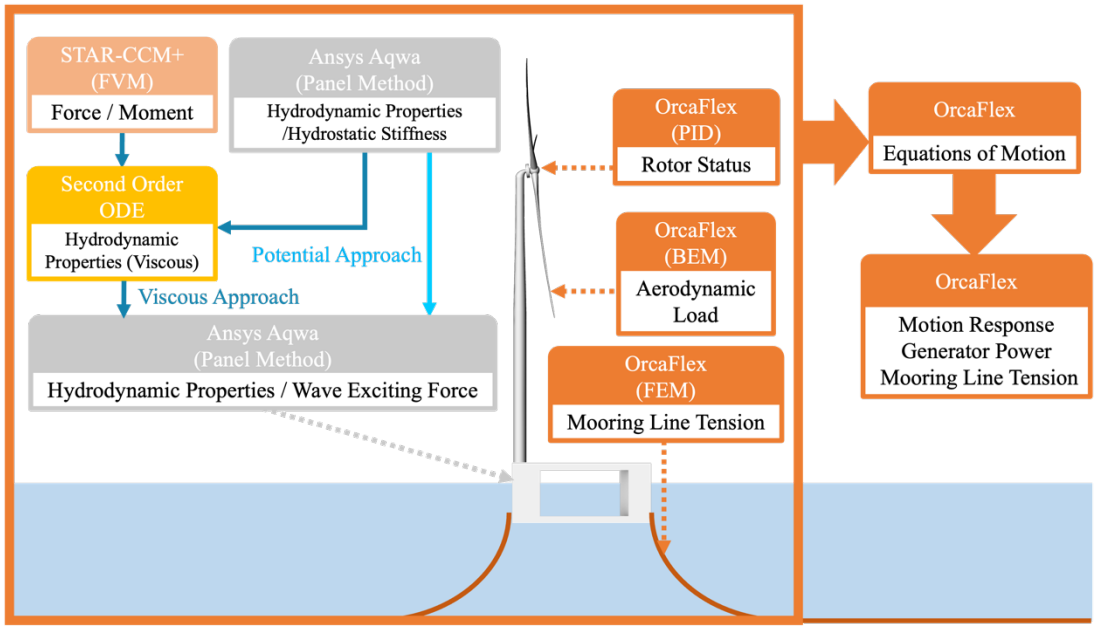

Figure 12 Numerical framework for predicting FOWT performance

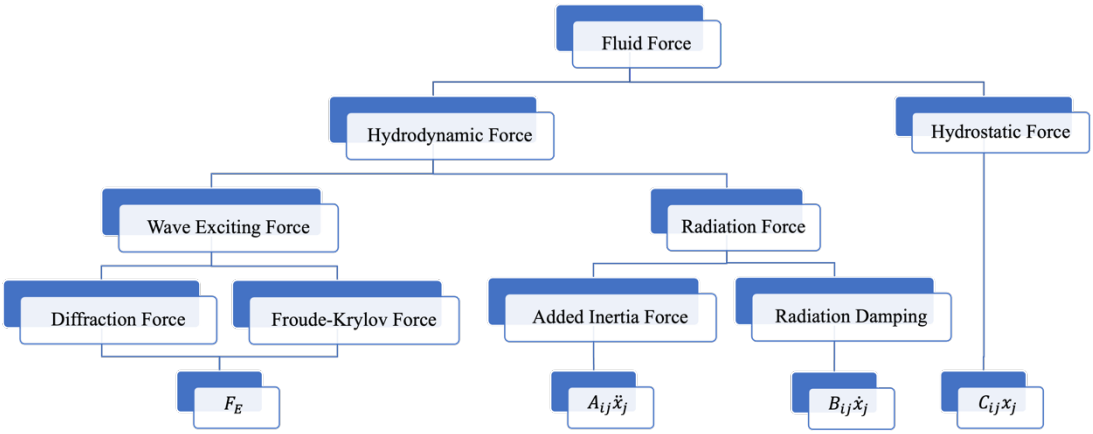

Figure 13 Components of the fluid force

doi:10.6342/NTU202403052

3.2 Potential Flow Modeling of Floating Body

Under the assumption of linear small-amplitude waves, Ansys Aqwa utilizes the panel method to predict the potential components of a floating body's hydrodynamic properties, employing three-dimensional potential flow theory. This theory treats the flow field as inviscid, irrotational, and incompressible. Figure 14 illustrates the coordinate system used for this potential flow formulation.

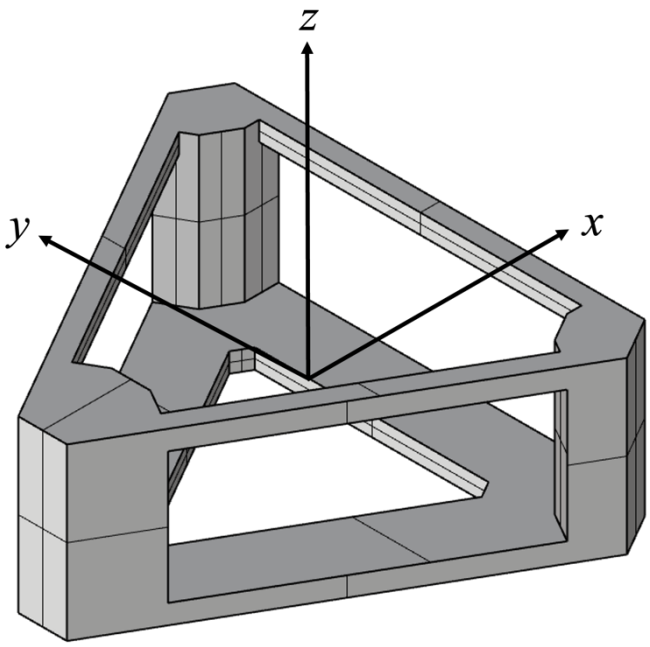

Figure 14 Coordinate system for potential flow formulation

The velocity potential $\Psi(x, y, z, t)$ within the flow field is defined as:

$$\Psi(x, y, z, t) = a_w \Phi(x, y, z) e^{-i\omega_w t}, \tag{2}$$

where a_w is the amplitude of the incident wave, $\Phi(x, y, z)$ is the spatially dependent term of the velocity potential with a unit wave amplitude, ω_w is the angular frequency of the wave, and t represents time. According to Haskind's theory [28] and [29], the potential due to incident, diffraction, and radiation waves can be expressed as follows:

doi:10.6342/NTU202403052

$$\Phi(x,y,z)e^{-i\omega_w t} = \left[\Phi_1(x,y,z) + \Phi_d(x,y,z) + \sum_{j=1}^{6} x_j \Phi_{r,j}(x,y,z)\right] e^{-i\omega_w t}, \quad (3)$$

where $\Phi_1(x,y,z)$ represents the first-order velocity potential of the incident wave with a unit wave amplitude. Similarly, $\Phi_d(x,y,z)$ refers to the diffraction wave potential, and $\Phi_{rj}(x,y,z)$ indicates the radiation wave potential caused by the floating body's unit motion amplitude. Here, x_j is the motion amplitude in the *j*-th direction, where $j = 1, 2, \ldots, 6$ corresponds to surge, sway, heave, roll, pitch, and yaw motions, respectively.

The first-order hydrodynamic force and moment components can be expressed in a generalized form as follows:

$$F_l = F_{E,l}^{[1]} + \sum_{l=1}^{6} x_j F_{r,lj}, \quad (4)$$

$$F_{E,l}^{[1]} = (F_{I,l} + F_{D,l}), \quad (5)$$

where $l = 1,2, \ldots,6$ represents the force acting in six motion directions. $F_{E,l}^{[1]}$ is the first-order wave exciting force in the l-th direction. $F_{I,l}$ denotes the Froude-Krylov force induced by the incident wave in the l-th direction and $F_{D,l}$ signifies the force generated by the diffracting wave in the l-th direction. $F_{R,lj}$ is the radiation force due to the motion-induced radiation wave with unit amplitude in the l-th direction, shown as below:

$$F_{I,l} = -i\omega_w \rho \int_{S_0} \Phi_1(x,y,z)\, n_l dS, \quad (6)$$

$$F_{d,l} = -i\omega_w \rho \int_{S_0} \Phi_d(x,y,z)\, n_l dS, \quad (7)$$

$$F_{r,lj} = -i\omega_w \rho \int_{S_0} \Phi_{r,j}(x,y,z)\, n_l dS, \quad (8)$$

doi:10.6342/NTU202403052

where ρ_w denotes the water density, S_0 represents the average wetted surface area, and n_l signifies the component of the unit normal vector.

Fluid forces are divided into two main types: active and reactive components. Active forces, which include wave exciting forces, primarily consist of Froude-Krylov forces. Reactive forces, on the other hand, arise from radiation waves produced by the body's movement, leading to radiation forces. The radiation wave potential, $\Phi_{r,j}$ can be expressed in terms of its real and imaginary components and then substituted into Eq. (8) to determine the added mass and wave-damping, as shown below:

$$\begin{aligned} F_{r,lj} &= -i\omega_a\rho_w \int_{S_0} \left\{ \{\mathrm{Re}[\Phi_{r,j}(x,y,z)] + i\mathrm{Im}[\Phi_{r,j}(x,y,z)] \right\} n_l dS \\ &= \omega_a\rho_w \int_{S_0} \mathrm{Im}\left[\Phi_{r,j}(x,y,z)\right] n_l dS \\ -i\omega_a\rho_w &\int_{S_0} \mathrm{Re}\left[\varphi_{r,j}(x,y,z)\right] n_l dS = \omega_w^2 A_{jl} + i\omega_w B_{jl}, \end{aligned} \tag{9}$$

where added mass A_{jl} and damping B_{jl} can be defined by Eq. (10) and Eq. (11), respectively, as shown below:

$$A_{jl} = \frac{\rho_w}{\omega_w} \int_{S_0} \mathrm{Im}\left[\Phi_{r,j}(x,y,z)\right] n_l dS, \tag{10}$$

$$B_{jl} = -\rho_w \int_{S_0} \mathrm{Re}\left[\Phi_{r,j}(x,y,z)\right] n_l dS. \tag{11}$$

Assuming ω_0 is the motion frequency and α_w is the angle between the incident wave and the *x*-axis, the wave potential Ψ_1 is expressed as

$$\begin{aligned} \Psi_1(x,y,z,t) &= \Phi_1(x,y,z)e^{i\omega t} \\ &= \frac{-iga_w}{\omega_0} \frac{\cosh k_0(z-h)}{\cosh k_0 h} e^{i(-\omega_w t + k_0(x\cos\alpha_w + y\sin\alpha_w)}, \end{aligned} \tag{12}$$

doi:10.6342/NTU202403052

$$k_0 = \frac{{\omega_0}^2}{g}, \tag{13}$$

where g is the acceleration due to gravity, and k_0 is the wave number. In this analysis, the floating body is assumed to have no forward velocity, making $\omega_w = \omega_0$.

Assuming the fluid is ideal and contains an isolated spatial dependency term in the velocity potential function, and by using linear hydrodynamics to account for wave radiation and diffraction. The interaction between the fluid and the structure requires that the velocity potential satisfies the Laplace equation:

$$\nabla^2 \Phi = \frac{\partial^2 \Phi}{\partial x} + \frac{\partial^2 \Phi}{\partial y} + \frac{\partial^2 \Phi}{\partial z}. \tag{14}$$

With the wave number denoted by $k_w = \frac{{\omega_a}^2}{g}$ and the radius of the flow field indicated as R_w, the boundary conditions for the far-field potentials Φ_d and $\Phi_{r,j}$ are as follows:

$$\lim_{R_w \to \infty} {R_w}^{\frac{1}{2}} \left(\frac{\partial}{\partial R_w} - i k_w \right) \Phi_d = 0, \tag{15}$$

$$\lim_{R_w \to \infty} {R_w}^{\frac{1}{2}} \left(\frac{\partial}{\partial R_w} - i k_w \right) \Phi_{r,j} = 0. \tag{16}$$

The boundary condition at the bottom of the flow field is given by

$$\frac{\partial \Phi}{\partial z} = 0 \text{ on } z \to -h, \tag{17}$$

where h denotes the water depth. The conditions at the free surface boundary are defined as follows:

$$-\omega_w^2 \Phi_1 + g \frac{\partial}{\partial z} \Phi_1 = 0 \text{ at } z = 0, \tag{18}$$

$$-\omega_w^2 \Phi_d + g \frac{\partial}{\partial z} \Phi_d = 0 \text{ at } z = 0, \tag{19}$$

$$-\omega_w^2 \Phi_{r,j} + g \frac{\partial \Phi_{r,j}}{\partial z} = 0 \text{ at } z = 0. \tag{20}$$

The boundary conditions on the surface of the floating body are defined as

doi:10.6342/NTU202403052

$$\frac{\partial \Phi_1}{\partial n} = -\frac{\partial \Phi_d}{\partial n}, \tag{21}$$

$$\frac{\partial}{\partial n}\Phi_{r,j} = -i\omega_w n_l, \tag{22}$$

where n is the normal vector. To solve these boundary condition equations, the source distribution method is employed. Letting $\boldsymbol{X}$ indicate the position of a platform and $\boldsymbol{\xi}$ indicate the position of a source, the Dirac delta function is defined as

$$\nabla^2 G(\boldsymbol{X}, \boldsymbol{\xi}, \omega) = \frac{\partial^2 \Phi}{\partial x^2} + \frac{\partial^2 \Phi}{\partial y^2} + \frac{\partial^2 \Phi}{\partial z^2} = \delta(\boldsymbol{X} - \boldsymbol{\xi}), \tag{23}$$

$$\boldsymbol{X} = (x, y, z), \tag{24}$$

$$\boldsymbol{\xi} = (\xi, \eta, \zeta), \tag{25}$$

$$\delta(\boldsymbol{X} - \boldsymbol{\xi}) = \begin{cases} 0 & \text{where } \boldsymbol{X} - \boldsymbol{\xi} \neq 0 \\ \infty & \text{where } \boldsymbol{X} - \boldsymbol{\xi} = 0 \end{cases}. \tag{26}$$

Wehausen and Laitone [30] described the three-dimensional Green's function $G(\boldsymbol{X}, \boldsymbol{\xi}, \omega)$ as follows:

$$\begin{aligned} & G(\boldsymbol{X}, \boldsymbol{\xi}, \omega) \\ & = \frac{1}{R_2} + \frac{1}{R_3} \\ & + \int_0^\infty \frac{2(k_0 + \nu)e^{-k_w h}\cosh[k_0(z+h)]\cosh[k_0(\zeta+h)]}{k_w \sinh(k_0 h) - \nu\cosh(k_0 h)} J_0(k_0 R_1) dk_w \\ & + i2\pi \frac{(k_0 + \nu)e^{-k_0 h}\cosh[k_0(z+h)]\cosh[k_0(\zeta+h)]}{\sinh(k_0 h) - k_0 d\cosh(k_0 h) - \nu d\sinh(k_0 h)} J_0(k_0 R_1), \end{aligned} \tag{27}$$

$$R_1 = [(x-\xi)^2 + (y-\eta)^2]^{0.5}, \tag{28}$$

$$R_2 = [R_1^2 + (z-\zeta)^2]^{0.5}, \tag{29}$$

$$R_3 = [R_1^2 + (z-\zeta+2h)^2]^{0.5}, \tag{30}$$

doi:10.6342/NTU202403052

where $J_o(x)$ is the Bessel function of the first kind, ν is the given by $\frac{{\omega_0}^2}{g}$. By applying Green's theorem, the velocity potential of diffraction and radiation waves can be expressed as a Fredholm integral equation of the second kind:

$$\Phi(\boldsymbol{X}) = \frac{1}{4\pi} \int_{S_0} \sigma(\boldsymbol{\xi}) G(\boldsymbol{X}, \boldsymbol{\xi}, \omega_w)\, dS. \tag{31}$$

Eqs. (21) and (22) show how the boundary condition on the surface determines the source strength over the mean wetted surface:

$$\frac{\partial \Phi}{\partial n} = -\frac{1}{2}\sigma(\boldsymbol{X}) + \frac{1}{4\pi} \int_{S_0} \sigma(\boldsymbol{\xi}) \frac{\partial G}{\partial n}\, dS. \tag{32}$$

To solve these equations, the Hess-Smith constant panel method is employed. This method divides the mean wetted surface into panels. It assumes that the potential and source strength are constant within each panel and represented by their average values over the surface area. Thus, the discrete integral forms of Eqs. (31) and (32) are expressed as follows:

$$\Phi(\boldsymbol{X}) = \frac{1}{4\pi} \sum_{l=1}^{N_p} \sigma_l G(\boldsymbol{X}, \boldsymbol{\xi_l}, \omega_w) \Delta S_l\, dS \tag{33}$$

$$\frac{\partial \Phi}{\partial n} = -\frac{1}{2}\sigma_i + \frac{1}{4\pi} \sum_{l=1}^{N_p} \sigma_l \frac{\partial G}{\partial n} \Delta S_l dS \tag{34}$$

where N_p denotes the number of panels covering the average wetted surface, ΔS_m denotes the area of the m-th panel, and $\boldsymbol{\xi_l}$ represents the coordinates of the geometric centers of the l-th panel.

Assuming $\boldsymbol{X}$ indicates the point on the surface at infinity, and $\boldsymbol{\xi}$ denotes the point on the body surface centered at the floating body's center of gravity (x_g, y_g, z_g), their horizontal coordinates can be defined as follows:

doi:10.6342/NTU202403052

$$x = r_1 \cos\theta + x_g, \tag{35}$$

$$y = r_1 \sin\theta + y_g, \tag{36}$$

$$\xi = r_2 \cos\theta_q + x_g, \tag{37}$$

$$\eta = r_2 \sin\theta_q + y_g. \tag{38}$$

The second-order wave drift force and moment can be expressed as follows:

$$\bar{F}_{E,1}^{(2)} = -\frac{\rho_w g a_w}{\nu}\mathrm{Re}[A_B^*(\chi)]\cos\chi - \frac{\rho g}{2\pi\nu}\cdot\frac{(1+e^{-2kh})^2}{1-e^{-4k_0h}+4hde^{-2k_0h}}\int_0^{2\pi}|A_B(\theta_1)|^2\cos\theta_1 d\theta_1 \tag{39}$$

$$\bar{F}_{E,2}^{(2)} = -\frac{\rho_w g a_w}{\nu}\mathrm{Re}[A_B^*(\chi)]\sin\chi - \frac{\rho g}{2\pi\nu}\cdot\frac{(1+e^{-2kh})^2}{1-e^{-4k_0h}+4hde^{-2k_0h}}\int_0^{2\pi}|A_B(\theta_1)|^2\sin\theta_1 d\theta_1 \tag{40}$$

$$\bar{M}_{E,6}^{(2)} = -\frac{2a\rho_w g k_0 a_w}{\nu[\tan(k_0h)+k_0h-\nu d\tanh(k_0h)\,]}\mathrm{Re}(A_C) - \frac{a\rho_w g k_0}{\pi\nu}\frac{1}{[\tan(k_0h)+kh-\nu d\tanh(k_0h)]^2}\mathrm{Re}[\int_0^{2\pi}A_C(\theta_1)A_B^*(\theta_1)\,d\theta_1] \tag{41}$$

where $\bar{F}_{E,1}^{(2)}$, $\bar{F}_{E,2}^{(2)}$, and $\bar{M}_{E,6}^{(2)}$ represent the second-order wave exciting force in the surge, sway and yaw directions, respectively. The superscript * denotes the complex conjugate of the value, and A_B and A_C are the coefficent of the equations.

doi:10.6342/NTU202403052

3.3 Viscous Flow Modeling of Floating Body

3.3.1 Governing Equations

To evaluate the hydrodynamic properties considering viscous effects, a forced motion simulation is conducted using STAR-CCM+ [31]. Figure 15 depicts the coordinate system used in the viscous flow formulation.

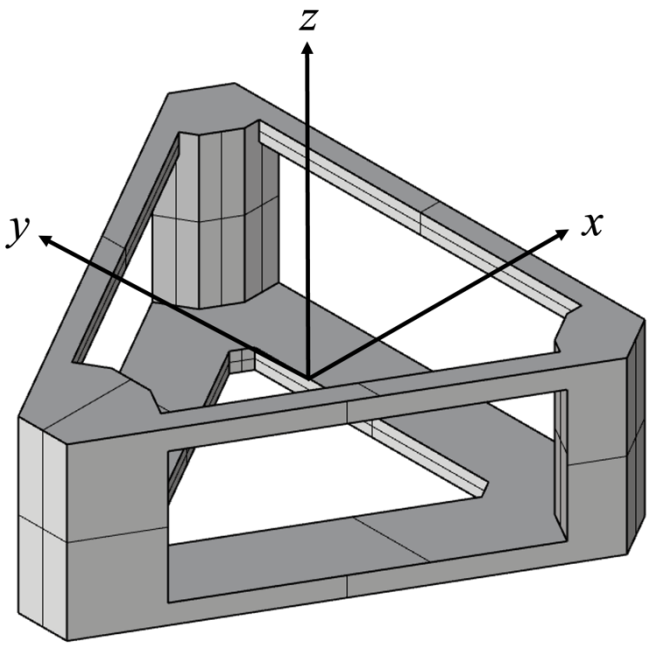

Figure 15 Coordinate system utilized in formulating viscous flow simulation

The time-averaged continuity equation for an incompressible fluid is given by

$$\frac{\partial(\rho\bar{u}_i)}{\partial x_i} = 0, \tag{42}$$

where ρ is the fluid density, and $\bar{u}_i$ denotes the mean velocity component in the x_i-direction. The momentum equations are expressed as:

$$\frac{\partial(\rho\bar{u}_i)}{\partial t} + \frac{\partial(\rho\bar{u}_i\bar{u}_j)}{\partial x_j} = -\frac{\partial\bar{p}}{\partial x_i} + \frac{\partial}{\partial x_j}\left[\mu\left(\frac{\partial\bar{u}_i}{\partial x_j} + \frac{\partial\bar{u}_j}{\partial x_i}\right)\right] - \frac{\partial\rho\overline{u_i'u_j'}}{\partial x_j} + \rho g_i, \tag{43}$$

doi:10.6342/NTU202403052

where $\bar{p}$ represents the mean pressure, μ is the fluid viscosity, $-\rho\overline{u_i'u_j'}$ in Eq (43) denotes the Reynolds stress, u_i' denotes the turbulent velocity component, and g_i denotes the gravity component in the i-direction, where $i = 1,2,3$ correspond to the x-, y- and z-directions, respectively.

doi:10.6342/NTU202403052

3.3.2 Turbulence Model

This study utilizes the SST *k*-*ω* model, which integrates features from both the standard *k*-*ω* and *k*-*ε* models. The equations governing turbulent kinetic energy (*k*) and specific dissipation rate (*ω*) are formulated as follows:

$$\frac{\partial(\rho k)}{\partial t}+\frac{\partial\left(\rho\bar{u}_j k\right)}{\partial x_j}=\tau_{ij}\frac{\partial\bar{u}_i}{\partial x_j}-\beta^*\rho\omega k+\frac{\partial}{\partial x_j}\left[(\mu+\sigma_k\mu_t)\frac{\partial k}{\partial x_j}\right], \tag{44}$$

$$\begin{aligned}\frac{\partial(\rho\omega)}{\partial t}+\frac{\partial\left(\rho\bar{u}_j\omega\right)}{\partial x_j}&=\frac{\rho\gamma}{\mu_t}\tau_{ij}\frac{\partial\bar{u}_i}{\partial x}-\beta\rho\omega^2+\frac{\partial}{\partial x_j}\left[(\mu+\sigma_\omega\mu_t)\frac{\partial\omega}{\partial x_j}\right]\\&+2(1-F_1)\frac{\rho\sigma_{\omega_2}}{\omega}\frac{\partial k}{\partial x_j}\frac{\partial\omega}{\partial x_j},\end{aligned} \tag{45}$$

where τ_{ij} denotes the shear stress. The blending function F_1 integrates coefficients from the *k*-*ω* model within the boundary layer with those from the *k*-*ε* model applied in the free shear layer and free flow region, defined as

$$F_1=\tanh\left\{\min\left[\max\left(\frac{\sqrt{k}}{\beta^*\omega d},\frac{500\nu}{d^2\omega}\right),\frac{2k}{d^2CD_{k\omega}}\right]^4\right\}, \tag{46}$$

where d is the shortest distance to the wall, β^* is set to 0.09, $\frac{\sqrt{k}}{\beta^*\omega d}$ denotes the turbulence length scale, ν denotes the kinematic viscosity, and $CD_{k\omega}$ is the cross-diffusion coefficient, as shown below. Other model constants are listed in Table 5. According to the Boussinesq eddy viscosity assumption [32], Reynold's stress is related to the mean strain rate tensor. The eddy viscosity μ_t is calculated using the SST *k*-*ω* model [31] and defined as follows:

$$CD_{k\omega}=\max\left(\frac{1}{\omega}\nabla k\cdot\nabla\omega,10^{-20}\right), \tag{47}$$

$$-\rho\overline{u_i'u_j'}=\mu_t\left(\frac{\partial u_j}{\partial x_i}+\frac{\partial u_i}{\partial x_j}\right)-\frac{2}{3}\rho k\delta_{ij}, \tag{48}$$

doi:10.6342/NTU202403052

$$\mu_t = \min\left\{\frac{\rho k}{\max\left(\frac{\omega}{\alpha^*}, \frac{|\mathbf{S}|F_2}{a_1}\right)}, \frac{\rho k C_T}{\sqrt{3}|\mathbf{S}|}\right\}, \tag{49}$$

where k represents the turbulent kinetic energy, ω is the specific dissipation rate, $\bar{\mathbf{u}}$ is the mean velocity, and $\mathbf{S}$ is the mean strain rate tensor, defined as

$$\mathbf{S} = \frac{1}{2}(\nabla\bar{\mathbf{u}} + \nabla\bar{\mathbf{u}}^{\mathrm{T}}). \tag{50}$$

Table 5 Constants employed in the SST k-ω model [31]

a_1	0.31	β^*	$F_1\beta_1^* + (1-F_1)\beta_2^*$
C_T	0.6	β_1^*	0.09
F_2	$\tanh({f_2}^2)$	β_2^*	0.09
f_2	$\max\left(\frac{2\sqrt{k}}{\beta^*\omega d}, \frac{500\nu}{d^2\omega}\right)$	κ	0.41
α^*	$F_1\alpha_1^* + (1-F_1)\alpha_2^*$	σ_k	$F_1\sigma_{k_1} + (1-F_1)\sigma_{k_2}$
α_1^*	1	σ_{k_1}	0.85
α_2^*	1	σ_{k_2}	1
β	$F_1\beta_1 + (1-F_1)\beta_2$	σ_ω	$F_1\sigma_{\omega_1} + (1-F_1)\sigma_{\omega_2}$
β_1	0.075	σ_{ω_1}	0.5
β_2	0.0828	σ_{ω_2}	0.856

doi:10.6342/NTU202403052

3.3.3 Volume of Fluid Method

This study investigates the flow field across the free surface where air and water coexist using the volume of fluid (VOF) method [33]. In this method, the volume fraction of the i-th fluid within a cell is defined as:

$$\alpha_i = \frac{V_i}{V}, \tag{51}$$

where V is the total volume of the cell, and V_i is the volume occupied by the i-th fluid within that cell. To ensure conservation, the sum of the volume fractions must satisfy the following equation:

$$\sum_{i=1}^{N} \alpha_i = 1, \tag{52}$$

where N represents the total number of fluids. When $\alpha_i = 1$, the cell is fully occupied by the i-th fluid. Conversely, $\alpha_i = 0$ means the i-th fluid is absent in the cell. If $0 < \alpha_i < 1$, it indicates a mixture where multiple fluids, including the i-th fluid, coexist within the cell, forming a free surface. As a result, the ρ and μ within the cell are computed as weighted averages of these properties for the present fluids, given by

$$\rho = \sum_{i=1}^{N} \rho_i \alpha_i, \tag{53}$$

$$\mu = \sum_{i=1}^{N} \mu_i \alpha_i, \tag{54}$$

where ρ_i and μ_i are the density and viscosity of the i-th fluid, respectively. The continuity equation is then derived as

$$\frac{\partial \alpha_i}{\partial t} + u_j \frac{\partial \alpha_i}{\partial z_j} + \nabla \cdot \left(\alpha_i \mathbf{u}_{d,i}\right) + \nabla \cdot \left[\alpha_i (1 - \alpha_i) \mathbf{u}_{c,i}\right] = 0, \tag{55}$$

doi:10.6342/NTU202403052

where $\mathbf{u}_{d,i}$ and $\mathbf{u}_{c,i}$ denote the diffusion velocity and the boundary sharpening velocity of the i-th fluid, respectively, defined as

$$\mathbf{u}_{c,i} = C_\alpha |\mathbf{u}| \frac{\nabla \alpha_i}{|\nabla \alpha_i|}, \tag{56}$$

where C_α denotes the sharpening factor.

doi:10.6342/NTU202403052

3.3.4 Boundary Conditions

This study simulates the forced motion of the FOWT by defining the velocity using following equation:

$$V_f = \zeta_0 \omega \sin(\omega t), \tag{57}$$

where V_f is the generalized velocity of movement, ω is the angular frequency, and ζ_0 denotes the generalized amplitude. In this study, the amplitude ζ_0 is set to 1 m for translational motions and 1° for rotational motions.

To ensure the numerical accuracy of the force motion, this study employs an overset mesh technique to simulate the dynamics of FOWT system. The overset mesh consists of a background mesh encompassing the entire computational domain and a component mesh confined within the overset domain. During the simulation, the component mesh undergoes controlled translational or rotational motions. In this research, the surface of the floating body and the base of the computational domain are considered as no-slip boundaries, whereas the top and sides are identified as pressure outlets.

In the offshore region near Hsinchu, the typical water depth is around 70 m, which establishes the upper and lower limits of the computational domain as 70 m above and below the water surface. Given that the characteristic length of TaidaFloat is roughly 80 m, the height of the overset boundary is also set to this characteristic length. The computational domain extends 18.75 times the characteristic length, while the overset domain covers 1.25 times the characteristic length. Figure 16 provides a visual representation of the domain dimensions and boundary conditions.

doi:10.6342/NTU202403052

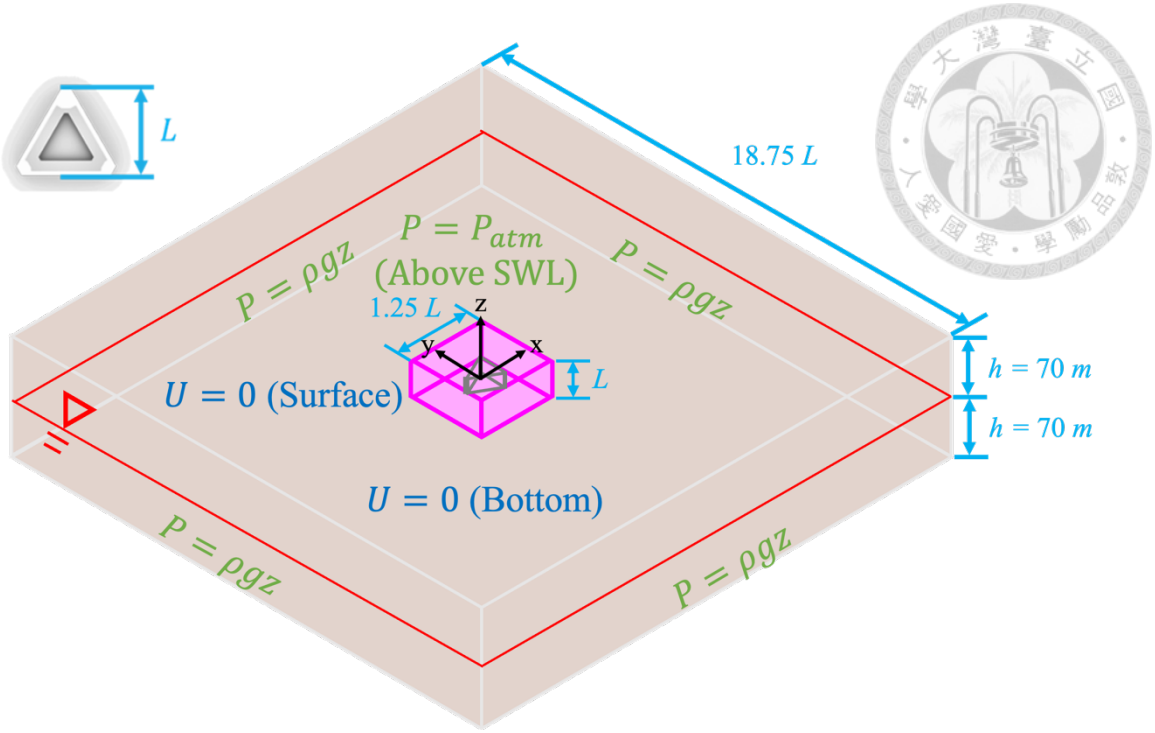

Figure 16 Computational domain for viscous flow modeling

To accurately assess the hydrodynamic forces and moments acting on the FOWT, the mesh was refined from the outside to the inside, with a finer mesh is employed near the free surface, recognizing its significant influence on hydrodynamic behavior. The mesh configuration used in STAR-CCM+ is shown in Fig. 17, highlighting the detailed mesh near the free surface to improve calculation precision.

doi:10.6342/NTU202403052

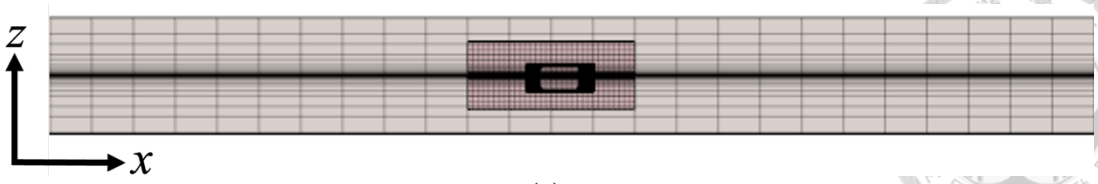

(a)

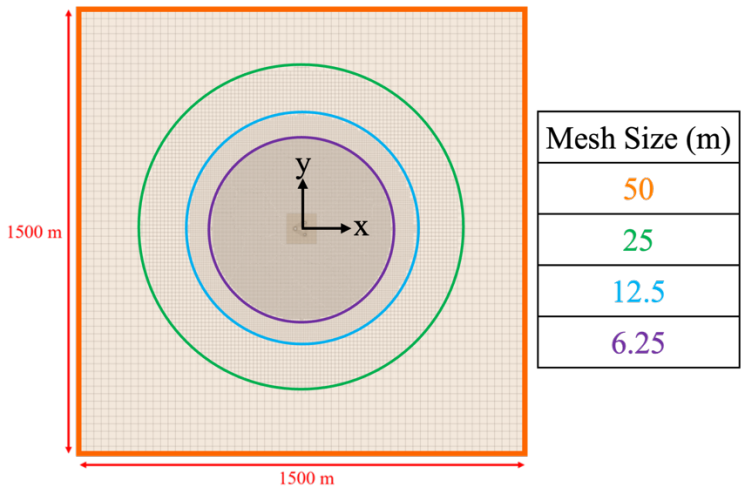

(b)

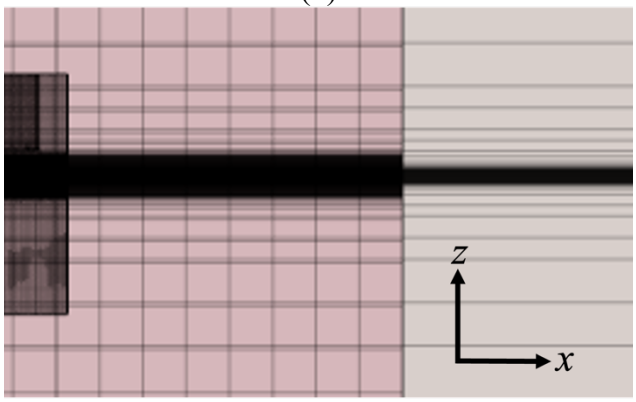

(c)

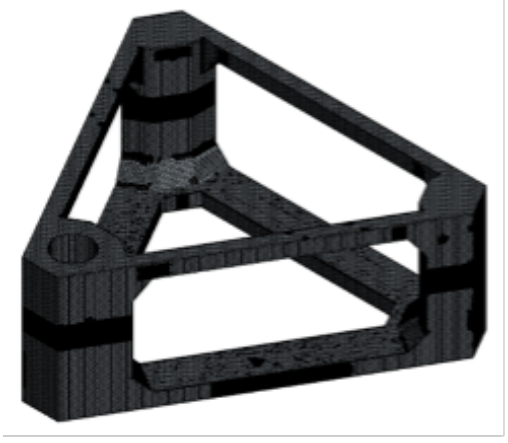

(d)

Figure 17 Mesh arrangement for viscous flow modeling: (a) side view, (b) top view, (c) refined mesh for the free surface, and (d) surface mesh of the platform

doi:10.6342/NTU202403052

3.4 Modeling of Wind Turbine

This research employs OrcaFlex to calculate the rotor aerodynamics using blade element momentum (BEM) theory, which integrates momentum theory with blade element theory.

3.4.1 Momentum Theory

Momentum theory is categorized into axial and angular momentum theories. Axial momentum theory assumes that the fluid is inviscid, incompressible, and irrotational. It uses the actuator disk model to represent the force distribution on the rotor plane. According to the principle of mass conservation, the inflow equals the outflow, as illustrated in Fig. 18. The following equations are derived from the Bernoulli equation:

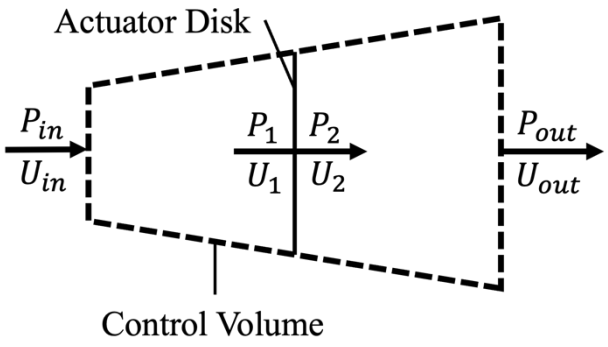

Figure 18 Axial momentum theory

$$P_{in} + \frac{1}{2}\rho {U_{in}}^2 = P_1 + \frac{1}{2}\rho {U_1}^2, \tag{58}$$

$$P_2 + \frac{1}{2}\rho {U_2}^2 = P_{out} + \frac{1}{2}\rho {U_{out}}^2, \tag{59}$$

where U_{in} and P_{in} refer to the fluid velocity and pressure before entering the control volume, as well as U_1 and P_1 denote the velocity and pressure just before reaching the actuator disk. The variables U_2 and P_2 represent the velocity and pressure immediately after the fluid passes through the actuator disk. U_{out} and P_{out} indicate the velocity and

doi:10.6342/NTU202403052

pressure as the fluid exits the control volume. The axial induction factor a is defined as the ratio of the velocity decrease as it enters the control volume to the initial velocity of the inflow:

$$a = \frac{U_{in} - U_1}{U_{in}}. \tag{60}$$

The pressure difference acting on the actuator disk multiplied by the disk area A gives the thrust T_r on the actuator disk, as shown below:

$$T_r = \frac{1}{2}\rho A {U_{in}}^2 4a(1-a). \tag{61}$$

Under the framework of axial momentum theory, angular momentum theory evaluates the torque exerted by the fluid on the actuator disk, taking into account the fluid's angular velocity induced by the rotor's rotation. As the rotor rotates with an angular velocity ω_a, there is a reduction in axial velocity before the rotor, given by $U_1 = U_{in}(1-a)$. Considering the change in fluid's angular velocity induced by the rotor, denoted as ω', and assuming r to be the cross-sectional radius, the torque Q is determined as follows:

$$Q = \frac{d(I\omega')}{dt} = \dot{m}r^2\omega', \tag{62}$$

where I represents the rotor's moment of inertia. The angular velocity induction factor, denoted as a', is calculated as

$$a' = \frac{\omega'}{2\omega_a}. \tag{63}$$

As depicted in Fig. 19, the moment dQ exerted by an annulus of width *dr* is expressed as:

$$dQ = 4a'(1-a)\frac{1}{2}\rho U_{in}\omega_a r^2 2\pi r dr. \tag{64}$$

doi:10.6342/NTU202403052

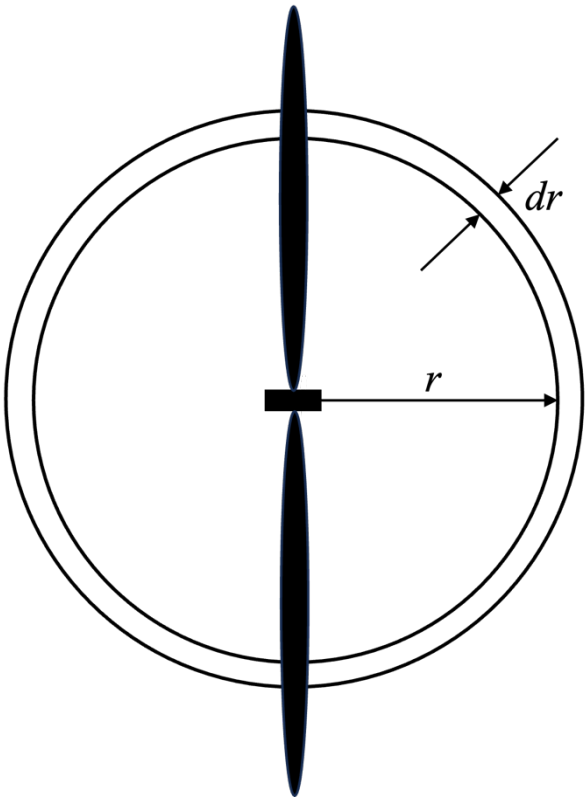

Figure 19 Angular momentum theory

doi:10.6342/NTU202403052

3.4.2 Blade Element Theory

Blade element theory involves dividing the blade into discrete segments along its length. The forces on each segment are computed based on the drag and lift coefficients of the local airfoil, assuming that each segment's aerodynamic behavior is independent. Assuming that r is the radial position, dr is the length, and c is the chord length of the blade section, respectively. The inflow velocity U_{in} for each blade section arises from the combination of wind speed, rotor speed, axial-induced velocity, and tangential-induced velocity, the axial induced velocity is $-U_{in}a$, and the vector sum of the tangential rotor speed and tangential induced velocity is

$$\omega_a r + \frac{\omega'}{2} r = \omega_a r + \omega_a r a' = \omega_a r(1 + a'). \tag{65}$$

There are various force components acting on the blade cross section, assuming α representing the angle of attack, and θ representing the relative inflow angle.

$$\tan(\theta) = \frac{U_{in}(1-a)}{r\omega_a(1+a')} = \frac{1-a}{1+a'}\lambda_r, \tag{66}$$

where λ_r is the local tip speed ratio defined as

$$\lambda_r = \frac{U_{in}}{r\omega_a}. \tag{67}$$

Next, the relative inflow velocity is given by

$$U = \frac{U_{in}(1-a)}{\sin\theta}. \tag{68}$$

For a rotor with n_b blades, the axial force F_a and the tangential force F_t can be calculated as

$$dF_a = n_b c \frac{1}{2}\rho U^2 [C_l \cos\theta + C_d \sin\theta] dr, \tag{69}$$

doi:10.6342/NTU202403052

$$dF_t = n_b c \frac{1}{2} \rho U^2 [C_l \sin\theta - C_d \cos\theta] dr, \tag{70}$$

where C_d and C_l denote the drag and lift coefficients, respectively. The moment dQ applied to the blade is determined by

$$dQ = n_b c \frac{1}{2} \rho U^2 [C_l \sin\theta - C_d \cos\theta] r dr. \tag{71}$$

doi:10.6342/NTU202403052

3.4.3 Blade Element Momentum Theory

The blade element momentum theory combines the momentum theory with blade element theory. This is achieved by equating dT_r from axial momentum theory with dF_a from blade element theory. By combining Eqs. (61) and (69), the following equation is derived:

$$\frac{a}{1-a} = \frac{\sigma[C_l \cos\theta + C_d \sin\theta]}{4\sin^2\theta}, \tag{72}$$

where σ is the local solidity, defined as

$$\sigma = \frac{n_b c}{2\pi}. \tag{73}$$

By equating dQ from angular momentum theory with dQ from blade element theory and combining Eqs. (64) and (71), the following equation is obtained,

$$\frac{a'}{1-a} = \frac{\sigma[C_L \sin\theta - C_D \cos\theta]}{4\lambda_r \sin^2\theta}. \tag{74}$$

Using Eqs. (72) and (74), a and a' can be expressed as

$$a = \frac{1}{1 + \frac{4\sin^2\theta}{\sigma[C_l \cos\theta + C_d \sin\theta]}}, \tag{75}$$

$$a' = \frac{1}{\frac{2\sin\theta\cos\theta}{\sigma[C_l \cos\theta + C_d \sin\theta]} - 1}. \tag{76}$$

The thrust force and mechanical power are then calculated, as

$$T_r = \int_{r_h}^{R_r} dT_r\,, \tag{77}$$

$$P = \int_{r_h}^{R_r} \omega_a dQ\,, \tag{78}$$

where r_h denotes the hub radius and R_r denotes the rotor radius.

doi:10.6342/NTU202403052

3.4.4 Tip Loss Model

Blade element momentum theory incorporates several simplifications, often leading to the predicted power values higher than the actual measured power. Momentum theory assumes the rotor has infinite blades, whereas, in reality, it typically has only three. This discrepancy causes energy losses due to vortices at the blade tips. To improve prediction accuracy in OrcaFlex, the lifting surface method [34] is applied, introducing a correction factor F, which varies between zero and one, i.e.,

$$F = \frac{2}{\pi}\cos^{-1}\left\{\exp\left[-\frac{\frac{n_b}{2}\left(1-\frac{r}{R}\right)}{\frac{r}{R}\sin\theta}\right]\right\}. \tag{79}$$

The axial induction factor a and the angular velocity induction factor a' are then corrected accordingly:

$$a = \frac{1}{1+\frac{4F\sin^2\theta}{\sigma[C_l\cos\theta + C_d\sin\theta]}}, \tag{80}$$

$$a' = \frac{1}{\frac{2F\sin\theta\cos\theta}{\sigma[C_l\cos\theta + C_d\sin\theta]} - 1}. \tag{81}$$

doi:10.6342/NTU202403052

3.5 Modeling of Control System

In OrcaFlex, the wind turbine control mechanism is coded in Python and utilizes two separate controllers: a generator torque controller for wind speeds under the rated threshold, and a full-span rotor-collective blade pitch controller for wind speeds above the rated threshold. Figure 20 illustrates the schematic of this control system.

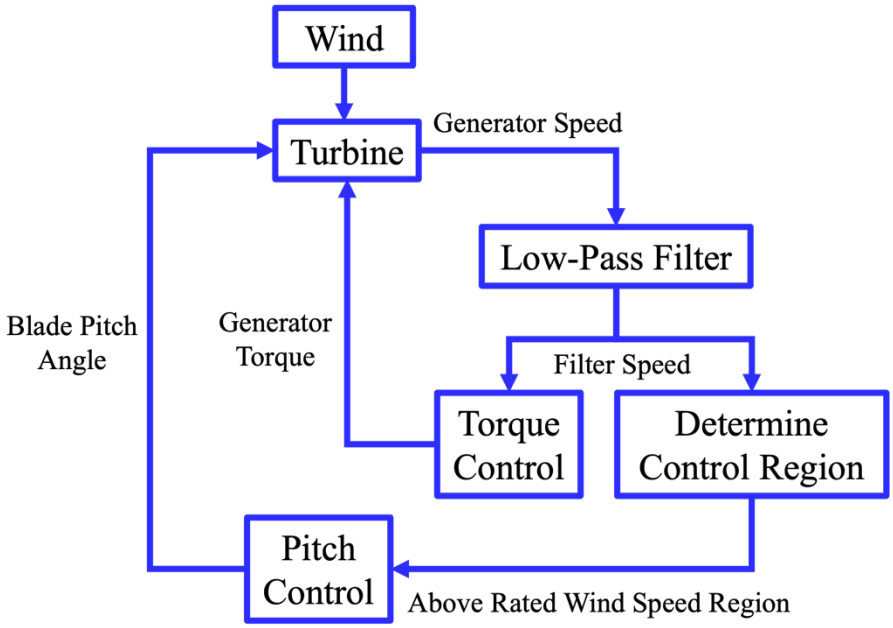

Figure 20 Schematic of the employed control system

A recursive single-pole low-pass filter with exponential smoothing is utilized within the model to reduce the impact of high-frequency excitation. The discrete-time recursive equation for this filter is formulated as follows:

$$y_{f,n} = (1 - \alpha_f)u_{f,n} + \alpha_f y_{f,n-1}, \tag{82}$$

$$\alpha_f = e^{-2\pi T_s \omega_s}, \tag{83}$$

where the filtered generator speed $y_{f,n}$ is derived from the unfiltered generator speed $u_{f,n}$ using a recursive single-pole low-pass filter with the coefficient α_f. Here, n

doi:10.6342/NTU202403052

represents the discrete-time-step counter, T_s denotes the discrete time step, and ω_s denotes the corner frequency. This study ignores the initial start-up phase, concentrating on operational conditions. An optimal proportionality constant is then applied to estimate the torque on the rotor, which is assumed to vary proportionally with the square of the generator speed. In the sub-rated wind speed range, a single-degree-of-freedom model is utilized to control the generator speed. The equation of motion is as follows:

$$T_a - N_g T_g = I_d \Delta\dot{\Omega}, \tag{84}$$

where T_a is the aerodynamic torque on the low-speed shaft, T_g is the torque generated on the high-speed shaft, N_g represents the gear ratio of high-speed to low-speed, I_d is the inertia of the low-speed shaft drivetrain, and $\Delta\dot{\Omega}$ is the rotational acceleration of the low-speed shaft. The inertia I_d is defined as

$$I_d = I_r + {N_g}^2 I_g, \tag{85}$$

where I_r is the rotor inertia, and I_g is the generator inertia relative to the high-speed shaft. For wind speeds exceeding the rated range, the equation of motion in the single-degree-of-freedom model is modified as follows:

$$T_a - N_g T_g = \left(I_r + {N_g}^2 I_g\right) \frac{d}{dt} (\Omega_0 + \Delta\Omega), \tag{86}$$

where Ω_0 denotes the rated rotational speed of the low-speed shaft, and $\Delta\Omega$ represents a minor fluctuation in the low-speed shaft's rotational speed around its rated value. The generator power P_g is formulated as

$$P_g = T_g N_g \Omega, \tag{87}$$

where Ω indicates the rotational speed of the low-speed shaft. The values of T_g and T_a are established as follows:

doi:10.6342/NTU202403052

$$T_g\left(N_g\Omega\right) = \frac{P_0}{N_g\Omega}, \tag{88}$$

$$T_a(\beta_b) = \frac{P(\beta_b, \Omega_0)}{\Omega_0}, \tag{89}$$

where P_0 and β_b denote the rated mechanical power and the blade pitch angle, respectively. Utilizing Taylor series expansion, Eqs. (88) and (89) can be approximated as

$$T_g \approx \frac{P_0}{N_g\Omega_0} - \frac{P_0}{N_g\Omega_0^2}\Delta\Omega, \tag{90}$$

$$T_a \approx \frac{P_0}{\Omega_0} + \frac{1}{\Omega_0}\left(\frac{\partial P}{\partial \beta_b}\right)\Delta\beta_b. \tag{91}$$

Incorporating a proportional-integral-derivative (PID) control, $\Delta\beta_b$ represents the small deviation of the blade pitch angle, as shown in Eq. (92).

$$\Delta\beta_b = K_p N_g \Delta\Omega + K_i \int_0^t N_g \Delta\Omega dt + K_d N_g \Delta\dot{\Omega}, \tag{92}$$

where K_p, K_i, and K_d represent the proportional, integral, and derivative gains of the blade pitch controller. Assuming $\dot{\varphi} = \Delta\Omega$, the equation of motion can be written as

$$\begin{aligned}\left[I_d + \frac{1}{\Omega_0}\left(-\frac{\partial P}{\partial \beta_b} N_g K_d\right)\right]\ddot{\varphi} + \left[\frac{1}{\Omega_0}\left(-\frac{\partial P}{\partial \beta_b}\right) N_g K_p - \frac{P_0}{{\Omega_0}^2}\right]\dot{\varphi} \\ + \left[\frac{1}{\Omega_0}\left(-\frac{\partial P}{\partial \beta_b}\right) N_g K_i\right]\varphi = 0.\end{aligned} \tag{93}$$

According to [35], when K_d is set to zero, the values of K_p and K_i are determined as follows:

$$K_p = \frac{2I_d\Omega_0\zeta_\varphi\omega_n}{N_g\left(-\frac{\partial P}{\partial \beta_b}\right)}, \tag{94}$$

doi:10.6342/NTU202403052

$$K_i = \frac{I_d \Omega_0 {\omega_n}^2}{N_g \left(-\frac{\partial P}{\partial \beta_b}\right)}, \tag{95}$$

where ω_n represents the natural frequency and ζ_φ denotes the damping ratio, which are derived from the following equations:

$$\omega_n = \sqrt{\frac{K_\varphi}{m_\varphi}}, \tag{96}$$

$$\zeta_\varphi = \frac{C_\varphi}{2\sqrt{K_\varphi M_\varphi}} = \frac{C_\varphi}{2M_\varphi \omega_n}. \tag{97}$$

The response of the pitch is assumed to vary almost linearly with the angle of the blade pitch.

$$\frac{\partial P}{\partial \beta_b} = \frac{\partial P}{\partial \beta_b}(\beta_b = 0)\left(1 + \frac{\beta_b}{\beta_{b,2}}\right), \tag{98}$$

where $\beta_{b,2}$ is the blade pitch angle at which the pitch sensitivity has doubled from its value at the rated operating point, i.e.,

$$\frac{\partial P}{\partial \beta_b}\left(\beta_b = \beta_{b,2}\right) = 2\frac{\partial P}{\partial \beta_b}(\beta_b = 0). \tag{99}$$

Eqs. (94) and (95) are derived using Eqs. (98) and (99) as references, namely:

$$K_p = \frac{2I_d \Omega_0 \zeta_\varphi \omega_n}{N_g \left[\left(-\frac{\partial P}{\partial \beta_b}\right)(\beta_b = 0)\right]} GK, \tag{100}$$

$$K_i = \frac{I_d \Omega_0 {\omega_n}^2}{N_g \left[\left(-\frac{\partial P}{\partial \beta_b}\right)(\beta_b = 0)\right]} GK, \tag{101}$$

where GK denotes the dimensionless gain correction factor, characterized as

$$GK(\beta_b) = \frac{1}{1 + \frac{\beta_b}{\beta_{b,2}}}. \tag{102}$$

doi:10.6342/NTU202403052

3.6 Modeling of Mooring

In OrcaFlex, mooring lines are modeled using the finite element method, as illustrated in Fig. 21 [36]. The mooring line is divided into straight, massless segments, what each ends with a node. These segments primarily contributes to the axial and torsional properties of the mooring line, with axial force being the most significant factor in the system. Each segment is further divided into two sub-segments, allowing the mass, weight, and buoyancy to be concentrated at the adjacent nodes.

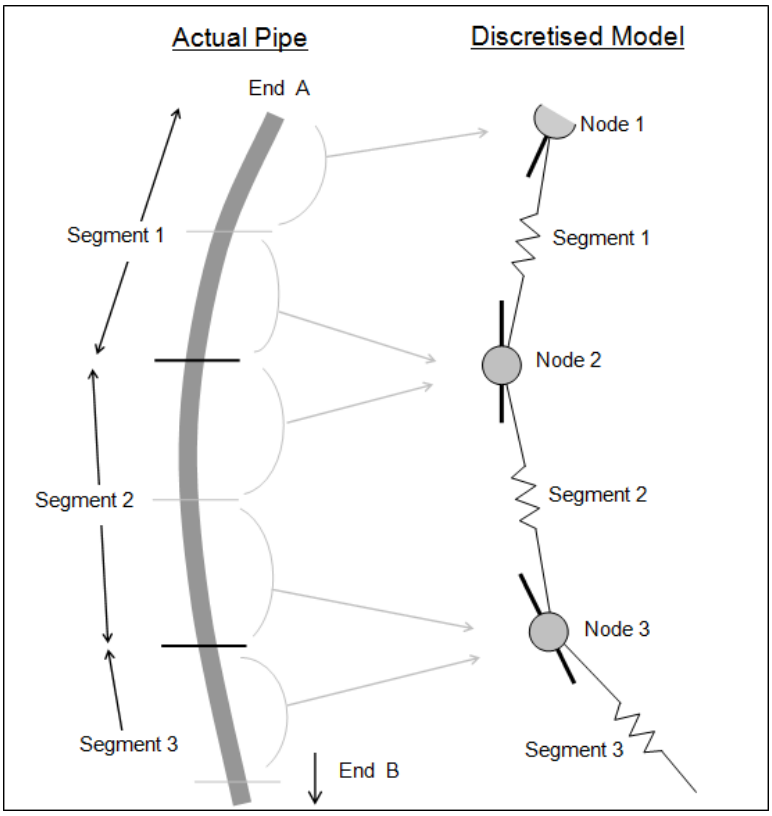

Figure 21 Finite element model for mooring lines [36]

The axial force includes both the effective tension T_e and the wall tension T_w, related by the equation:

$$T_e = T_w + (p_{ex}a_{ex} - p_{in}a_{in}), \tag{103}$$

doi:10.6342/NTU202403052

where p_{in} and p_{ex} are the internal and external pressures, and a_{in} and a_{ex} are the internal and external cross-sectional stress areas, respectively. The wall tension is calculated using the following equation:

$$T_w = EA\varepsilon - 2\nu_P(p_{ex}a_{ex} - p_{in}a_{in}) + k_{tt}\frac{\tau}{l_0} + EAc_d\frac{dl}{dt}\frac{1}{l_0}, \tag{104}$$

where EA is the axial stiffness, ε is the axial strain given by $\frac{l-\lambda_s l_0}{\lambda_s l_0}$, ν_P is the Poisson ratio, k_{tt} is the torque coupling coefficient, τ is the segment twist angle, l is the segment length, l_0 is the initial segment length, λ_s represents the expansion factor, and c_d is the damping coefficient expressed as

$$c_d = \frac{\lambda_a}{100}c_c, \tag{105}$$

$$c_c = \sqrt{\frac{2m_s l_0}{EA}}, \tag{106}$$

where λ_a signifies the desired tension damping, c_c denotes the critical damping coefficient for a segment, and m_s represents the mass of the segment.

doi:10.6342/NTU202403052

4 Hydrodynamic Properties

4.1 Time Shifting Approach (TSA)

This study employs Ansys Aqwa to predict the hydrodynamic properties without considering viscous effect. The hydrodynamic properties, considering viscous effects, are determined using STAR-CCM+ incorporated with the following approach.

Initially, with zero velocity in the flow field, no wave excitation force acts on the FOWT. Consequently, the fluid forces acting on the FOWT consist solely of radiation and hydrostatic forces. The results in STAR-CCM+ provide the total force $F_{o,1}$ as function of the generalized displacement $x_{i,1}$, as illustrated below:

$$F_{o,1} = A_i\ddot{x}_{i,1} + B_i\dot{x}_{i,1} + C_i x_{i,1}. \tag{107}$$

where A_i represents the added mass, B_i denotes the damping, and, C_i is the stiffness. According to Eq. (57), the displacement $x_{i,1}$, velocity $\dot{x}_{i,1}$, and acceleration $\ddot{x}_{i,1}$ are expressed as follows:

$$x_{i,1} = -\zeta_0 \cos(\omega t), \tag{108}$$

$$\dot{x}_{i,1} = \zeta_0 \omega \sin(\omega t), \tag{109}$$

$$\ddot{x}_{i,1} = \zeta_0 \omega^2 \cos(\omega t). \tag{110}$$

Next, the force curve is translated to the left by one-fourth of period, as shown in Fig. 22 (a), to obtain the force curve $F_{o,2}$, which is accordingly expressed:

$$F_{o,2} = A_i\ddot{x}_{i,2} + B_i\dot{x}_{i,2} + C_i x_{i,2}. \tag{111}$$

$$x_{i,2} = \zeta_0 \sin(\omega t), \tag{112}$$

$$\dot{x}_{i,2} = \zeta_0 \omega \cos(\omega t), \tag{113}$$

$$\ddot{x}_{i,2} = -\zeta_0 \omega^2 \sin(\omega t). \tag{114}$$

doi:10.6342/NTU202403052

Substituting Eqs. (108), (109), and (110) into Eq (107) and Eqs. (112), (113), and (114) into Eq (111), the following equations are obtained:

$$F_{o,1} = \zeta_0\big((\omega^2 A_i - C_i)\cos(\omega t) + \omega B_i \sin(\omega t)\big), \tag{115}$$

$$F_{o,2} = -\zeta_0\big((\omega^2 A_i - C_i)\sin(\omega t) + \omega B_i \cos(\omega t)\big). \tag{116}$$

The stiffness C_i of the floating body is determined using Ansys Aqwa. The variables A_i and B_i can be them calculated

$$A_i = \frac{F_{o,1}\cos(\omega t) - F_{o,2}\sin(\omega t) + C_k\zeta_0}{\zeta_0\omega^2}, \tag{117}$$

$$B_i = \frac{F_{o,1}\sin(\omega t) + F_{o,2}\cos(\omega t)}{\zeta_0\omega}. \tag{118}$$

In Fig. 22 (b) and (c), given the green line indicates the instantaneous value, while the orange line shows the average value.

doi:10.6342/NTU202403052

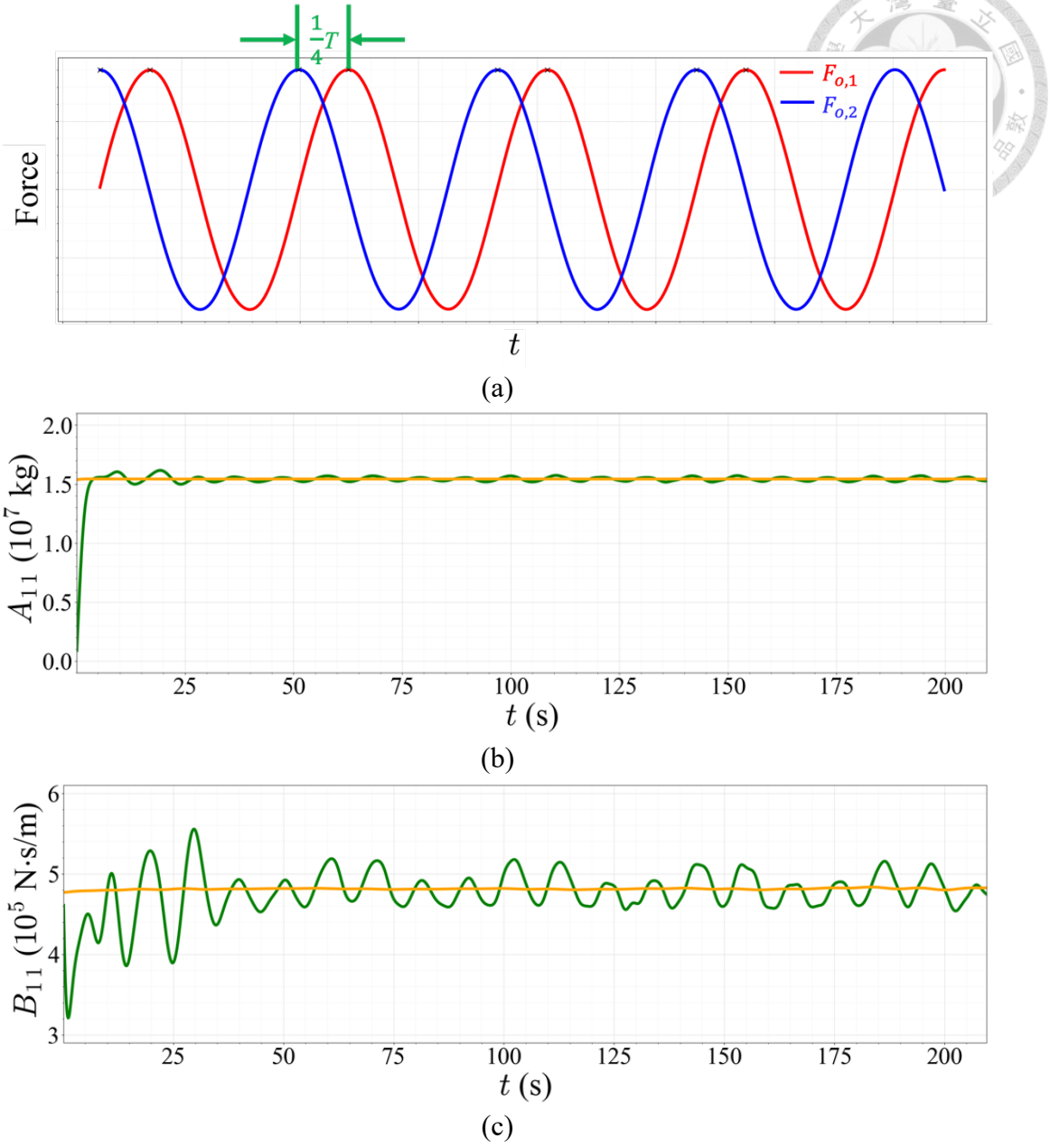

Figure 22 Time shifting approach: (a) translation of force curve, (b) predicted added mass, and (c) predicted damping

doi:10.6342/NTU202403052

4.2 Hydrodynamic Properties Considering Viscous Effect

After the calculation of hydrodynamic properties at a single frequency as described in Section 4.1, the next step is to obtain the curve of hydrodynamic properties considering viscous effect. Two methods for obtaining these curves are outlined below.

4.2.1 Single-Point Method

The forces and moments of the final five periods of a given forced motion are used to compute the average viscous hydrodynamic properties using the time shifting approach. At the force motion frequency, if the hydrodynamic property is lower than that obtained from the potential method, no adjustment is made, and the hydrodynamic property from the potential flow method is retained. However, if the hydrodynamic property is higher than that from the potential method, the hydrodynamic property curve from the potential method is offset by the difference between the viscous method and the potential method at the force motion frequency. Figure 23 illustrates the viscous damping obtained using the single-point method at a force surge motion frequency of 0.182 Hz.

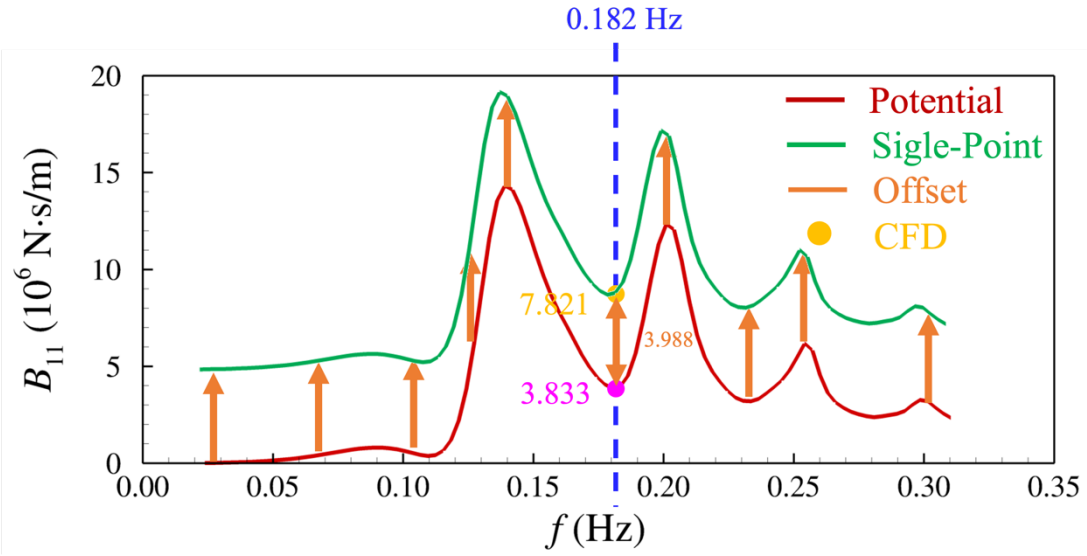

Figure 23 Schematic of the single-point method

doi:10.6342/NTU202403052

4.2.2 Fully Viscous Method

In this research, another method is used to obtain the hydrodynamic property curve. The force motion simulation is conducted at ten frequencies: 0.0238 Hz, 0.0557 Hz, 0.0875 Hz, 0.1193 Hz, 0.1512 Hz, 0.1830 Hz, 0.2148 Hz, 0.2467 Hz, 0.2785 Hz, and 0.3103 Hz. The hydrodynamic properties, considering the viscous effects, are estimated using the time shifting approach. Subsequently, the hydrodynamic properties obtained at these ten frequencies are fitted into a continuous curve. Figure 24 provides a schematic representation of the viscous damping curve obtained using the fully viscous method for surge motion.

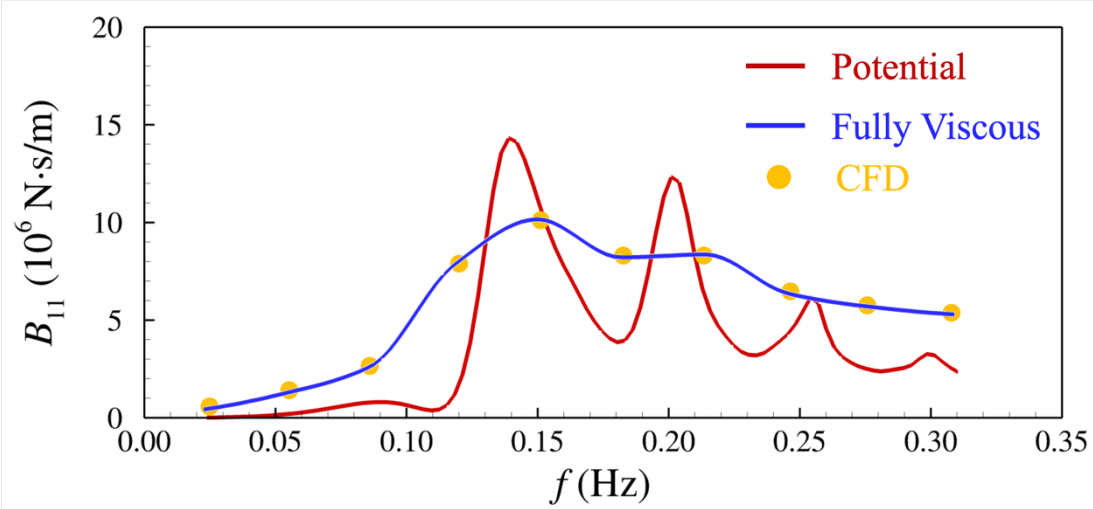

Figure 24 Schematic of the fully viscous method

doi:10.6342/NTU202403052

5 Validation

To ensure the accuracy of the numerical methods, The free decay heave and roll tests conducted on a 1/100 scale model [37], is chosen as the validation case. The dimensions of the model, shown in Fig. 25, were 79.2 cm in length, 92.9 cm in width, and 29.9 cm in height. The water tank used for the model testing measured 12 m in length, 8 m in width, and had a depth of 4 m. In the free decay motion depicted in Fig. 26, δ denotes the logarithmic decrement, T_D denotes damped period, ζ_D denotes damping ratio, and ω_n denotes natural frequency. These values are defined as follows:

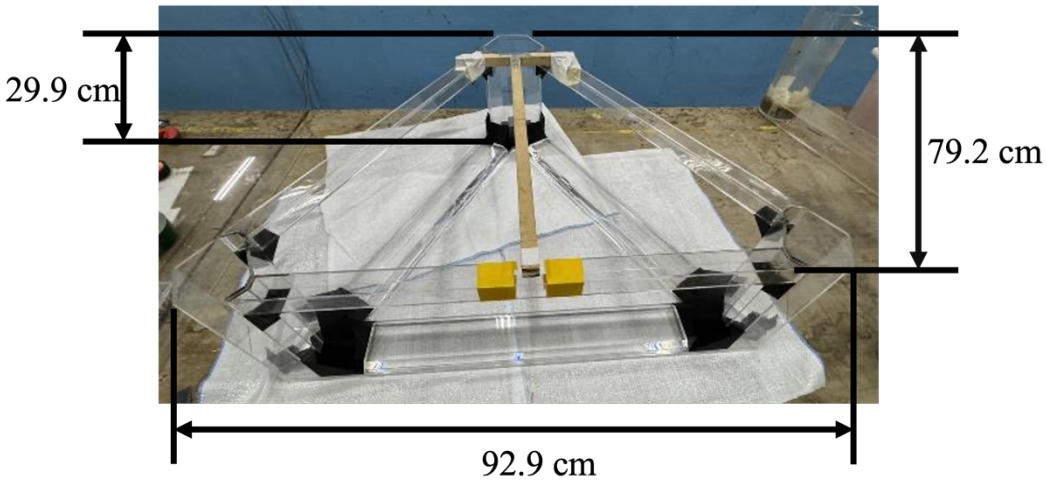

Figure 25 1/100 scale model of TaidaFloat Medium Demo

$$\delta = \frac{1}{N_p}\sum_{l=0}^{N_p} \ln\left(\frac{H_l}{H_{l+1}}\right), \tag{119}$$

$$T_D = \frac{1}{N_p}\sum_{l=1}^{N_p} t_l, \tag{120}$$

$$\zeta_D = \frac{\delta}{\sqrt{4\pi^2 + \delta^2}}, \tag{121}$$

$$\omega_n = \frac{2\pi}{T\sqrt{1-{\zeta_D}^2}}. \tag{122}$$

doi:10.6342/NTU202403052

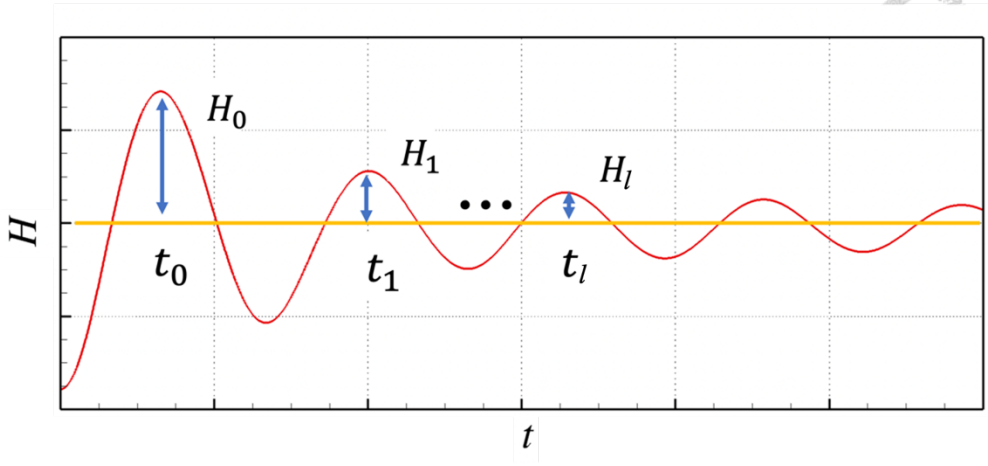

Figure 26 The free decay process

After determining the hydrodynamic properties of the model platform accounting for viscous effects using the fully viscous method, these properties were integrated into OrcaFlex. A comparison of the heave and roll motion time series was made between the potential flow theory, the fully viscous method, and the experiments by [37]. The initial conditions of heave and roll motions were 3.27 cm, and 5.68°, respectively. It is clear that neglecting viscosity leads to a very slow decay, whereas including viscosity produces results that are more aligned with the experimental data. Figure 27 displays the time series for the free decay in heave and roll motions.

When calculating the parameters for free decay, as presented in Table 6, the first period is often subject to high uncertainty; hence, calculations commence from the second period, i.e., $l = 2$. Observations indicate that considering the viscous effect results in free decay parameters are closer to the experimental values. This demonstrates that the numerical methods employed in this study are reasonably accurate.

doi:10.6342/NTU202403052

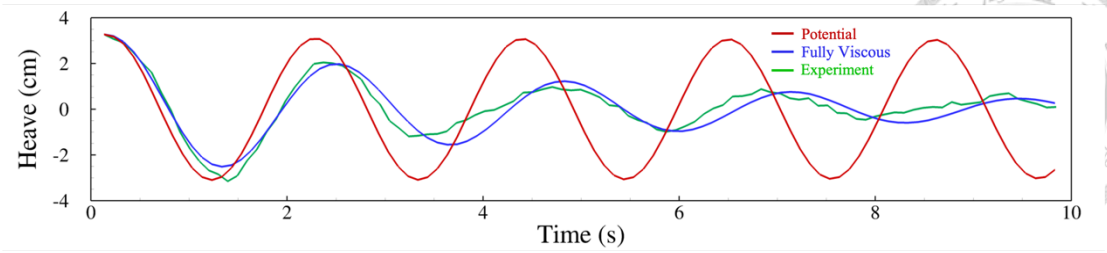

(a)

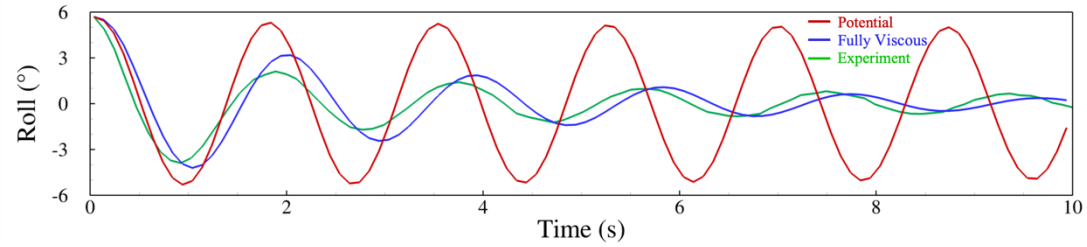

(b)

Figure 27 Free decay in time series: (a) heave, and (b) roll motion

Table 6 Free decay parameters: (a) heave, and (b) roll motion

(a)

Heave	l	δ	T_D	ζ_D	ω_n
Potential	2	0.004	2.100	0.065	2.992
Fully Viscous		0.478	2.300	7.591	2.748
Experiment		0.744	2.335	11.754	2.728
	2, 3	0.004	2.100	0.068	2.992
		0.744	2.335	11.754	2.728
		0.478	2.300	7.591	2.748

(b)

Roll	l	δ	T_D	ζ_D	ω_n
Potential	2	0.012	1.700	0.189	3.696
Fully Viscous		0.539	1.900	8.540	3.331
Experiment		0.405	1.866	6.435	3.382
	2, 3	0.017	1.700	0.269	3.696
		0.540	1.900	8.561	3.331
		0.393	1.857	6.242	3.397

doi:10.6342/NTU202403052

6 Metocean Data

6.1 Wave Conditions

This study examines two specific wave conditions: the CW condition, defined by (H_s, T_z) = (1.5 m, 5.5 s), and the EW condition, defined by (H_s, T_z) = (12.7 m, 8.83 s). Additionally, the study evaluates the long-term condition (LTC) using daily data from the Hsinchu buoy [38] provided by the Central Weather Administration (CWA), spanning from 2011 to 2020. The buoy is located 6 km offshore, in a water depth of 24 m. A statistical analysis of this data results in a wave scatter diagram for the Hsinchu offshore area, as shown in Table 7. This diagram is employed to assess the motion response and power performance of FOWT systems under various metocean conditions, ultimately determining the annual average power generation.

Table 7 Wave scatter diagram of the Hsinchu offshore area

H_s (m) \ T_z (s)	3.5	4.5	5.5	6.5	7.5	Sum (%)
0.25	3.70	3.59	0.06			7.35
0.50	8.04	13.19	1.28			22.51
0.75	3.87	12.13	1.42	0.06		17.47
1.00	1.53	10.13	1.95	0.03		13.63
1.25	0.08	7.43	3.62	0.08		11.21
1.50		4.48	4.45	0.19		9.13
1.75		0.83	8.90	0.31		10.04
2.50		0.03	7.18	0.92	0.03	8.15
3.50			0.03	0.42		0.45
4.50				0.06		0.06
Sum (%)	17.22	51.81	28.88	2.06	0.03	100

doi:10.6342/NTU202403052

According to [39], this research employs the JONSWAP spectrum with $\gamma = 2.08$. The spectral density $S(f)$ and its associated model constants are given as follows:

$$S(f) = \frac{\alpha g^2}{16\pi^4} f^{-5} e^{-\frac{5}{4}\left(\frac{f}{f_p}\right)^4} \gamma^b, \tag{123}$$

$$\alpha = 5.061(f_p)^4 H_s{}^2 (1 - 0.287\log\gamma), \tag{124}$$

$$b = e^{-\frac{1}{2\sigma^2}\left(\frac{f}{f_p} - 1\right)^2}, \tag{125}$$

$$\sigma = \begin{cases} 0.07, & f \le f_p \\ 0.09, & f > f_p \end{cases}, \tag{126}$$

where $S(f)$ represents the wave spectral density, f_p is the wave's angular peak frequency, γ denotes a parameter influenced by sea conditions, and H_s denotes the significant wave height. Reference [40] provides the relationship between the wave peak period T_p and the zero-crossing period T_z as follows:

$$T_p = T_z \sqrt{\frac{11 + \gamma}{5 + \gamma}}. \tag{127}$$

Figure 28 illustrates the changes in wave spectral density for CW and EW across different frequencies. It is evident that as the period increases, the energy of the wave spectrum shifts to lower frequencies, which is noteworthy. Furthermore, an increase in wave height result in higher energy level.

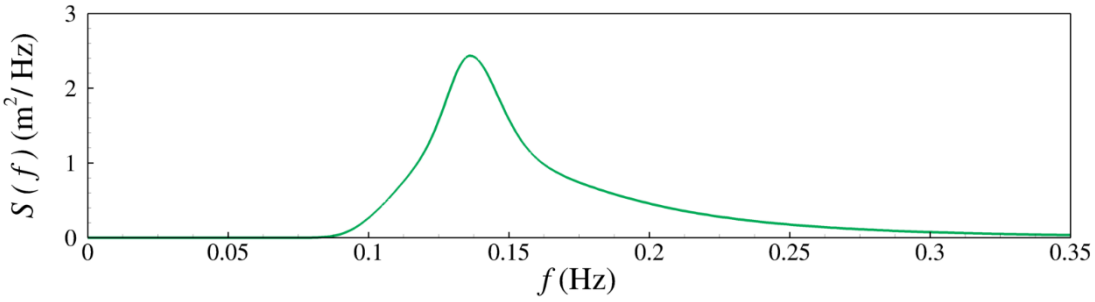

(a)

doi:10.6342/NTU202403052

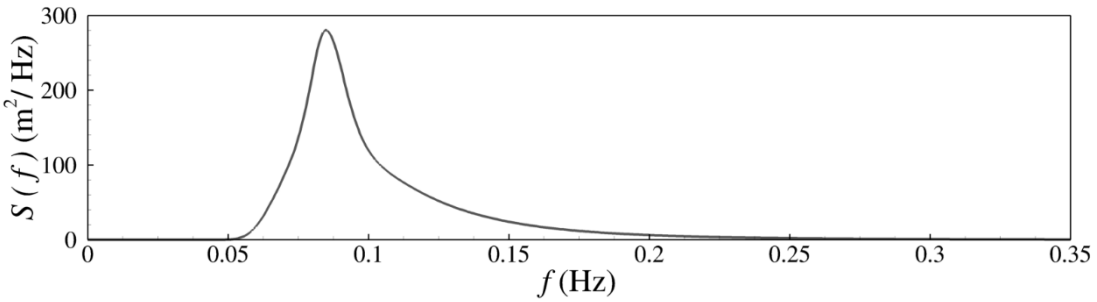

(b)

Figure 28 Dependence of $S(f)$ on f_p: (a) CW, and (b) EW conditions

doi:10.6342/NTU202403052

6.2 Wind Conditions

This research employs the American Petroleum Institute (API) spectrum [41] and constant wind speed to describe the wind speed behavior. Figure 29 contrasts the effects of constant wind speed with those of the API wind spectrum at $H_s = 4.5$ m. It shows that, unlike constant wind speed which remains stable, wind speed varies over time according to the API wind spectrum. The energy density in the API spectrum $S_A(f)$ is given by:

$$S_A(f,z) = U_z^2 I_z^2 f_p^{-1} \left[1 + 1.5\left(\frac{f}{f_p}\right)\right]^{-5/3}, \tag{128}$$

where S_A denotes the wind spectral density varying with frequency f and I_z is the turbulence intensity.The wind profile in the offshore area is characterized by

$$U_{10} = U_{hub}(\frac{10}{H_{hub}})^{\alpha}, \tag{129}$$

where U_{10} represents the wind speed at 10 m above MSL, U_{hub} is the wind speed at the hub height, H_{hub} denotes the hub height which is 150 m, and α is the surface roughness coefficient, valued at 0.1 due to the flat sea. Under the CW and EW conditions, the corresponding H_s values in Fig. 30, illustrating the relationship between wave height and wind speed according to the Beaufort wind scale [42], yield U_{10} values of 8.13 m/s and 40.64 m/s, respectively. U_{hub} of the CW and EW conditions are then calculated using Eq.(129). The wind velocities at the hub height are 11.4 m/s and 57 m/s, respectively, as depicted in Fig. 31. The metocean conditions for these two irregular wave scenarios are summarized in Table 8. The dependence of H_s on U_{10} and U_{hub} is given in Table 9. Wind directions recorded in the offshore area of Hsinchu were categorized into four main directions: θ_w = 45°, 135°, 225°, and 315°. The probabilities of wind occurrence for θ_w are presented in Table 10.

doi:10.6342/NTU202403052

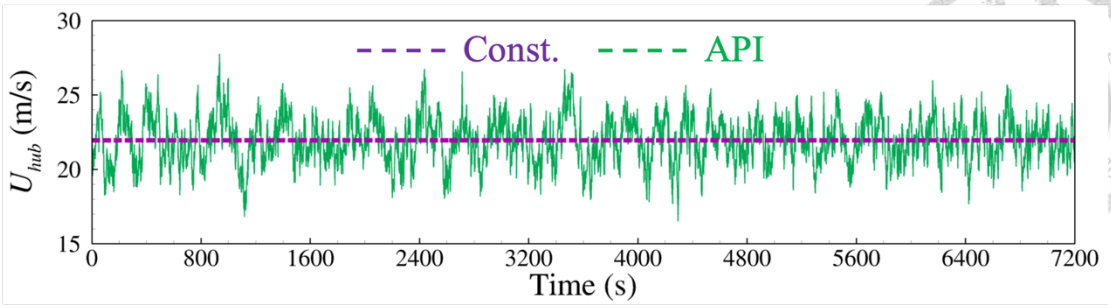

Figure 29 Comparison of constant wind speed with the API wind spectrum

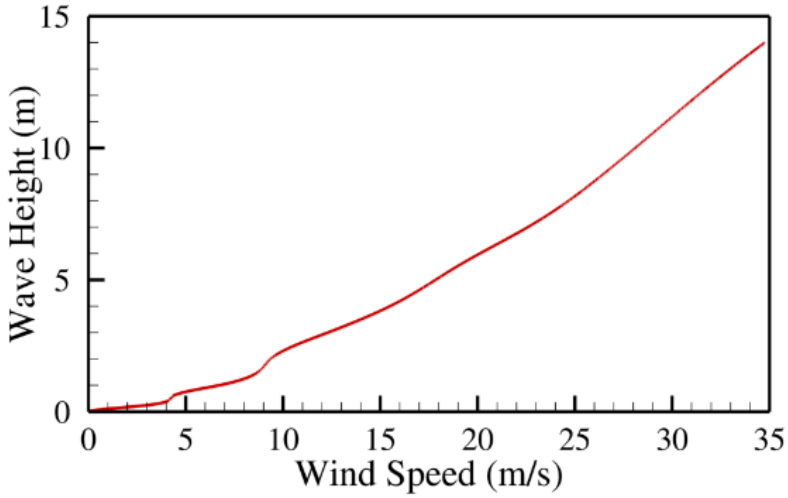

Figure 30 Beaufort wind scale – the relationship between wave height and wind speed

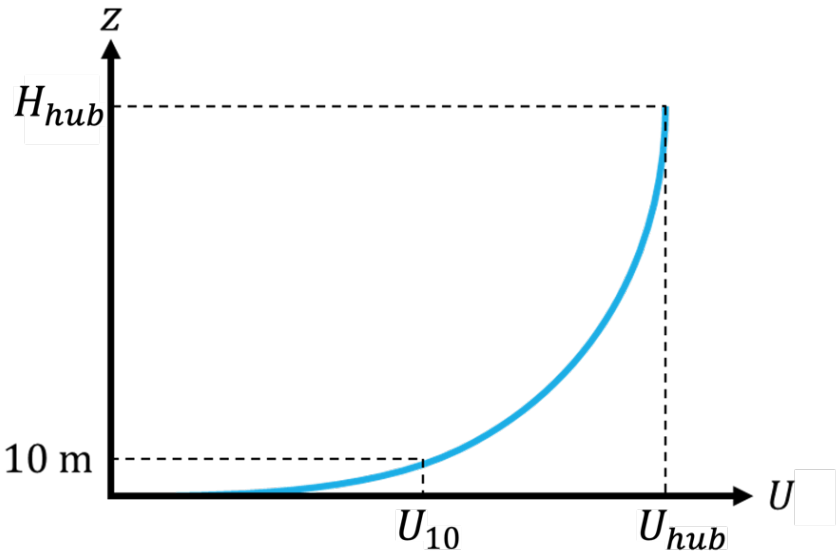

Figure 31 Schematic of the wind profile

doi:10.6342/NTU202403052

Table 8 Two irregular wave conditions

Irregular Wave Condition	CW	EW
H_s (m)	1.5	12.72
T_z (s)	5.5	8.83
U_{10} (m/s)	8.13	40.64
U_{hub} (m/s)	11.4	57

Table 9 Dependence of U_{10} and U_{hub} on H_s

H_s (m)	U_{10} (m/s)	U_{hub} (m/s)
0.25	2.82	3.96
0.50	3.94	5.53
0.75	4.64	6.51
1.00	6.23	8.87
1.25	7.47	10.48
1.50	8.13	11.40
1.75	8.45	11.86
2.50	9.87	13.84
3.50	13.07	18.34
4.50	15.64	21.94

Table 10 Probability distribution of θ_w in the Hsinchu offshore area

θ_w (°)	45	135	225	315
P_w (%)	13	22	13	52

doi:10.6342/NTU202403052

7 Case Descriptions

The motion definition and global coordinate system used in this study are depicted in Fig. 32. Assuming the wave direction aligns with the wind direction, this study investigates scenarios with a wind direction of 0° under two metocean conditions: CW and EW, where the wind turbine operates under CW condition and is parked under EW condition. The study employs three methods for predicting hydrodynamic properties, resulting in six cases. Table 11 presents the cases definitions of CW and EW scenarios. The study further examines long-term condition scenario using the wave scatter diagram for the Hsinchu offshore area, considering four wind (wave) directions along with API spectrum and constant wind speed, while the wind turbine is in operation. Two hydrodynamic properties prediction methods are utilized, amounting to 496 cases. These cases are employed to forecast the yearly mean energy and motion response, as demonstrated in Table 12. Figure 33 illustrates the direction of the wind (wave), with the north designated as 0°, and the angle is measured clockwise from the *x*-axis to the wind incoming direction.

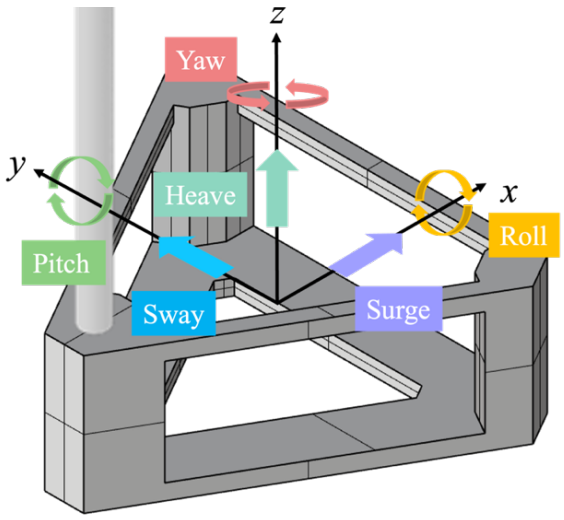

Figure 32 Global coordinate system of the FOWT system

doi:10.6342/NTU202403052

Table 11 Case definitions of CW and EW scenarios

Wave Condition	CW	EW
Turbine Status	Operating	Parked
Method	Potential, Single-Point, and Fully Viscous	
θ_w	0°	

Table 12 Case definitions of long-term condition

Wave Condition	31
Turbine Status	Operating
Method	Potential and Fully Viscous
θ_w	45°, 135°, 225° and 315°
Wind Spectrum	Constant wind speed and API

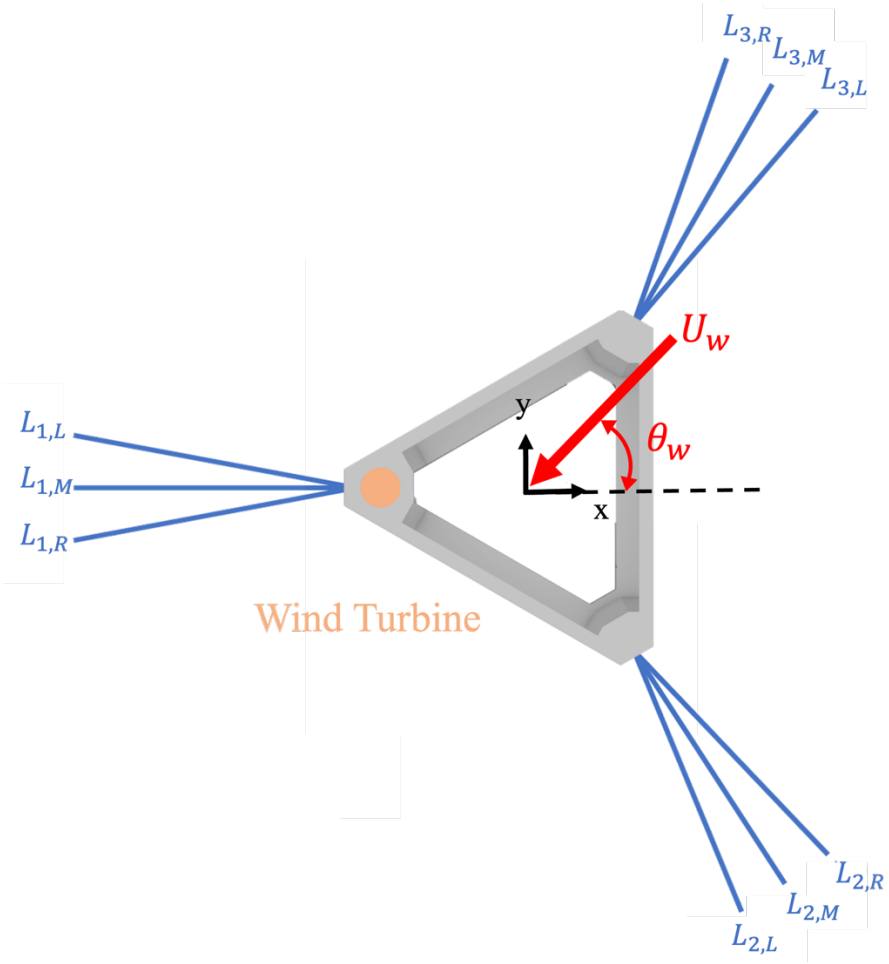

Figure 33 Definition of wind direction

doi:10.6342/NTU202403052

8 Simulation Results

8.1 Hydrodynamic Properties

In this study, Ansys Aqwa is first used to predict the hydrodynamic properties of the FOWT. Subsequently, STAR-CCM+ is utilized to the hydrodynamic properties considering viscous effect.

For the CW and EW conditions, the main frequencies are 0.182 Hz and 0.113 Hz, respectively. The stiffness coefficients for heave (C_{33}), roll (C_{44}), and pitch (C_{55}) motions, as calculated by Aqwa, are 6.41 MN/m, 52.03 MN/m, and 82.61 MN/m, respectively. Figure 34 and 37 display the added mass and damping, calculated using the potential and viscous methods. Table 13 and 14 provide the values of added mass and damping for the potential and fully viscous methods, respectively.

To quantify the potential component of added mass and damping, this study uses the ratio obtained by dividing the potential results by the fully viscous results. A higher ratio indicates a greater influence of inviscid effects on the added mass and damping.

By analyzing the added mass from the red line (potential) and the blue line (fully viscous) in Fig. 34 and Table 13, some observations are concluded: For surge motion, the highest ratio is 1.069 at 0.1193 Hz, and the lowest is 0.762 at 0.2148 Hz. At different frequencies, the ratio varies from 0.823 to 1.005. For sway motion, the highest ratio is 1.258 at 0.1830 Hz, and the lowest is 0.838 at 0.3103 Hz. Other frequencies show ratios between 0.85 and 1.072. These findings suggest the viscous effect is less significant in surge and sway motions. Regarding heave motion, the peak ratio is 0.923 at 0.2148 Hz, while the lowest is 0.764 at 0.3103 Hz. In heave motion, the added mass, considering the viscous effect, is higher than the inviscid effect across all frequencies. For roll motion,

doi:10.6342/NTU202403052

the maximum ratio reaches 1.079 at 0.1193 Hz, and the minimum is 0.682 at 0.0238 Hz. In pitch motion, the highest ratio is 0.993 at 0.1193 Hz, and the lowest is 0.694 at 0.0238 Hz. These findings indicate that the viscous effect is more prominent at low frequencies and tends to stabilize at higher frequencies in roll and pitch motions. For yaw motion, the highest ratio is 1.145 at 0.1193 Hz, and the lowest is 0.856 at 0.3103 Hz. At other frequencies, the ratios range from 0.869 to 1.079, indicating a less noticeable viscous effect in yaw motion.

Analyzing the damping values represented by the red line (potential) and the blue line (fully viscous) in Fig. 35 and Table 14, the followings are concluded. For surge motion, the peak ratio is 1.051 at 0.1512 Hz, and the lowest is 0.025 at 0.0238 Hz. At other frequencies, the ratios vary from 0.158 to 0.703. Similarly, in sway motion, the highest ratio is 0.998 at 0.1512 Hz, and the lowest is 0.025 at 0.0238 Hz, with ratios at other frequencies ranging from 0.162 to 0.819. These results indicate that at lower frequencies, the viscous effect is more significant, whereas at 0.1512 Hz, it becomes less pronounced in surge and sway motions. For heave motion, the maximum ratio is 0.248 at 0.0238 Hz, and the minimum is 0.001 at 0.2785 Hz and 0.3103 Hz, with other frequencies showing ratios between 0.002 and 0.223. In roll motion, the peak ratio is 0.591 at 0.1193 Hz, and the lowest is 0.001 at 0.2785 Hz and 0.3103 Hz, with ratios at other frequencies ranging from 0.003 to 0.119. For pitch motion, the maximum ratio is 0.521 at 0.0238 Hz, and the minimum is 0.001 at 0.2785 Hz and 0.3103 Hz, with other frequencies showing ratios between 0.005 and 0.391. These trends suggest that as frequency increases, the ratios decrease, approahing zero at 0.2467 Hz, 0.2785 Hz, and 0.3103 Hz, indicating a more significant viscous effect at higher frequencies in heave, roll, and pitch motions. In yaw motion, the highest ratio is 0.990 at 0.1512 Hz, and the lowest is 0.001 at 0.0238 Hz,

doi:10.6342/NTU202403052

with ratios at other frequencies ranging from 0.002 to 0.878. This suggests that the viscous effect is more pronounced at lower frequencies.

These findings demonstrate that that the viscous effect of damping is more obvious than the added mass, while the viscous effect significantly impacts added mass and damping in heave, roll, and pitch motions compared to surge, sway, and yaw motions. Specifically, the viscous effect on added mass is more pronounced at lower frequencies, while its influence on damping is greater at higher frequencies. This variation in the contribution of the viscous effect across different frequencies results in noticeable differences between the hydrodynamic property curves obtained using the fully viscous method and those derived from the singe-point method.

doi:10.6342/NTU202403052

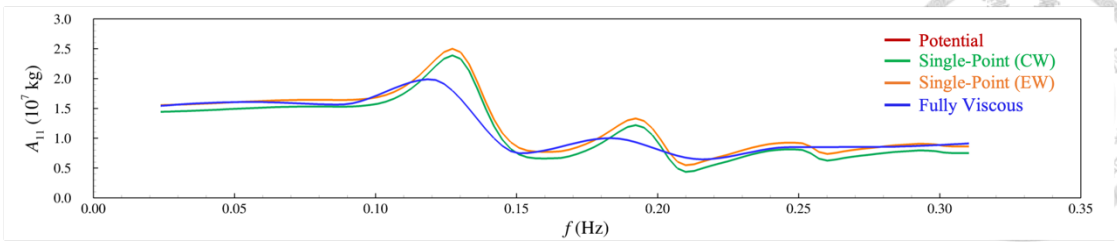

(a)

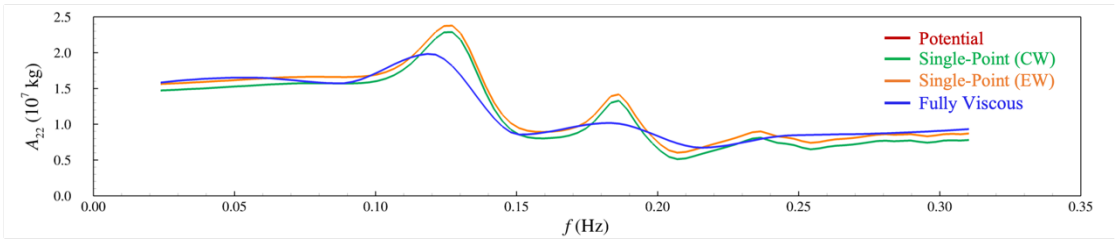

(b)

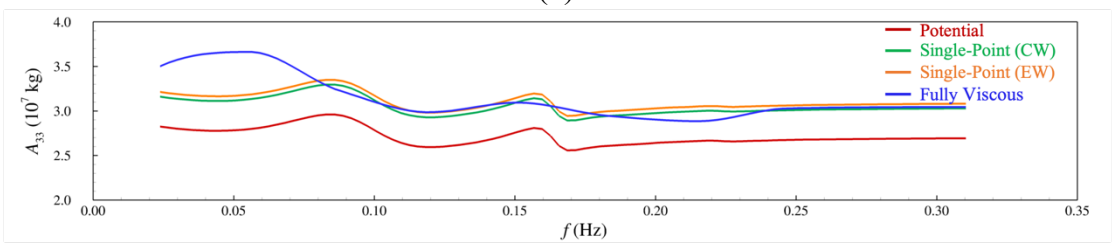

(c)

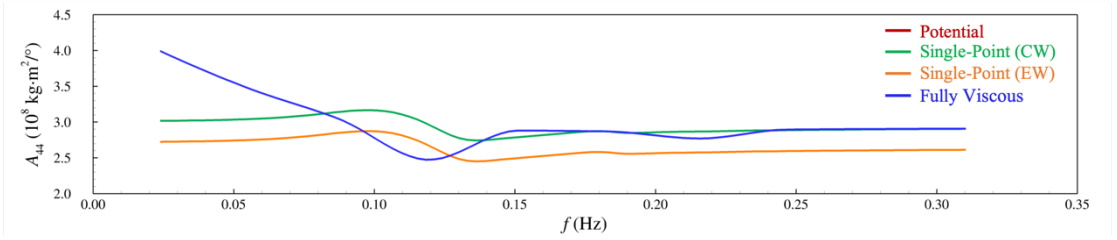

(d)

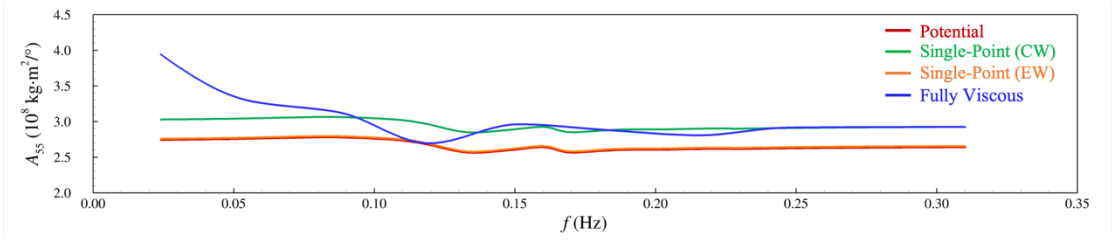

(e)

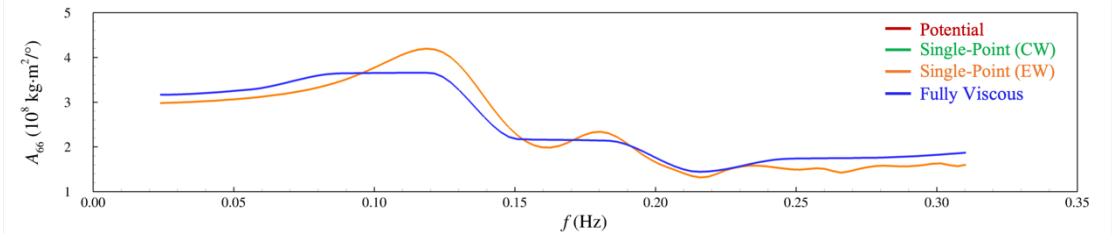

(f)

Figure 34 Added mass: (a) surge, (b) sway, (c) heave, (d) roll, (e) pitch, and (f) yaw

doi:10.6342/NTU202403052

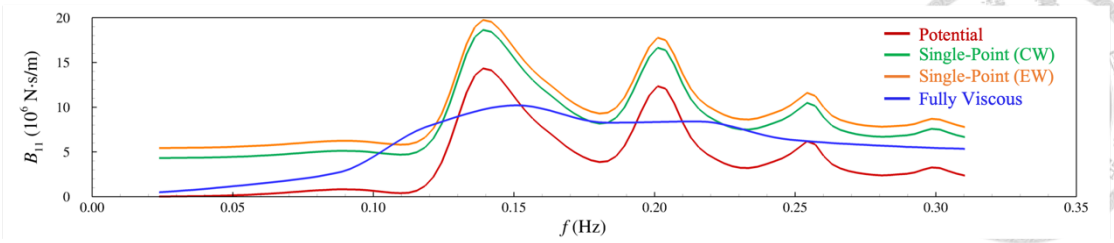

(a)

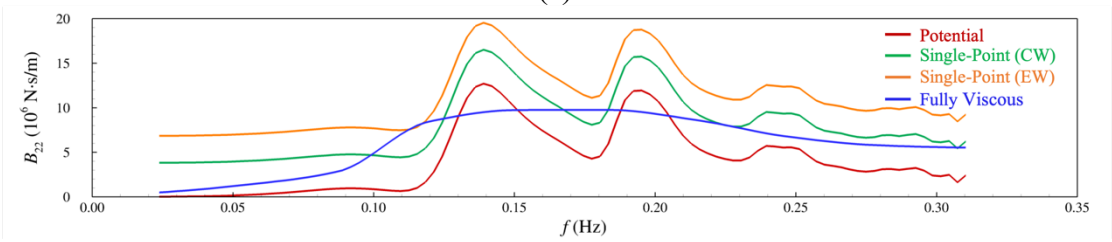

(b)

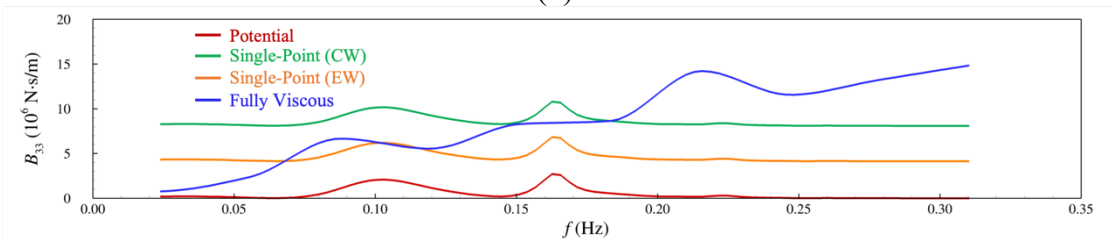

(c)

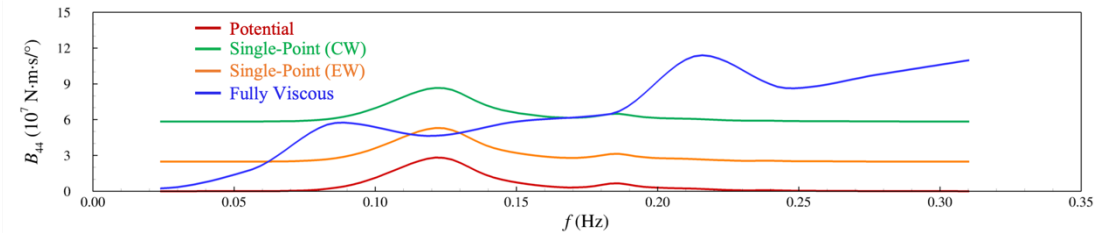

(d)

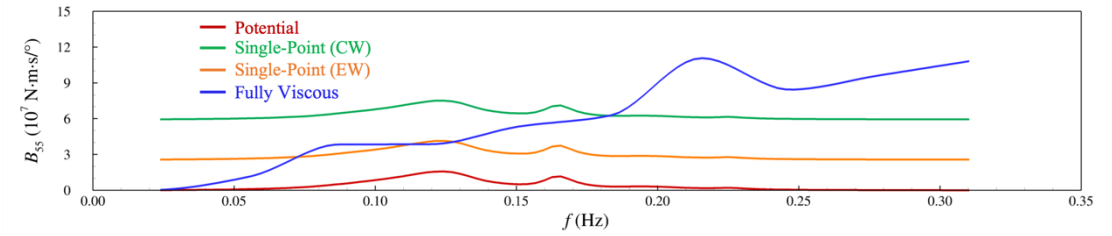

(e)

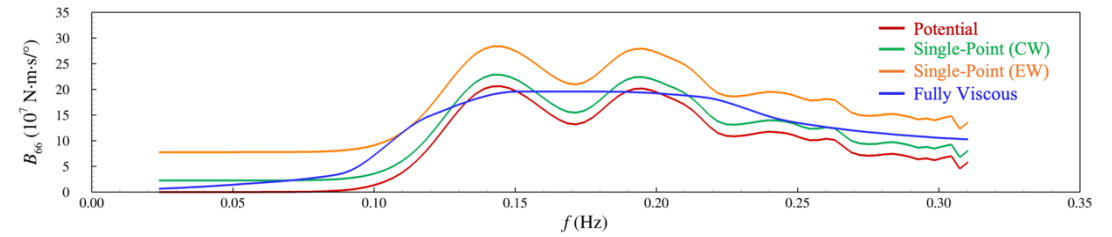

(f)

Figure 35 Damping: (a) surge, (b) sway, (c) heave, (d) roll, (e) pitch, and (f) yaw

doi:10.6342/NTU202403052

Table 13 Added mass predictions by (a) potential and (b) fully viscous methods

(a)

f	A_{11}	A_{22}	A_{33}	A_{44}	A_{55}	A_{66}
(Hz)	(10^7 kg)			(10^8 kg· m^2/°)		
0.0238	1.443	1.473	2.823	2.725	2.743	2.978
0.0557	1.504	1.542	2.800	2.749	2.760	3.099
0.0875	1.530	1.570	2.953	2.849	2.779	3.455
0.1193	2.073	2.082	2.595	2.689	2.683	4.195
0.1512	0.727	0.856	2.763	2.496	2.609	2.257
0.1830	1.016	1.301	2.610	2.575	2.593	2.302
0.2148	0.493	0.588	2.664	2.576	2.613	1.317
0.2467	0.811	0.708	2.675	2.595	2.626	1.496
0.2785	0.745	0.767	2.687	2.605	2.633	1.573
0.3103	0.751	0.780	2.695	2.611	2.640	1.601

(b)

f	A_{11}	A_{22}	A_{33}	A_{44}	A_{55}	A_{66}
(Hz)	(10^7 kg)			(10^8 kg· m^2/°)		
0.0238	1.543	1.582	3.503	3.995	3.953	3.165
0.0557	1.609	1.654	3.665	3.467	3.290	3.286
0.0875	1.564	1.572	3.231	3.041	3.129	3.641
0.1193	1.939	1.942	2.986	2.492	2.702	3.664
0.1512	0.751	0.859	3.091	2.879	2.961	2.187
0.1830	1.011	1.034	2.946	2.868	2.881	2.133
0.2148	0.647	0.674	2.886	2.770	2.807	1.439
0.2467	0.849	0.833	3.029	2.896	2.915	1.721
0.2785	0.859	0.872	3.043	2.904	2.922	1.762
0.3103	0.912	0.931	3.045	2.908	2.924	1.870

doi:10.6342/NTU202403052

Table 14 Damping predictions by (a) potential and (b) fully viscous methods

(a)

f	B_{11}	B_{22}	B_{33}	B_{44}	B_{55}	B_{66}
(Hz)	(10^6 N · s/m)			(10^7 N · m · s/°)		
0.0238	0.012	0.012	0.186	0.001	0.011	0.001
0.0557	0.217	0.226	0.062	0.005	0.093	0.003
0.0875	0.800	0.914	1.057	0.339	0.510	0.276
0.1193	1.187	1.644	1.251	2.717	1.497	7.960
0.1512	10.861	9.821	0.413	0.700	0.503	19.506
0.1830	3.962	5.952	0.543	0.642	0.306	17.319
0.2148	5.466	5.318	0.171	0.182	0.166	14.367
0.2467	4.532	5.546	0.023	0.043	0.042	11.319
0.2785	2.409	2.997	0.013	0.010	0.010	7.238
0.3103	2.346	2.415	0.015	0.011	0.011	5.818

(b)

f	B_{11}	B_{22}	B_{33}	B_{44}	B_{55}	B_{66}
(Hz)	(10^6 N · s/m)			(10^7 N · m · s/°)		
0.0238	0.481	0.488	0.750	0.224	0.022	0.648
0.0557	1.342	1.392	2.375	1.769	1.159	1.650
0.0875	2.683	2.848	6.649	5.750	3.837	3.454
0.1193	7.511	8.019	5.608	4.598	3.829	14.088
0.1512	10.334	9.841	8.256	5.884	5.350	19.703
0.1830	8.271	9.920	8.619	6.482	6.246	19.725
0.2148	8.332	8.522	14.220	11.401	11.069	18.443
0.2467	6.446	6.772	11.560	8.621	8.437	13.787
0.2785	5.708	5.853	13.226	9.799	9.628	11.563
0.3103	5.343	5.539	14.837	10.985	10.821	10.279

doi:10.6342/NTU202403052

8.2 Load Response Amplitude Operator

This study employs Ansys Aqwa to determine the load response amplitude operator (Load RAO) without the mooring system. Figure 36 illustrates the Load RAO, characterized under various incoming wave directions. For surge motion, a maximum value of 11.5 MN/m is observed at $\theta_w = 0°$ and 0.14 Hz. For sway motion a peak of 10.5 MN/m occurs at $\theta_w = 120°$ and 0.14 Hz. In heave motion, all θ_w show a maximum value of 5.4 MN/m at 0.025 Hz, with another peak at 0.1 Hz, exhibiting similar trends of θ_w. For roll motion, a maximum of 130 MN/m is observed at $\theta_w = 90°$ and 0.12 Hz. In pitch motion, the peak value is 90 MN/m at $\theta_w = 0°$ and 0.12 Hz. For yaw motion, a maximum of 300 MN/m is noted at $\theta_w = 0°$ and 0.13 Hz, with similar trends across wave directions. These results indicate that the studied FOWT exhibits varying Load RAOs under various incident waves.

doi:10.6342/NTU202403052

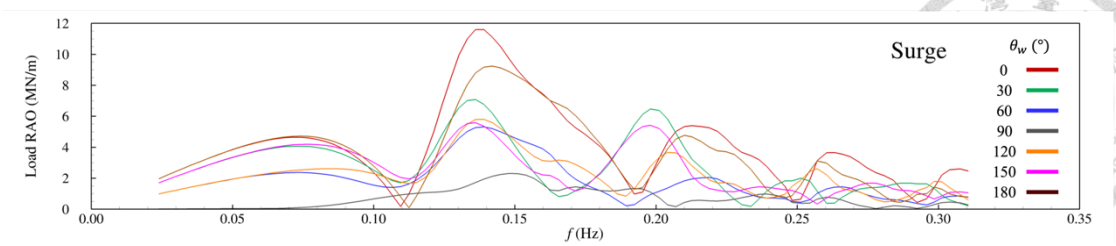

(a)

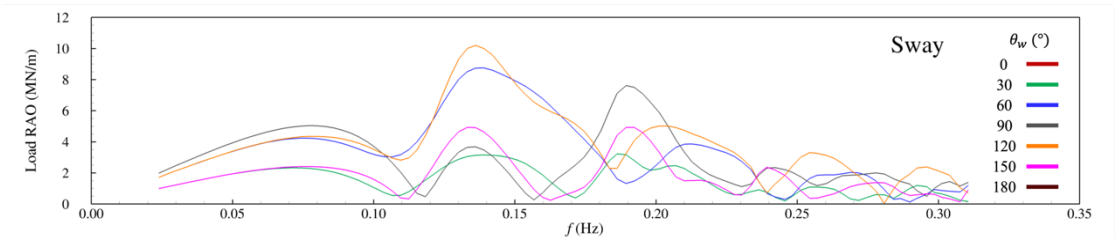

(b)

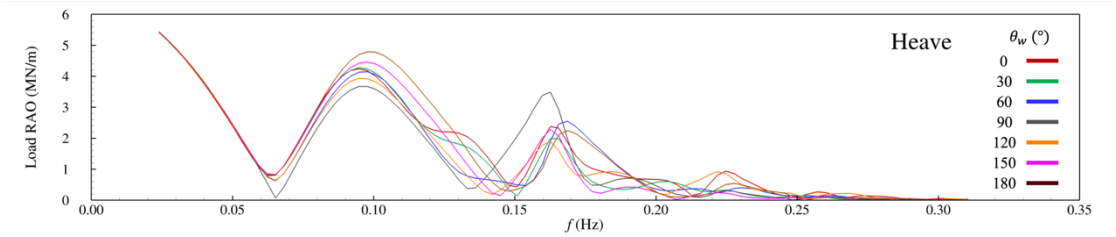

(c)

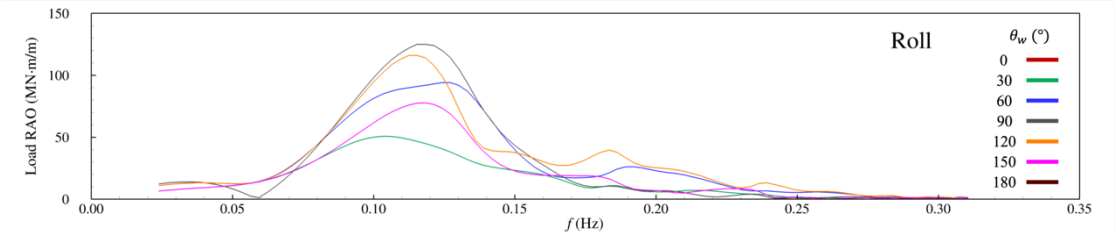

(d)

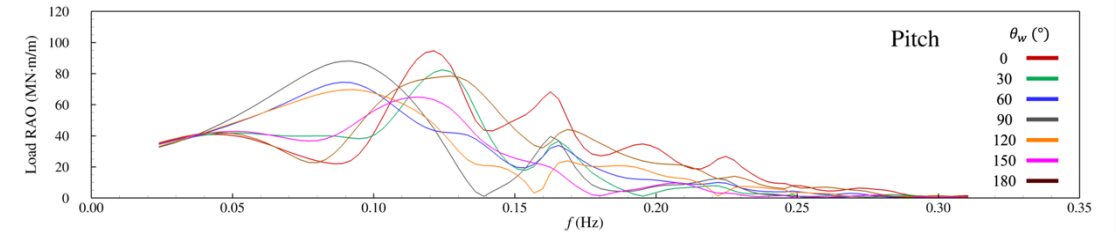

(e)

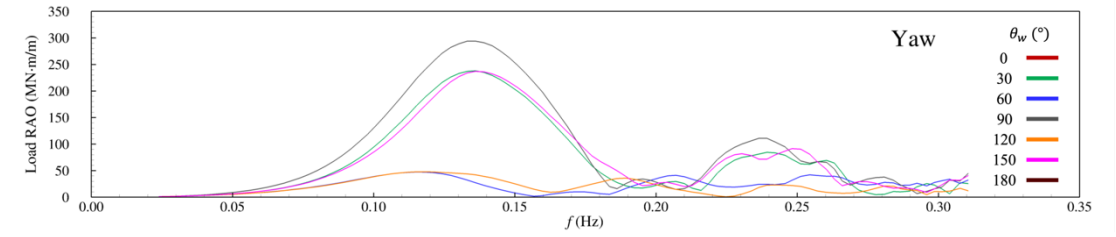

(f)

Figure 36 Load RAO: (a) surge, (b) sway, (c) heave, (d) roll, (e) pitch, and (f) yaw

doi:10.6342/NTU202403052

8.3 Motion Response

The motion response is determined by solving the equations of motion using OrcaFlex. From the time-domain results in OrcaFlex, the mean value (η_i^m), maximum value (η_i^M) and standard deviation (σ_{η_i}) are analyzed. Where η_i represents linear and angular displacements, and $i = 1, 2, \ldots, 6$ correspond to 6DOF motions, respectively. This study simulates total 7200 s and analyzes the last 3600 s. Figure 37 shows the time histories from 3600 s to 7200 s of the 6DOF motions at $\theta_w = 0°$. Section 8.3.1 discusses the motion response using different hydrodynamic property prediction methods, whereas Section 8.3.2 examines the LTC scenario.

8.3.1 Comparison of Motion Response among Methods

The mean, maximum, and standard deviations of the motions at $\theta_w = 0°$ under the CW and EW conditions using three hydrodynamic property predictions methods are depicted in Figs. 38 and 39 as well as Table 15.

For the surge motion under the CW condition, the mean values of single-point method and fully viscous method are 4.54% and 3.09% lower than those of potential method, respectively; the maximum values of single-point method and fully viscous method are 26.4% and 11.94% lower than those of potential method, respectively; and the standard deviations of single-point method and fully viscous method are 50.68% and 26.99% lower than those of potential method, respectively. Under the EW condition, the mean values of single-point method and fully viscous method are 7.21% and 5.2% higher than the potential method, respectively; the maximum values of single-point method and fully viscous method are 13.05% and 1.01% lower than those of potential method,

doi:10.6342/NTU202403052

respectively; and the standard deviations of single-point method and fully viscous method are 18.16% and 6.65% lower than those of potential method, respectively.

For the sway motion under the CW condition, the mean values of single-point method and fully viscous method are 1.87% and 3.74% lower than those of potential method, respectively; the maximum values of single-point method and fully viscous method are 45.98% and 21.34% lower than those of potential method, respectively; and the standard deviations of single-point method and fully viscous method are 50.85% and 15.18% lower than those of potential method, respectively. Under the EW condition, the mean values of single-point method and fully viscous method are 39.8% and 38.42% higher than the potential method, respectively; the maximum values of single-point method and fully viscous method are 97.52% and 93.69% lower than those of potential method, respectively; and the standard deviations of single-point method and fully viscous method are 97.24% and 92.08% lower than those of potential method, respectively.

For the heave motion under the CW condition, the mean values of single-point method and fully viscous method methods are 7% and 6.88% lower than those of potential method, respectively; the maximum values of single-point method and fully viscous method are 9.96% and 5.01% lower than those of potential method, respectively; and the standard deviations of single-point method and fully viscous method are 19.37% and 17.06% lower than those of potential method, respectively. Under the EW condition, the mean values of single-point method and fully viscous method remain 7% and 6.88% lower than those of potential method, respectively; the maximum values of single-point method and fully viscous method are 26.59% and 19.3% lower than those of potential method, respectively; and the standard deviations of the single-point method and fully viscous method are 28.9% and 33.94% lower than those of potential method, respectively.

doi:10.6342/NTU202403052

For the roll motion under the CW condition, the mean values of single-point method and fully viscous method are 0.1% and 0.03% higher than the potential method, respectively; the maximum values of the single-point method and fully viscous method are 25.77% and 3.29% lower than those of potential method, respectively; and the standard deviations of single-point method and fully viscous method are 58.48% and 3.07% lower than those of potential method, respectively. Under the EW condition, the mean values of single-point method and fully viscous method are 20.03% and 17.83% lower than those of potential method, respectively; the maximum values of single-point method and fully viscous method are 92.66% and 92.05% lower than those of potential method, respectively; and the standard deviations of single-point method and fully viscous method are 97.94% and 97.12% lower than those of potential method, respectively.

For the pitch motion under the CW condition, the mean values of single-point method and fully viscous method are 24.62% and 25.24% lower than those of potential method, respectively; the maximum values of single-point method and fully viscous method are 21.69% and 13.97% lower than those of potential method, respectively; and the standard deviations of single-point method and fully viscous method are 13.23% and 1.44% lower than those of potential method, respectively. Under the EW condition, the mean values of single-point method and fully viscous method are 74.65% and 11.39% higher han the potential method, respectively; the maximum values of single-point method and fully viscous method are 11.31% and 20.46% lower than those of potential method, respectively; and the standard deviations of single-point method and fully viscous method are 20.4% and 15.69% lower than those of potential method, respectively.

For the yaw motion under the CW condition, the mean values of single-point method and fully viscous method are 66.29% and 53.71% higher than the potential method,

doi:10.6342/NTU202403052

respectively; the maximum values of single-point method and fully viscous method are 52.62% and 25.25% lower than those of potential method, respectively; and the standard deviations of single-point method and fully viscous method are 56.42% and 31.74% less than the potential method, respectively. Under EW conditions, the mean values of single-point method and fully viscous method are 1.08% lower and 0.82% higher than the potential method, respectively; the maximum values of single-point method and fully viscous method are 98.16% and 96.88% lower than those of potential method, respectively; and the standard deviations of single-point method and fully viscous method are 99.21% and 98.01% lower than those of potential method, respectively.

These findings suggest that damping significantly affects the motion response more than added mass. Moreover, while incorporating viscous effects does not substantially change the mean values, it does result in a marked decrease in both maximum values and standard deviations. It was also observed that the maximum values and standard deviations are influenced by the magnitude of damping at frequencies corresponding to the peaks in the wave spectral density under specific metocean conditions. Higher damping at these frequencies leads to smaller maximum values and standard deviations. Additionally, the damping calculated using the single-point method tends to be overestimated, resulting in underestimating the maximum values and standard deviations.

doi:10.6342/NTU202403052

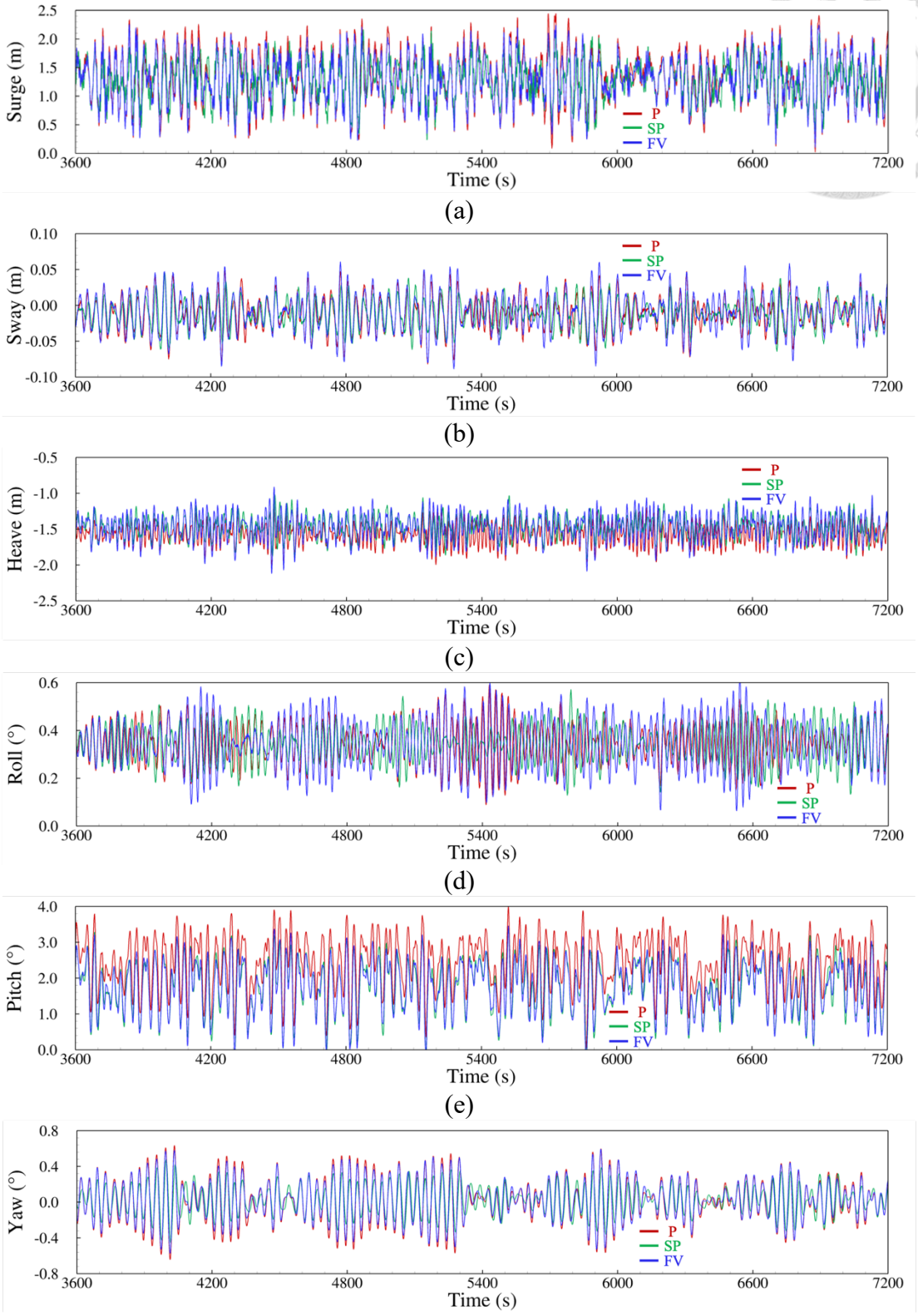

Figure 37 Time-domain predictions of platform 6DOF motions under CW, showing (a) surge, (b) sway, (c) heave, (d) roll, (e) pitch, and (f) yaw motion

doi:10.6342/NTU202403052

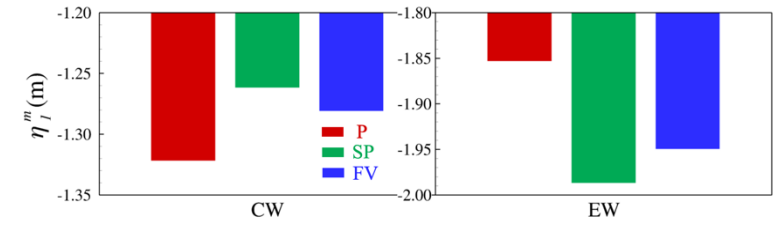

(a)

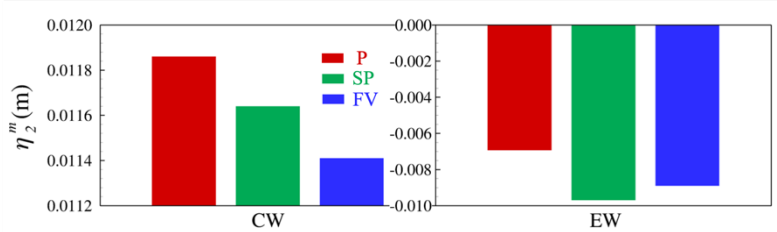

(b)

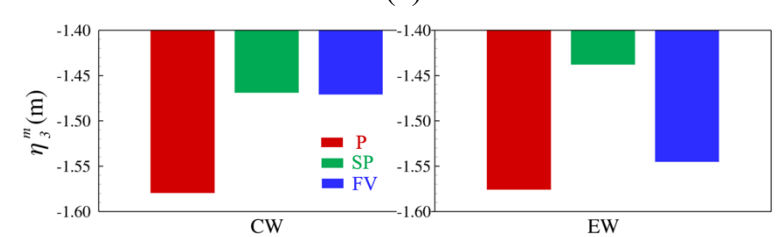

(c)

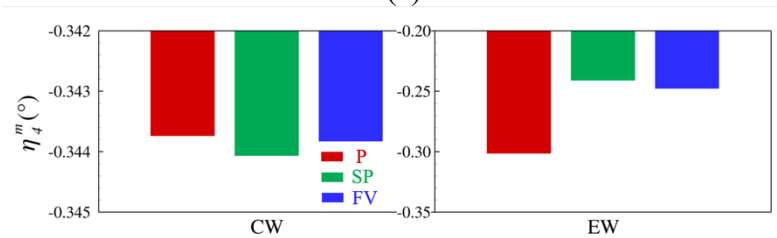

(d)

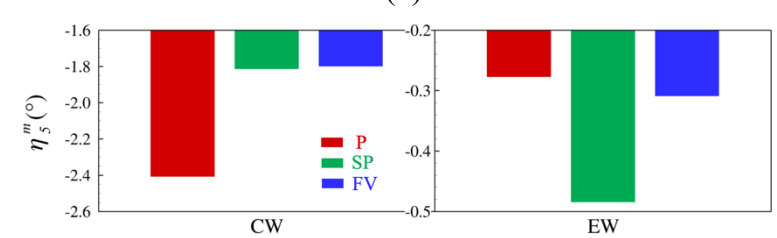

(e)

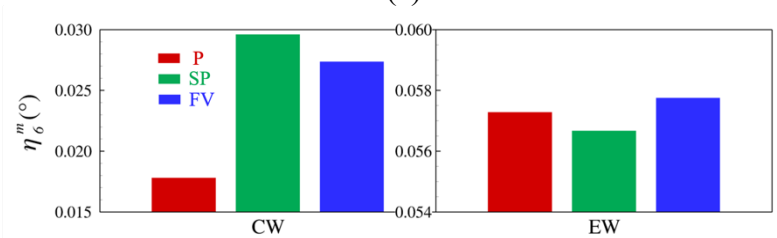

(f)

Figure 38 Average platform motion under CW and EW conditions: (a) surge, (b) sway, (c) heave, (d) roll, (e) pitch, and (f) yaw

doi:10.6342/NTU202403052

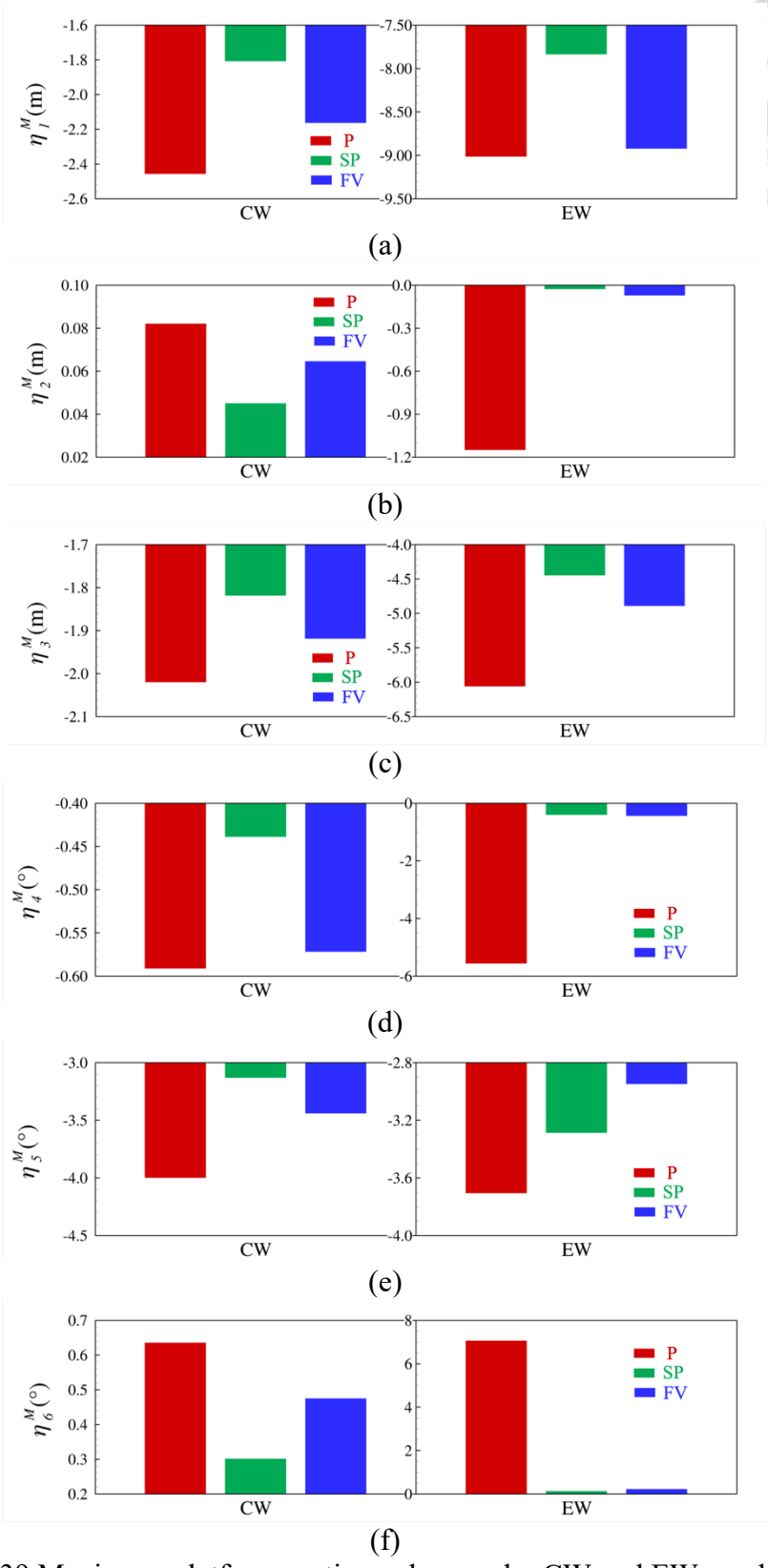

Figure 39 Maximum platform motion values under CW and EW conditions for:

(a) surge, (b) sway, (c) heave, (d) roll, (e) pitch, and (f) yaw

doi:10.6342/NTU202403052

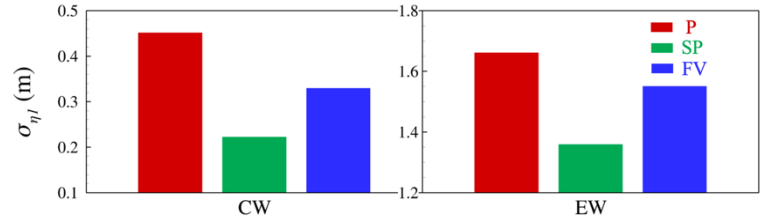

(a)

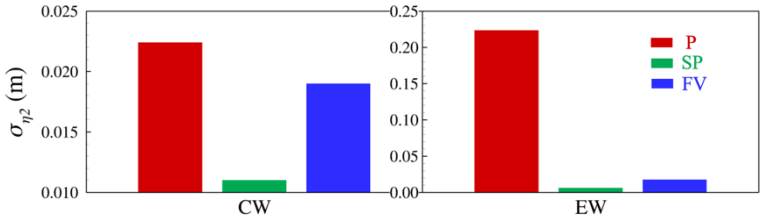

(b)

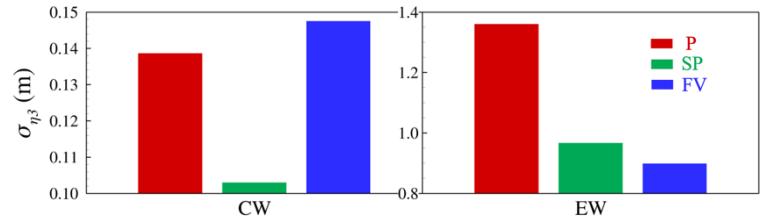

(c)

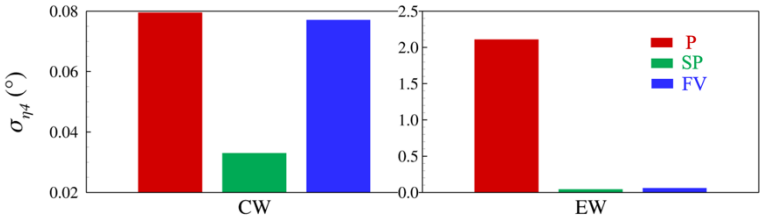

(d)

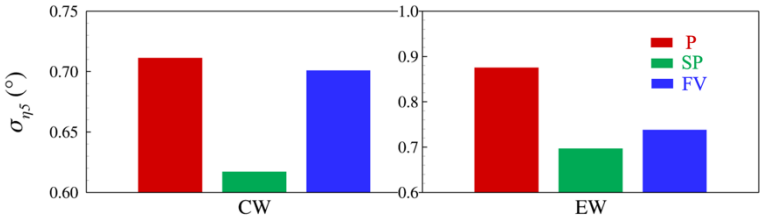

(e)

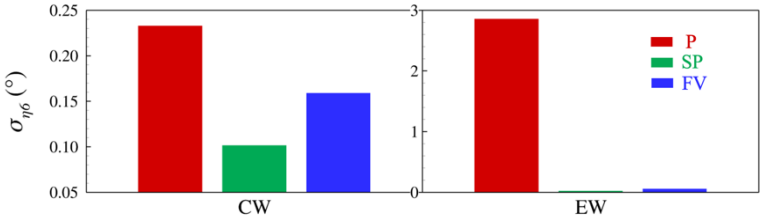

(f)

Figure 40 Standard deviation of platform motion under CW and EW conditions: (a) surge, (b) sway, (c) heave, (d) roll, (e) pitch, and (f) yaw

doi:10.6342/NTU202403052

Table 15 Platform 6 DOF motions in $\theta_w = 0°$ under CW, and EW conditions: (a) surge, (b) sway, (c) heave, (d) roll, (e) pitch, and (f) yaw

(a)

Method	Mean (m)		Max (m)		Std (m)	
	CW	EW	CW	EW	CW	EW
P	-1.322	-1.853	-2.458	-9.015	0.451	1.661
SP	-1.262	-1.987	-1.809	-7.839	0.223	1.360
FV	-1.281	-1.950	-2.164	-8.923	0.330	1.551

(b)

Method	Mean (m)		Max (m)		Std (m)	
	CW	EW	CW	EW	CW	EW
P	0.012	-0.007	0.082	-1.150	0.022	0.224
SP	0.012	-0.010	0.045	-0.029	0.011	0.006
FV	0.011	-0.009	0.065	-0.073	0.019	0.018

(c)

Method	Mean (m)		Max (m)		Std (m)	
	CW	EW	CW	EW	CW	EW
P	-1.580	-1.576	-2.020	-6.061	0.139	1.360
SP	-1.469	-1.438	-1.819	-4.449	0.103	0.967
FV	-1.471	-1.545	-1.919	-4.892	0.148	0.899

(d)

Method	Mean (°)		Max (°)		Std (°)	
	CW	EW	CW	EW	CW	EW
P	-0.344	-0.302	-0.591	-5.567	0.080	2.110
SP	-0.344	-0.241	-0.439	-0.408	0.033	0.044
FV	-0.344	-0.248	-0.572	-0.443	0.077	0.061

(e)

Method	Mean (°)		Max (°)		Std (°)	
	CW	EW	CW	EW	CW	EW
P	-2.408	-0.278	-4.000	3.707	0.711	0.875
SP	-1.815	-0.485	-3.133	3.288	0.617	0.697
FV	-1.800	-0.309	-3.442	2.949	0.701	0.738

(f)

Method	Mean (°)		Max (°)		Std (°)	
	CW	EW	CW	EW	CW	EW
P	0.018	0.057	0.635	7.064	0.233	2.856
SP	0.030	0.057	0.301	0.130	0.101	0.023
FV	0.027	0.058	0.475	0.220	0.159	0.057

doi:10.6342/NTU202403052

8.3.2 LTC Scenario

The simulation results under LTC scenario are illustrated in Figs. 41 and 42, and detailed in Table 16, comparing the effects between spectrum, as well as the impact of viscous effects.

For the surge motion, moving in the +*x* direction occurs when $\theta_w = 135°, 225°$, while moving in the -*x* direction happens when $\theta_w = 45°, 315°$. For the maximum values, comparing between spectrums reveal that using the potential method, API values are 16.04% to 23.29% larger than those of constant wind speed, while when using the fully viscous method, API values are 9.34% to 15.78% larger than those of constant wind speed. When comparing the potential method and fully viscous method under the constant wind speed, the fully viscous method values are 1.72% to 3.85% larger than those of potential method, while under API, the fully viscous method values are 8.96% smaller to 2.56% larger than those of potential method. For the standard deviations are higher for API compared to constant wind speed, and for potential method compared to fully viscous method.

For the sway motion, moving in the +*y* direction occurs when $\theta_w = 225°, 315°$, while moving in the -*y* direction happens when $\theta_w = 45°, 135°$. For the maximum values, comparing between spectrums reveal that using the potential method, API values are 2.89% smaller to 24.51% larger than those of constant wind speed, while when using the fully viscous method, API values are 5.34% to 25.09% larger than those of constant wind speed. When comparing the potential method and fully viscous method under the constant wind speed, the fully viscous method values are 7.19% to 8.99% larger than those of potential method, while under API, the fully viscous method values are 13.69% smaller to 15.86% larger than those of potential method. For the standard deviations are higher

doi:10.6342/NTU202403052

for API compared to constant wind speed, and for potential method compared to fully viscous method.

For the heave motion, concerning the maximum value, comparing between spectrums reveal that using the potential method, API values are 0.2% to 1.04% larger than those of constant wind speed, while when using the fully viscous method, API values are 0.2% to 1.04% larger than those of constant wind speed. When comparing the potential method and fully viscous method under the constant wind speed, the fully viscous method values are 2.31% smaller to 3.71% larger than those of potential method, while under API, the fully viscous method values are 0.05% to 5.65% larger than those of potential method. For the standard deviations are higher for API compared to constant wind speed, and for potential method compared to fully viscous method.

For the roll motion, rotating in the +*x* direction occurs when $\theta_w = 45°, 135°$, while rotating in the -*x* direction happens when $\theta_w = 225°, 315°$. For the maximum values, comparing between spectrums reveal that using the potential method, API values are 21.13% to 29.85% larger than those of constant wind speed, while when using the fully viscous method, API values are 14.95% to 24.04% larger than those of constant wind speed. When comparing the potential method and fully viscous method under the constant wind speed, the fully viscous method values are 0.02% smaller to 1.22% larger than those of potential method, while under API, the fully viscous method values are 1.63% to 7.57% smaller than those of potential method. For the standard deviations are higher for API compared to constant wind speed, and for potential method compared to fully viscous method.

For the pitch motion, rotating in the +*y* direction occurs when $\theta_w = 135°, 225°$, while rotating in the -*y* direction happens when $\theta_w = 45°, 315°$. For the maximum values, comparing between spectrums reveal that using the potential method, API values

doi:10.6342/NTU202403052

are 21.13% to 29.85% larger than those of constant wind speed, while when using the fully viscous method, API values are 30.55% to 64.74% larger than those of constant wind speed. When comparing the potential method and fully viscous method under the constant wind speed, the fully viscous method values are 31.05% smaller to 23.43% larger than those of potential method, while under API, the fully viscous method values are 18.83% smaller to 22.64% larger than those of potential method. For the standard deviations are higher for API compared to constant wind speed, and for potential method compared to fully viscous method.

For the yaw motion, rotating in the +z direction occurs when $\theta_w = 45°, 135°$, while rotating in the -z direction happens when $\theta_w = 225°, 315°$. For the maximum values, comparing between spectrums reveal that using the potential method, API values are 29.21% to 34.72% larger than those of constant wind speed, while when using the fully viscous method, API values are 8.82% to 18.45% larger than those of constant wind speed. When comparing the potential method and fully viscous method under the constant wind speed, the fully viscous method values are 2.57% to 4.85% smaller than those of potential method, while under API, the fully viscous method values are 11.69% to 22.95% smaller than those of potential method. For the standard deviations are higher for API compared to constant wind speed, and for potential method compared to fully viscous method.

These results highlight that due to the time-varying nature of wind speeds in the API spectrum, as illustrated in Fig. 29, using the API spectrum results in higher maximum values and standard deviations in platform motions compared to constant wind speed. This underscores the significance of accurately modeling wind speed variations. The effect of viscous damping considerably reduces standard deviations and occasionally decreases maximum values, thereby enhancing the accuracy of motion predictions. Therefore, incorporating both wind spectrum and viscous effects is essential for reliable

doi:10.6342/NTU202403052

long-term scenario of offshore wind turbine platforms, aiding in better design and operational strategies for improved performance and safety.

doi:10.6342/NTU202403052

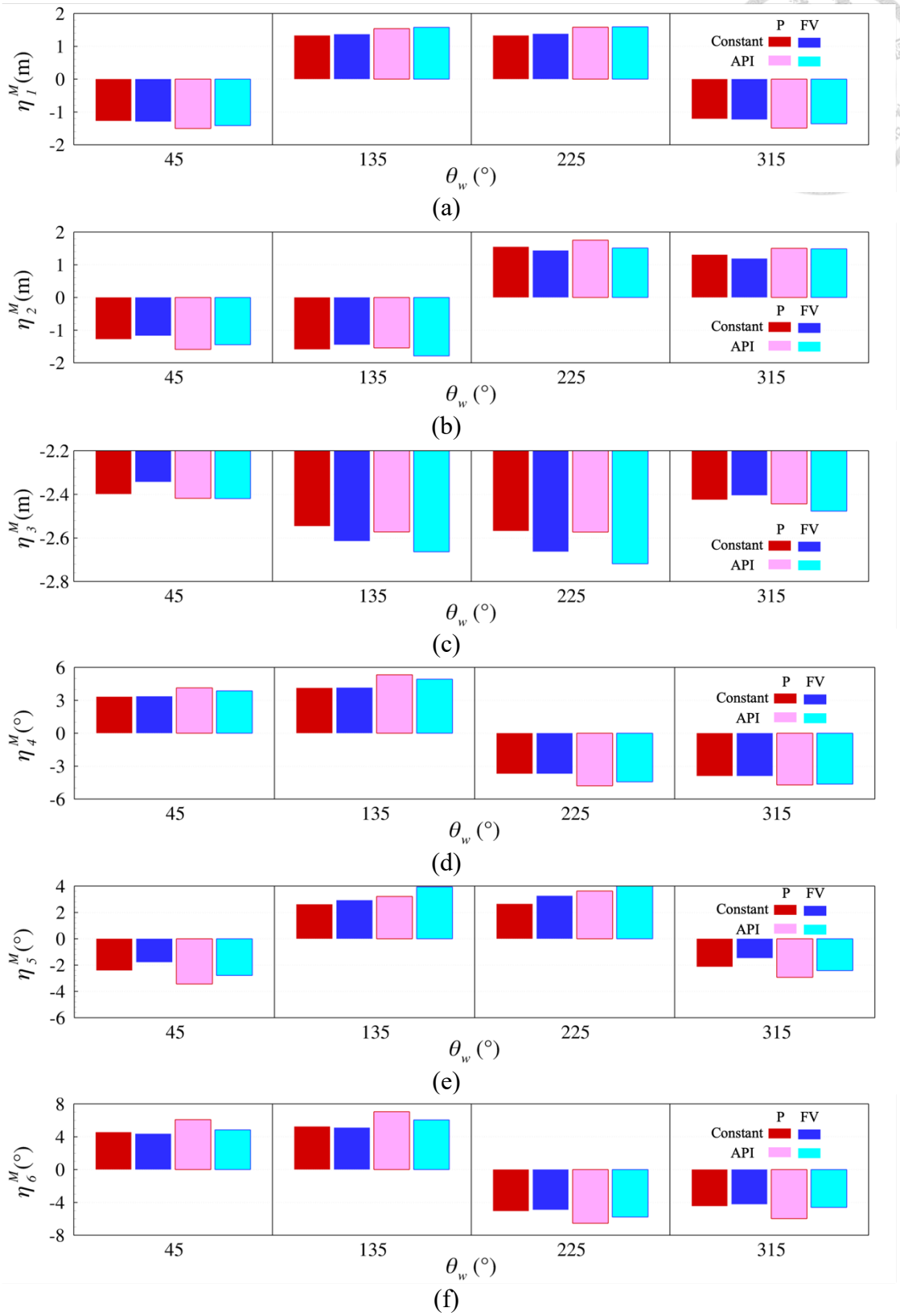

Figure 41 Maximum platform motion values under LTC scenario: (a) surge, (b) sway, (c) heave, (d) roll, (e) pitch, and (f) yaw

doi:10.6342/NTU202403052

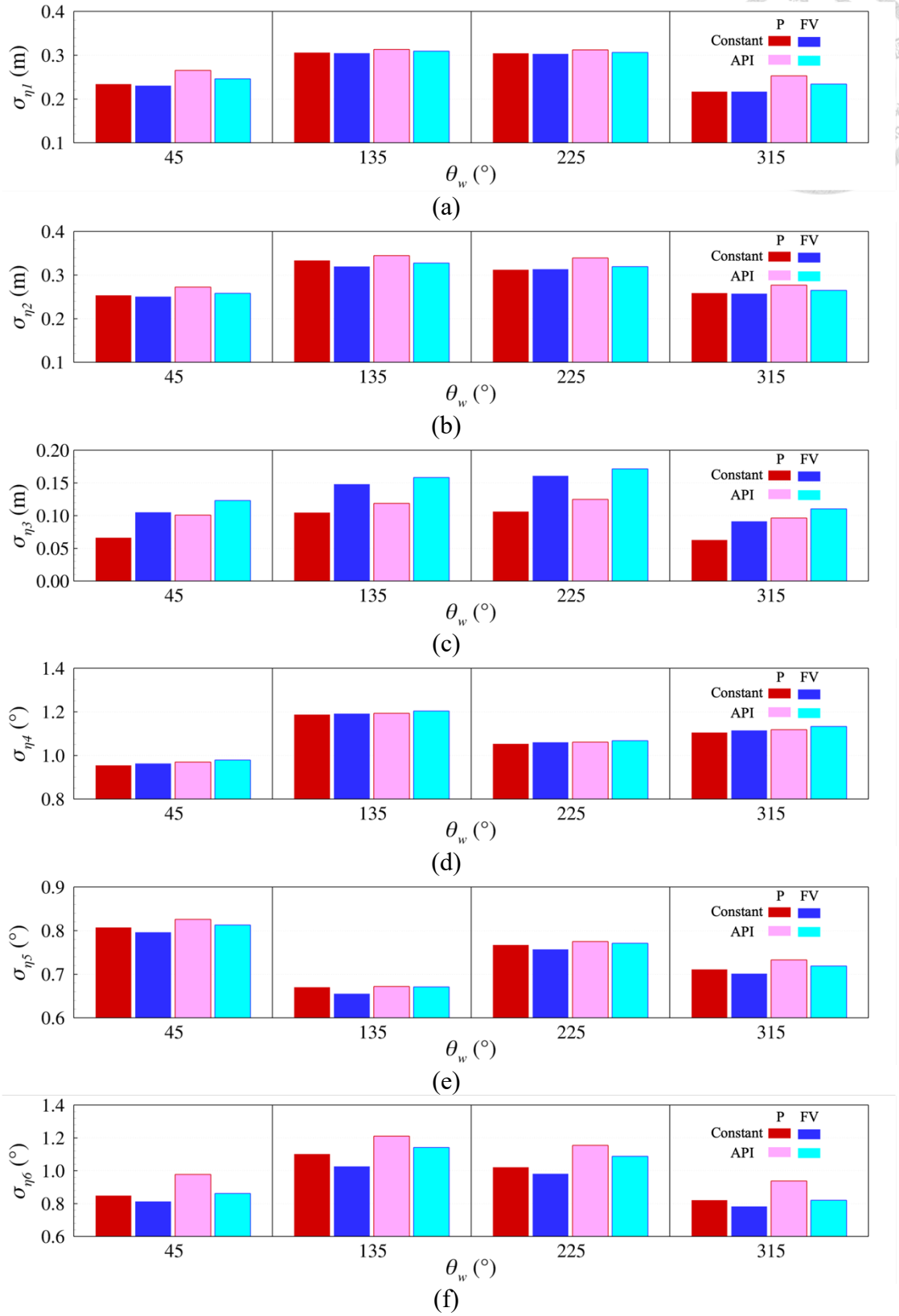

Figure 42 Standard deviation of platform motion under LTC scenario: (a) surge, (b) sway, (c) heave, (d) roll, (e) pitch, and (f) yaw

doi:10.6342/NTU202403052

Table 16 Platform 6 DOF motions under LTC scenario: (a) surge, (b) sway, (c) heave, (d) roll, (e) pitch, and (f) yaw

(a)

Spectrum		Max (m)				Std (m)			
	θ_w	45°	135°	225°	315°	45°	135°	225°	315°
Constant	P	-1.273	1.326	1.329	-1.210	0.234	0.306	0.304	0.217
	FV	-1.296	1.365	1.380	-1.231	0.230	0.305	0.303	0.217
API	P	-1.502	1.539	1.582	-1.492	0.265	0.313	0.312	0.253
	FV	-1.418	1.578	1.598	-1.358	0.246	0.310	0.307	0.234

(b)

Spectrum		Max (m)				Std (m)			
	θ_w	45°	135°	225°	315°	45°	135°	225°	315°
Constant	P	-1.276	-1.589	1.548	1.305	0.253	0.333	0.314	0.259
	FV	-1.168	-1.446	1.437	1.190	0.250	0.319	0.313	0.257
API	P	-1.589	-1.543	1.754	1.503	0.273	0.345	0.339	0.277
	FV	-1.446	-1.787	1.514	1.489	0.258	0.328	0.319	0.265

(c)

Spectrum		Max (m)				Std (m)			
	θ_w	45°	135°	225°	315°	45°	135°	225°	315°
Constant	P	-2.398	-2.546	-2.568	-2.424	0.066	0.105	0.106	0.063
	FV	-2.343	-2.615	-2.663	-2.405	0.105	0.148	0.161	0.091
API	P	-2.418	-2.572	-2.573	-2.444	0.101	0.119	0.125	0.096
	FV	-2.420	-2.664	-2.719	-2.477	0.123	0.158	0.172	0.110

(d)

Spectrum		Max (°)				Std (°)			
	θ_w	45°	135°	225°	315°	45°	135°	225°	315°
Constant	P	3.320	4.130	-3.695	-3.895	0.955	1.187	1.053	1.105
	FV	3.360	4.146	-3.695	-3.900	0.963	1.192	1.060	1.115
API	P	4.142	5.333	-4.798	-4.719	0.970	1.193	1.061	1.119
	FV	3.863	4.934	-4.435	-4.642	0.979	1.204	1.068	1.133

(e)

Spectrum		Max (°)				Std (°)			
	θ_w	45°	135°	225°	315°	45°	135°	225°	315°
Constant	P	-2.417	2.615	2.643	-2.135	0.807	0.670	0.767	0.711
	FV	-1.788	2.925	3.262	-1.472	0.796	0.655	0.757	0.701
API	P	-3.438	3.216	3.622	-2.932	0.826	0.672	0.775	0.733
	FV	-2.791	3.944	4.259	-2.425	0.813	0.671	0.771	0.719

(f)

Spectrum		Max (°)				Std (°)			
	θ_w	45°	135°	225°	315°	45°	135°	225°	315°
Constant	P	4.542	5.244	-5.065	-4.447	0.848	1.102	1.021	0.821
	FV	4.362	5.109	-4.906	-4.231	0.813	1.026	0.981	0.783
API	P	6.088	7.064	-6.544	-5.976	0.977	1.211	1.155	0.938
	FV	4.850	6.052	-5.779	-4.604	0.862	1.142	1.088	0.820

doi:10.6342/NTU202403052

8.4 Power Performance

The generator power is determined by solving the equations of motion in OrcaFlex. From the time-domain results in OrcaFlex, the mean value (P^m) and standard deviation (σ_p) are analyzed. Section 8.4.1 examines generator power under CW condition using different hydrodynamic property methods, while Section 8.4.2 explores the power characteristics under LTC scenario.

8.4.1 Comparison of Power Performance among Methods

Figure 43 and Table 17 illustrate the mean values and standard deviations of the generator power in $\theta_w = 0°$ under CW condition using various hydrodynamic property prediction methods.

Under CW condition, the mean power value using the potential method is 14.56 MW with a standard deviation of 1.1 MW. The mean values obtained using the single-point and fully viscous methods are 0.35% and 0.16% higher than that of using the potential method, respectively, while their standard deviations are 12.41% and 3.9% lower than that of potential method.

These findings indicate that power generation is influenced by the magnitude of the platform's motion, with more unstable motion leading to lower power generation. The single-point method, on the other hand, which tends to underestimate motion, results in slightly higher predicted power generation. However, the differences among the three methods are pretty limited, suggesting that the most time-efficient potential flow method can effectively predict power generation.

doi:10.6342/NTU202403052

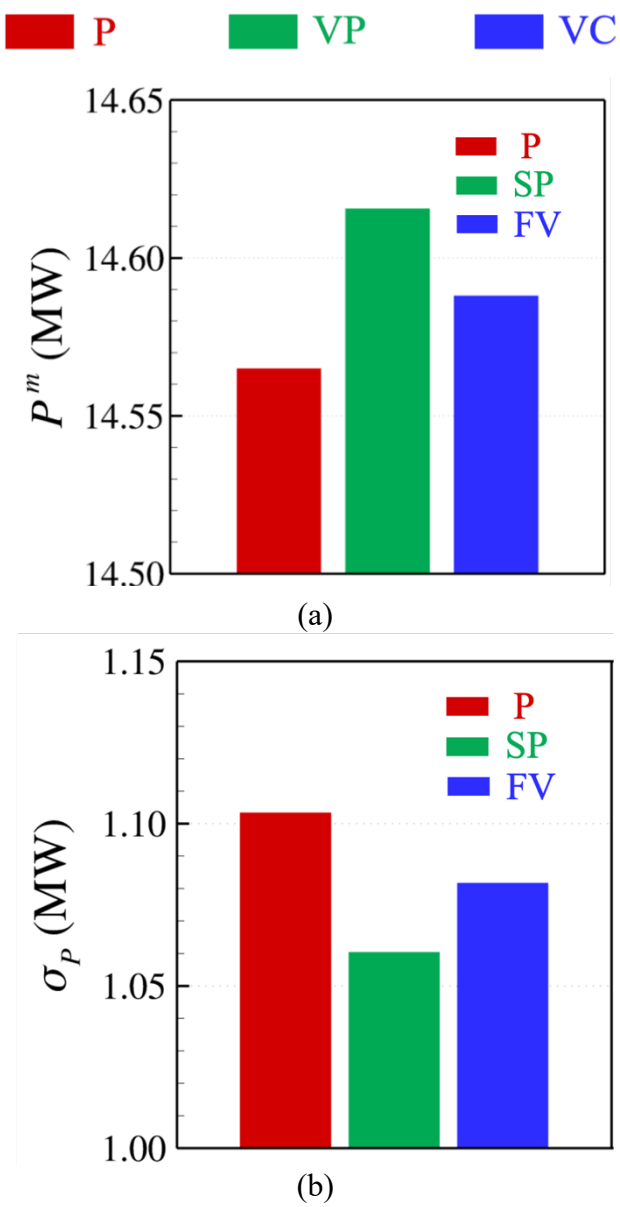

Figure 43 Power generation under CW condition:(a) Mean, and (b) standard deviation

Table 17 Power generation under CW condition

Method	Mean (MW)	Std (MW)
P	14.56	1.10
SP	14.62	0.97
FV	14.59	1.06

doi:10.6342/NTU202403052

8.4.2 LTC Scenario

This section examines power characteristics under LTC scenario, comparing the differences between wind spectrums, as well as the impact of the viscous effect. The weighted power characteristics P^m and the weighted capacity factor *CF* are calculated as follows:

$$P^m = \sum_{i=1}^{n} P_l^m q_l \,, \tag{130}$$

$$CF = \frac{P^m}{P_r}, \tag{131}$$

where P_l^m represents the generator power for the l-th sea state, as detailed in Table 18, q_l is the probability of occurrence of the i-th sea state, and P_r is the rated generator power.

Table 18 Power prediction (MW) for each wave condition using the fully viscous method and API spectrum

H_s (m) \ T_z (s)	3.5	4.5	5.5	6.5	7.5
0.25	0.519	0.519	0.519		
0.50	1.888	1.888	1.888		
0.75	3.242	3.243	3.243	3.243	
1.00	8.178	8.178	8.179	8.178	
1.25	12.891	12.892	12.893	12.891	
1.50		14.477	14.477	14.478	
1.75		14.732	14.732	14.733	
2.50		14.896	14.895	14.895	14.896
3.50			14.869	14.869	
4.50				14.671	

Using the wave scatter diagram, the theoretical power output of the wind turbine is calculated to be 7.817 MW, on wind speed of the hub height mapping to the power curve. This value deviates by only 1% to 2% from the four cases examined in this study, indicating a close alignment between the simulation and theoretical values. The power

doi:10.6342/NTU202403052

characteristics is shown in Fig. 44 (a) and Table 19 (a). The standard deviation of the power characteristics is depicted in Fig. 44 (b) and Table 19 (b), while the capacity factor (*CF*) is presented in Fig. 44 (c) and Table 20. Figure 45 and Table 21 show the dependence of P^m and σ_p on H_s.

When comparing the mean power at different θ_w between spectrums reveal that using the potential method, API values are 0.66% to 0.69% lower than those of constant wind speed, while when using the fully viscous method, API values are 0.63% to 0.69% lower than those of constant wind speed. When comparing the potential method and the fully viscous method under the constant wind speed, the fully viscous method values are 0.18% lower to 0.23% higher than those of potential method, while under API, the fully viscous method values are 0.11% lower to 0.22% higher than those of potential method. Regarding the standard deviation of power, using API consistently show higher values than those using constant wind speed., and similarly, cases using the potential method always show higher values than those using the fully viscous method.

For the weighted power under constant wind speed, the values using the potential method and the fully viscous method values are 7.724 MW and 7.731 MW, respectively, while under API, values using the potential method and the fully viscous method values are 7.672 MW and 7.68 MW, respectively. Regarding the standard deviation of weighted power, under constant wind speed, values using the potential method and the fully viscous method values are 0.096 MW and 0.082 MW, respectively, while under API, values using the potential method and the fully viscous method values are 0.835 MW and 0.825 MW, respectively.

For the weighted capacity factor under constant wind speed, the values using the potential method and the fully viscous method values are both 0.515, while under API,

doi:10.6342/NTU202403052

values using the potential method and the fully viscous method values are 0.511 and 0.512, respectively.

For mean power characteristics under varying H_s, there is minimal difference between using the potential and the fully viscous methods. When applying API, power characteristics exceeds constant wind speed for $H_s < 1.25$ m, but falls short for $H_s > 1.25$ m. Regarding the standard deviation of power characteristics across different H_s, the difference between the potential and the fully viscous methods are insignificant.

The findings suggest that viscous effects have a negligible impact on power characteristics. The differences between using constant wind speed. and API are more pronounced, though still less than 1%. The four results analyzed in this study closely align with theoretical power performance, with a difference of 1% to 2%. It shows that to roughly estimate power characteristics, theoretical values can be used.

doi:10.6342/NTU202403052

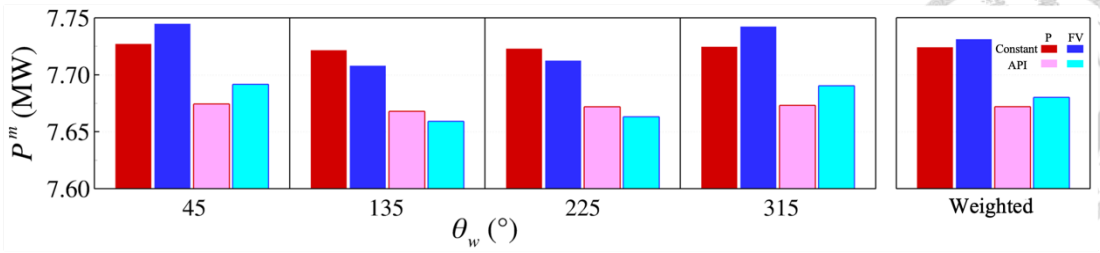

(a)

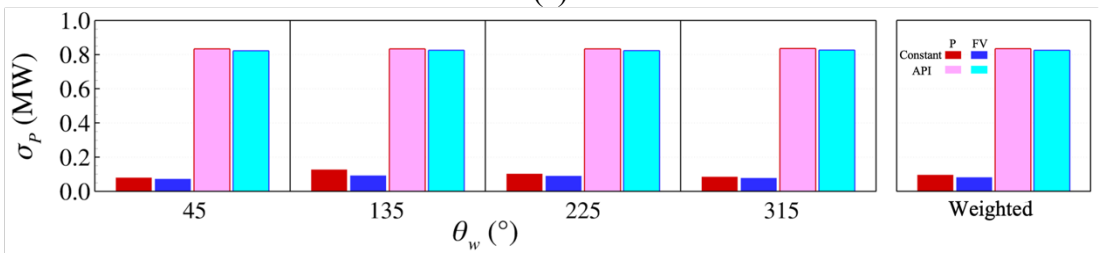

(b)

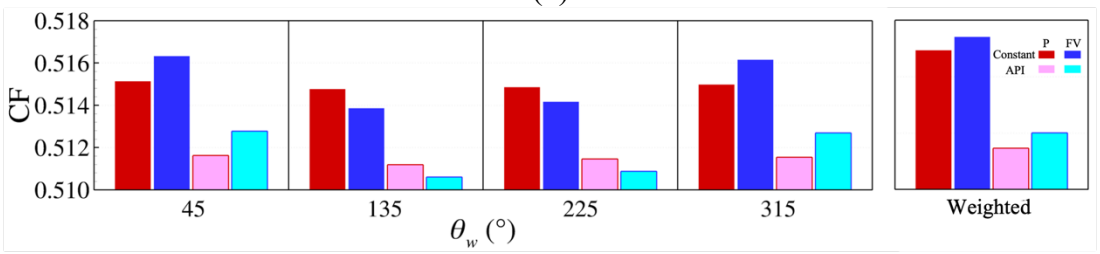

(c)

Figure 44 Power characteristics under LTC scenario: (a) mean, (b) standard deviation, and (c) CF

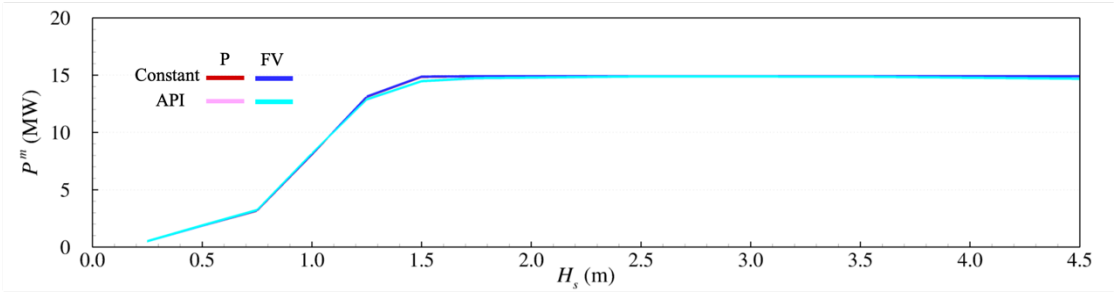

(a)

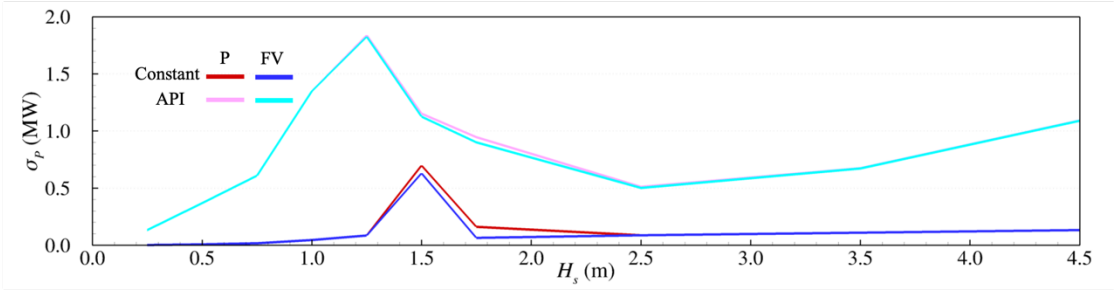

(b)

Figure 45 Dependence of P^m and σ_p on H_s: (a) mean, and (b) standard deviation

doi:10.6342/NTU202403052

Table 19 Power characteristics: (a) mean, and (b) standard deviation

(a)

Spectrum	θ_w	45°	135°	225°	315°	Weighted
Constant (MW)	P	7.727	7.721	7.723	7.725	7.724
	FV	7.745	7.708	7.712	7.742	7.731
API (MW)	P	7.674	7.668	7.672	7.673	7.672
	FV	7.692	7.659	7.663	7.690	7.680

(b)

Spectrum	θ_w	45°	135°	225°	315°	Weighted
Constant (MW)	P	0.080	0.127	0.102	0.086	0.096
	FV	0.073	0.093	0.090	0.078	0.082
API (MW)	P	0.833	0.834	0.834	0.836	0.835
	FV	0.822	0.825	0.823	0.827	0.825

Table 20 Capacity factor CF

Spectrum	θ_w	45°	135°	225°	315°	Weighted
Constant	P	0.515	0.515	0.515	0.515	0.515
	FV	0.516	0.514	0.514	0.516	0.515
API	P	0.512	0.511	0.511	0.512	0.511
	FV	0.513	0.511	0.511	0.513	0.512

Table 21 Dependence of P^m and σ_p on H_s

Wave Height	Mean (MW)				Std (MW)			
	Constant		API		Constant		API	
H_s (m)	P	FV	P	FV	P	FV	P	FV
0.25	0.511	0.512	0.518	0.519	0.002	0.002	0.132	0.132
0.50	1.868	1.870	1.886	1.888	0.008	0.008	0.370	0.370
0.75	3.190	3.194	3.239	3.243	0.018	0.018	0.610	0.608
1.00	8.064	8.076	8.166	8.178	0.046	0.046	1.349	1.348
1.25	13.101	13.127	12.868	12.891	0.085	0.085	1.838	1.826
1.50	14.840	14.863	14.466	14.478	0.698	0.631	1.152	1.126
1.75	14.899	14.897	14.718	14.733	0.161	0.064	0.945	0.901
2.50	14.897	14.897	14.895	14.895	0.087	0.087	0.511	0.501
3.50	14.897	14.897	14.870	14.869	0.110	0.110	0.673	0.672
4.50	14.897	14.897	14.671	14.671	0.134	0.132	1.091	1.090

doi:10.6342/NTU202403052

8.5 Mooring Line Tension

In this study, the mooring line tension is calculated using the finite element method in OrcaFlex. The time-domain results from OrcaFlex provide the mean value (T_i^m), maximum value (T_i^M), and standard deviation (σ_{T_i}).

8.5.1 Comparison of Mooring Line Tension among Methods

The mean, maximum, and standard deviations of the mooring line tension at $\theta_w = 0°$ under CW and EW conditions using various hydrodynamic property prediction methods are depicted in Fig. 46 and Table 22.

For the mooring line tension (T_1), under the CW condition, the mean values, maximum values, and standard deviations of the potential method range from 1.58 MN to 1.661 MN, 1.9 MN to 2.012 MN, and 0.105 MN to 0.114 MN, respectively. The mean values of single-point method and fully viscous method are 1.39% to 1.49% and 1.18% to 1.29% higher than the potential method, respectively. The maximum values are 8.31% to 9% and 3.33% to 3.58% lower than those of potential method, respectively, and the standard deviations are 56.75% to 60.72% and 30.86% to 34.71% lower than those of potential method, respectively. Under the EW condition, the mean values, maximum values, and standard deviations of the potential method range from 1.506 MN to 1.583 MN, 4.706 MN to 5.512 MN, and 0.483 MN to 0.539 MN, respectively. The mean values for single-point method and fully viscous method are 8.31% to 9% and 3.81% to 4.41% lower than those of potential method, respectively. The maximum values are 24.78% to 33.7% and 19.62% to 30.75% lower than those of potential method, respectively, and the standard deviations are 35.08% to 37.72% and 19.28% to 24.28% lower than those of potential method, respectively.

doi:10.6342/NTU202403052

For the tension in mooring line (T_2), under CW conditions, the mean values, maximum values, and standard deviations of the potential method range from 2.232 MN to 2.431 MN, 2.545 MN to 2.929 MN, and 0.092 MN to 0.166 MN, respectively. The mean values of single-point method and fully viscous method are 0.06% to 1.49% lower and 0.05% lower to 1.01% higher than the potential method, respectively. The maximum values are 3.29% to 9.19% and 1.22% to 4.85% lower than those of potential method, and the standard deviations are 29.31% to 49.97% and 12.04% to 25.88% lower than those of potential method, respectively. Under EW conditions, the mean values, maximum values, and standard deviations of the potential method range from 2.357 MN to 2.754 MN, 4.075 MN to 6.588 MN, and 0.348 MN to 0.752 MN, respectively. The mean values of single-point method and fully viscous method are 1.67% to 1.79% and 2.28% to 2.52% lower than those of potential method; the maximum values are 4.94% lower to 0.41% higher and 1.1% to 2.58% lower than those of potential method; and the standard deviations are 23.5% to 32.31% and 16.85% to 31.53% lower than those of potential method, respectively.

For the tension in the mooring line (T_3), under CW conditions, the mean values, maximum values, and standard deviations of the potential method range from 2.222 MN to 2.421 MN, 2.548 MN to 2.954 MN, and 0.085 MN to 0.179 MN, respectively. The mean values of single-point method and fully viscous method are 0.21% to 1.23% and 0.07% to 0.82% higher than the potential method, respectively. The maximum values are 4.55% to 9.32% and 1.83% to 3.83% lower than those of potential method; the standard deviations are 34.57% to 45.1% and 11.6% to 21.17% lower than those of potential method, respectively. Under EW conditions, the mean values, maximum values, and standard deviations of the potential method range from 2.349 MN to 2.764 MN, 4.263 MN to 6.925 MN, and 0.347 MN to 0.77 MN, respectively. The mean values of single-

doi:10.6342/NTU202403052

point method and fully viscous method are 1.08% to 1.5% and 1.86% to 2.02% lower than those of potential method, respectively. The maximum values are 2.24% to 8.31% and 2.08% to 5.85% lower than those of potential method; the standard deviations are 23.55% to 31.02% and 17.57% to 31.24% lower than those of potential method, respectively.

These results indicate a significant correlation between the motion response of the wind turbine platform and the tension of the mooring lines. Greater motion responses increase mooring line tension, particularly during EW conditions. Accounting for viscous effects effectively reduces the motion responses, thereby stabilizing the fluctuations in mooring line tension.

doi:10.6342/NTU202403052

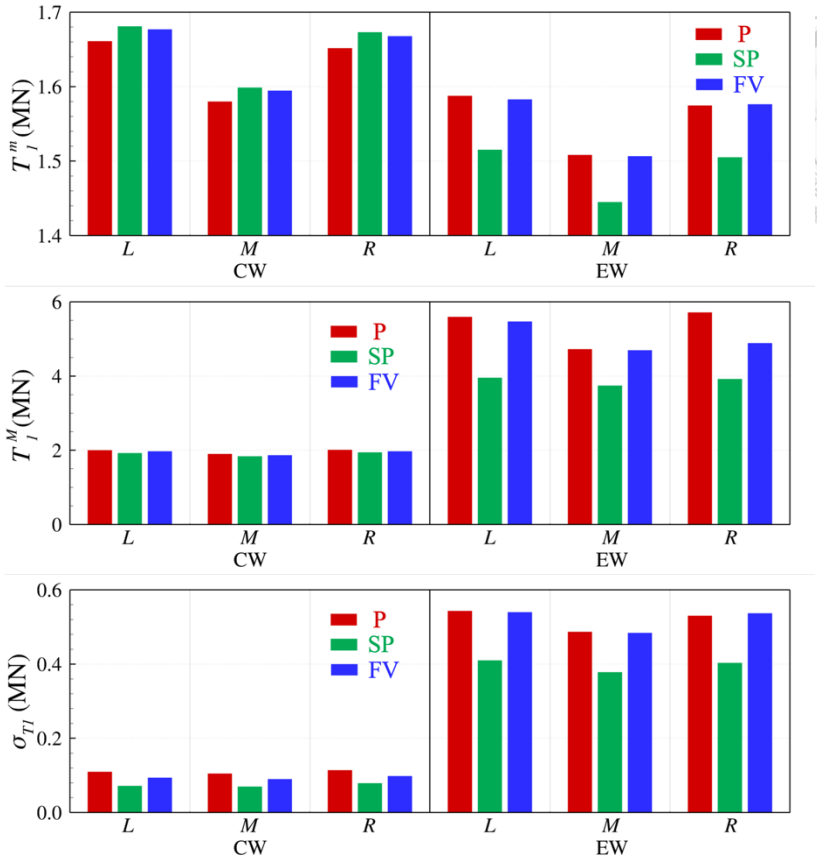

(a)

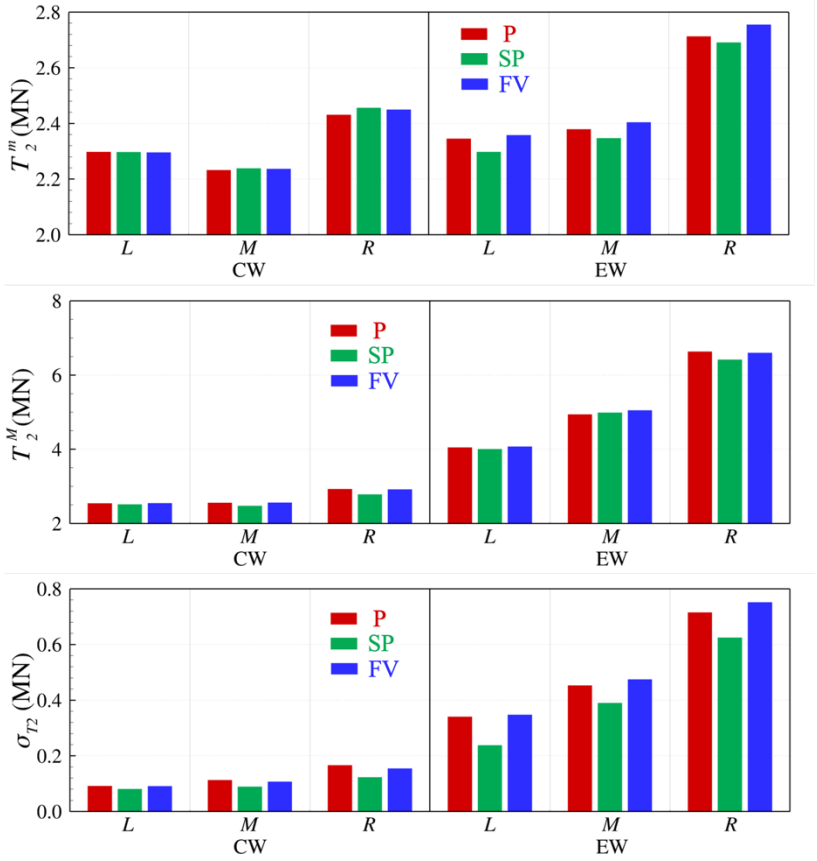

(b)

doi:10.6342/NTU202403052

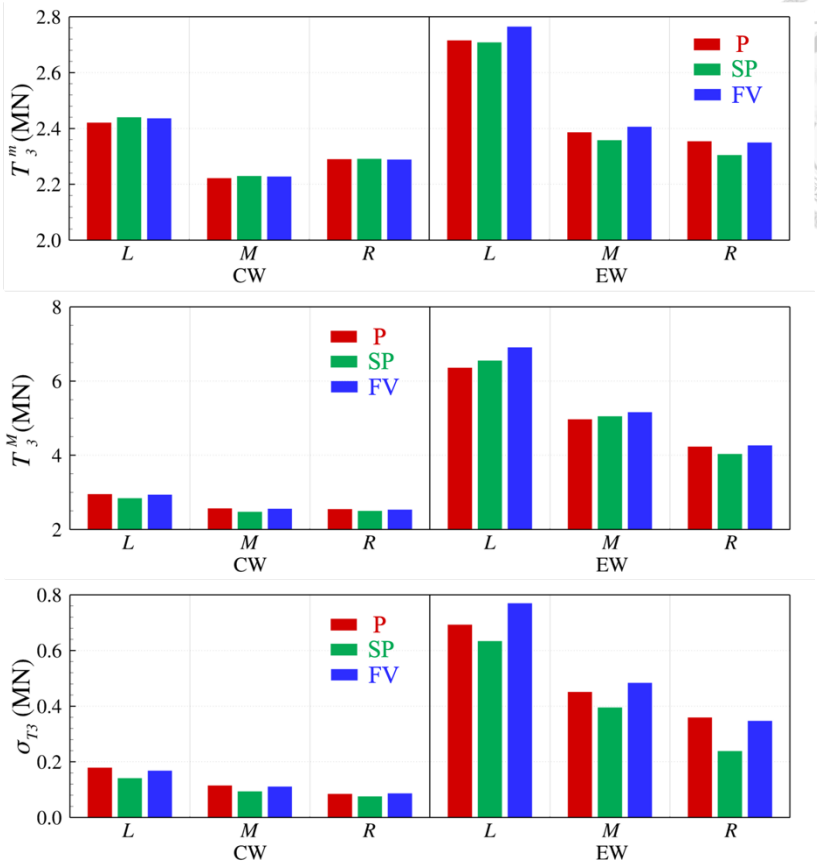

(c)

Figure 46 Mean, maximum, and standard deviation of mooring line tension under CW and EW conditions for (a) T_1, (b) T_2, and (c) T_3

doi:10.6342/NTU202403052

Table 22 Mooring line tension at $\theta_w = 0°$ under CW and EW conditions: (a) T_1, (b) T_2, and (c) T_3

(a)

Tension	Method	Mean (MN)		Max (MN)		Std (MN)	
		CW	EW	CW	EW	CW	EW
$T_{1,L}$	P	1.661	1.583	2.002	5.512	0.110	0.539
	SP	1.685	1.504	1.822	3.654	0.043	0.336
	FV	1.681	1.513	1.925	3.959	0.072	0.408
$T_{1,M}$	P	1.580	1.506	1.900	4.706	0.105	0.483
	SP	1.602	1.430	1.742	3.484	0.043	0.314
	FV	1.599	1.448	1.837	3.259	0.070	0.389
$T_{1,R}$	P	1.652	1.576	2.012	4.886	0.114	0.535
	SP	1.676	1.489	1.831	3.675	0.049	0.335
	FV	1.673	1.506	1.944	3.927	0.079	0.405

(b)

Tension	Method	Mean (MN)		Max (MN)		Std (MN)	
		CW	EW	CW	EW	CW	EW
$T_{2,L}$	P	2.298	2.357	2.545	4.075	0.092	0.348
	SP	2.299	2.315	2.461	4.092	0.065	0.235
	FV	2.297	2.298	2.514	4.005	0.081	0.238
$T_{2,M}$	P	2.232	2.403	2.558	5.045	0.113	0.475
	SP	2.242	2.363	2.415	4.982	0.066	0.363
	FV	2.239	2.347	2.478	4.989	0.089	0.390
$T_{2,R}$	P	2.431	2.754	2.929	6.588	0.166	0.752
	SP	2.467	2.705	2.659	6.262	0.083	0.565
	FV	2.456	2.691	2.786	6.418	0.123	0.626

(c)

Tension	Method	Mean (MN)		Max (MN)		Std (MN)	
		CW	EW	CW	EW	CW	EW
$T_{3,L}$	P	2.421	2.764	2.954	6.925	0.179	0.770
	SP	2.451	2.723	2.679	6.343	0.098	0.575
	FV	2.440	2.709	2.841	6.519	0.141	0.634
$T_{3,M}$	P	2.222	2.405	2.568	5.159	0.115	0.484
	SP	2.234	2.376	2.395	5.044	0.067	0.370
	FV	2.230	2.358	2.479	5.052	0.094	0.395
$T_{3,R}$	P	2.290	2.349	2.548	4.263	0.085	0.347
	SP	2.294	2.324	2.432	4.128	0.056	0.239
	FV	2.291	2.305	2.501	4.034	0.076	0.239

doi:10.6342/NTU202403052

8.5.2 LTC Scenario

The maximum values and standard deviations of mooring line tension under LTC scenario are compared between spectrums, as well as the impact of viscous effects, as shown in Fig. 47 and Table 23.

For mooring line tension (T_1), concerning the maximum value, comparing between spectrums reveal that using the potential method, API values are 1.48% to 16.08% larger than those of constant wind speed, while when using the fully viscous method, API values are1.23% to 9.67% larger than those of constant wind speed. When comparing the potential method and fully viscous method under the constant wind speed, the fully viscous method values are 4.64% smaller to 0.55% larger than those of potential method, while under API, the fully viscous method values are 5.8% smaller to 0.9% larger than those of potential method. For the standard deviations are consistently higher for API compared to constant wind speed, and for potential method compared to fully viscous method.

For mooring line tension (T_2), concerning the maximum value, comparing between spectrums reveal that using the potential method, API values are 0.49% to 8.54% larger than those of constant wind speed, while when using the fully viscous method, API values 1.27% to 10.55% larger than those of constant wind speed. When comparing the potential method and fully viscous method under the constant wind speed, the fully viscous method values are 1.28% smaller to12.39% larger than those of potential method, while under API, the fully viscous method values are 9.93% smaller to 0.09% larger than those of potential method. For the standard deviations are consistently higher for API compared to constant wind speed, and for potential method compared to fully viscous method.

doi:10.6342/NTU202403052

For mooring line tension (T_3), concerning the maximum value, comparing between spectrums reveal that using the potential method, API values are 0.58% to 11.7% larger than those of constant wind speed, while when using the fully viscous method, API values 1.29% to 9.13% larger than those of constant wind speed. When comparing the potential method and fully viscous method under the constant wind speed, the fully viscous method values are 5.17% smaller to 0.17% larger than those of potential method, while under API, the fully viscous method values are 0.24% to 8.11% smaller than those of potential method. For the standard deviations are consistently higher for API compared to constant wind speed, and for potential method compared to fully viscous method.

The findings indicate that the API spectrum, with its time-varying wind speeds, causes greater instability in motion response, leading to higher maximum values and standard deviations in mooring line tensions compared to constant wind speed. This highlights the importance of accounting for actual wind spectra in the design and analysis of offshore structures. Furthermore, incorporating viscous effects tends to reduce platform motions and mooring line tensions compared to potential flow models. Although these reductions are modest, they contribute to improved fatigue performance.

doi:10.6342/NTU202403052

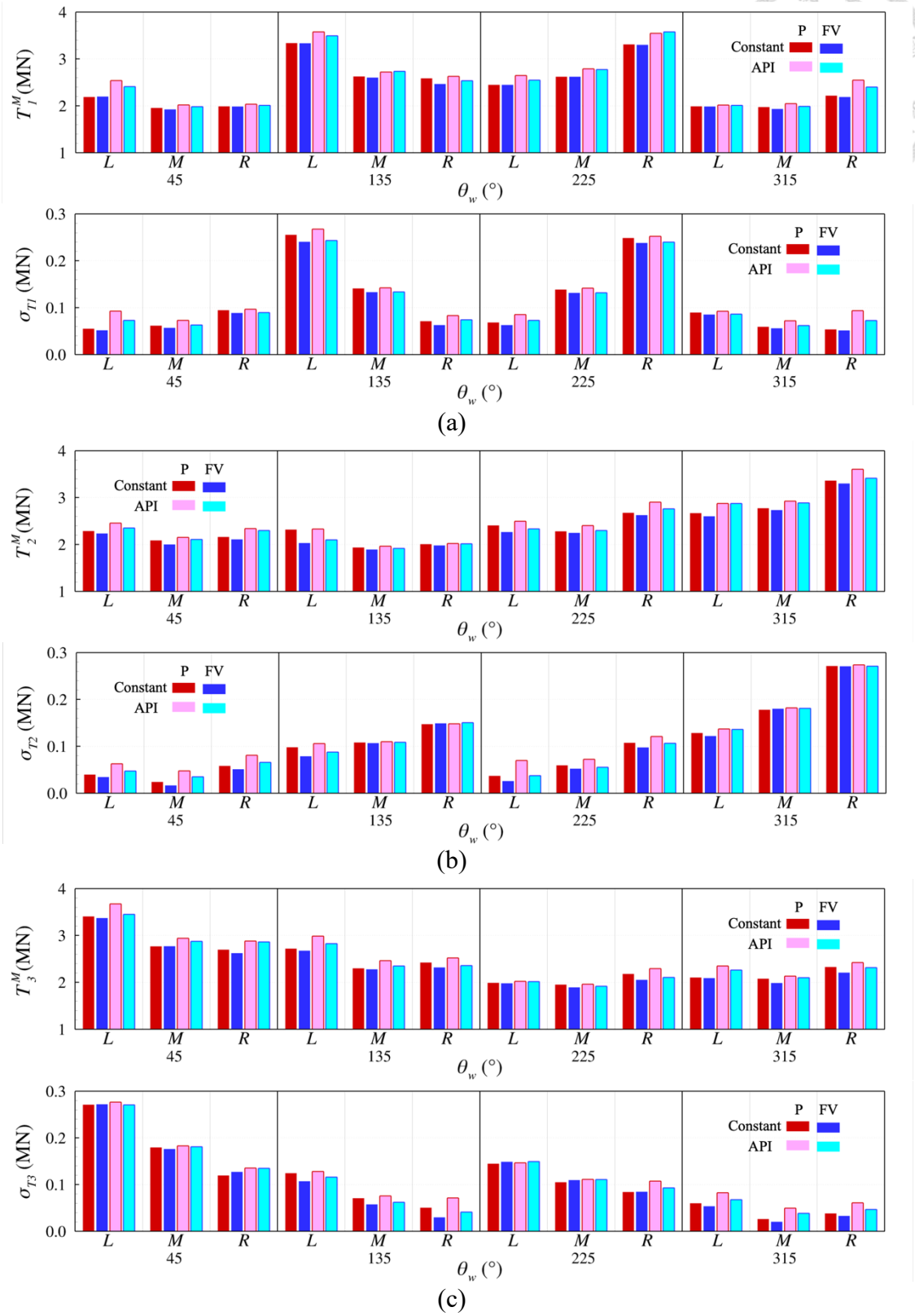

Figure 47 Maximum and standard deviation of mooring line tension under LTC scenario:(a) T_1, (b) T_2, and (c) T_3

doi:10.6342/NTU202403052

Table 23 Mooring line tension under LTC scenario: (a) T_1, (b) T_2, and (c) T_3

(a)

Tension	Spectrum		Max (MN)				Std (MN)			
		θ_w	45°	135°	225°	315°	45°	135°	225°	315°
$T_{1,L}$	Constant	P	2.187	3.338	2.446	1.988	0.055	0.255	0.068	0.090
		FV	2.199	3.332	2.447	1.985	0.052	0.241	0.063	0.085
	API	P	2.539	3.578	2.648	2.017	0.093	0.267	0.085	0.092
		FV	2.411	3.493	2.550	2.010	0.073	0.243	0.073	0.086
$T_{1,M}$	Constant	P	1.955	2.624	2.620	1.972	0.061	0.141	0.139	0.059
		FV	1.923	2.601	2.620	1.932	0.057	0.133	0.131	0.056
	API	P	2.018	2.721	2.789	2.048	0.073	0.142	0.142	0.072
		FV	1.984	2.736	2.774	1.987	0.063	0.134	0.132	0.062
$T_{1,R}$	Constant	P	1.988	2.584	3.308	2.216	0.094	0.071	0.249	0.053
		FV	1.985	2.464	3.300	2.188	0.089	0.063	0.238	0.051
	API	P	2.035	2.629	3.545	2.547	0.097	0.083	0.252	0.093
		FV	2.011	2.537	3.577	2.400	0.090	0.074	0.240	0.073

(b)

Tension	Spectrum		Max (MN)				Std (MN)			
		θ_w	45°	135°	225°	315°	45°	135°	225°	315°
$T_{2,L}$	Constant	P	2.287	2.318	2.407	2.669	0.040	0.098	0.037	0.128
		FV	2.234	2.031	2.267	2.602	0.034	0.079	0.026	0.122
	API	P	2.456	2.330	2.496	2.874	0.063	0.106	0.070	0.137
		FV	2.351	2.098	2.332	2.876	0.047	0.088	0.038	0.136
$T_{2,M}$	Constant	P	2.088	1.935	2.280	2.772	0.024	0.108	0.059	0.178
		FV	2.002	1.894	2.246	2.735	0.017	0.107	0.052	0.180
	API	P	2.150	1.964	2.403	2.923	0.048	0.110	0.072	0.182
		FV	2.108	1.919	2.301	2.886	0.035	0.109	0.055	0.181
$T_{2,R}$	Constant	P	2.160	2.005	2.674	3.362	0.058	0.147	0.107	0.271
		FV	2.108	1.980	2.626	3.301	0.051	0.149	0.098	0.270
	API	P	2.340	2.023	2.902	3.604	0.081	0.148	0.121	0.274
		FV	2.300	2.016	2.762	3.413	0.066	0.150	0.107	0.271

doi:10.6342/NTU202403052

(c)

Tension	Spectrum		Max (MN)				Std (MN)			
		θ_w	45°	135°	225°	315°	45°	135°	225°	315°
$T_{3,L}$	Constant	P	3.405	2.718	1.988	2.101	0.271	0.125	0.145	0.060
		FV	3.372	2.675	1.980	2.089	0.272	0.107	0.149	0.054
	API	P	3.673	2.986	2.021	2.347	0.276	0.128	0.147	0.083
		FV	3.450	2.825	2.016	2.262	0.271	0.116	0.149	0.068
$T_{3,M}$	Constant	P	2.767	2.298	1.951	2.077	0.179	0.071	0.105	0.026
		FV	2.771	2.279	1.894	1.984	0.176	0.057	0.109	0.020
	API	P	2.939	2.464	1.962	2.133	0.183	0.076	0.111	0.049
		FV	2.875	2.348	1.919	2.099	0.181	0.062	0.111	0.038
$T_{3,R}$	Constant	P	2.696	2.423	2.178	2.328	0.119	0.051	0.084	0.038
		FV	2.623	2.317	2.053	2.206	0.127	0.030	0.085	0.033
	API	P	2.883	2.520	2.292	2.424	0.135	0.072	0.107	0.061
		FV	2.862	2.356	2.106	2.314	0.135	0.041	0.093	0.047

doi:10.6342/NTU202403052

9 Conclusions

This study aims to evaluate the performance of a 15MW FOWT system, which includes a semi-submersible TaidaFloat platform and an IEA 15MW offshore wind turbine, using a 3×3 mooring configuration of the Hsinchu offshore area. It analyzes variations in motion response and power characteristics across different hydrodynamic property prediction methods and calculates the weighted capacity factor. Initially, the study compares the hydrodynamic property derived from the potential method (P) and two viscous methods (SP and FV). Under single wind (wave) direction conditions, it examines differences in motion response, generator power, and mooring line tension using two hydrodynamic property prediction methods across two metocean conditions (CW and EW). The analysis includes the mean, maximum, and standard deviation values for six cases. Additionally, the study compiles a wave scatter diagram for the Hsinchu offshore area to predict the maximum and standard deviation of motion response during normal operation. It also estimates the weighted capacity factor, considering 31 wave conditions, four wind (wave) directions, two hydrodynamic property prediction methods, and two wind spectrums. The conclusions of this study are as follows:

1. Hydrodynamic property prediction method: The FV method reveals significant viscous effects on damping to added mass, as well as heave, roll, and pitch motions compared to surge, sway, and yaw. Viscous effects are more pronounced at low frequencies for added mass and at high frequencies for damping. The hydrodynamic properties curves obtained using the FV method indicate varying contributions of viscous effects across different frequencies.
2. CW condition: Comparison among hydrodynamic property prediction methods, the maximum motion response values using the SP and FV methods are 30.3% and

doi:10.6342/NTU202403052

13.3% lower than those using the potential method, indicating an underestimation by the SP method and revealing that motion magnitude is related to damping at the wave spectral density peak under specific metocean conditions. Power performance shows that the average values using the SP and FV methods are 0.3% and 0.2% higher than those using the potential method, indicating minimal viscous effects on power characteristics. The maximum mooring line tensions obtained from the SP and FV methods are 9.3% and 3.8% lower than those from the potential method, respectively, highlighting a correlation between tension magnitude and motion response magnitude. It demonstrates the importance of viscous effects in the calculation of FOWT systems.

3. EW condition: Comparison among hydrodynamic property prediction methods using the potential, SP and FV methods. The maximum offsets are 9.088 m, 7.839 m, and 8.293 m, respectively, both decreased significantly after considering the viscosity effect, and all within the acceptable range of less than 30% of the water depth (21 m).
4. Mooring line tension under EW condition: The maximum mooring line tensions obtained are 6.925 MN, 6.343 MN, and 6.519 MN for the potential, SP and FV methods, respectively, both decreased significantly after considering the viscosity effect, corresponding to 27.2%, 24.9%, and 25.6% of the break load. The safety factors are 3.68, 4.02, and 3.91, respectively, all meeting the requirement of a safety factor greater than 1.67.
5. LTC scenario: For motion response, the maximum value is 20% higher when using the API spectrum compared to constant wind speed, with the potential method exceeding the FV method by 3.15%. The standard deviation is higher for heave and roll motion with the FV method compared to the potential method. Power shows a

doi:10.6342/NTU202403052

mean value of 0.67% lower with the API spectrum compared to constant wind speed, and the potential method is 0.1% lower than the FV method, with negligible differences. The standard deviation for power is higher with the API spectrum and the potential method compared to constant wind speed and the FV method. For mooring line tension, the maximum value is 5.29% higher with the API spectrum compared to constant wind speed, and the potential method shows a 2.53% higher value than the FV method. The standard deviation is also higher with the API spectrum and the potential method compared to constant wind speed and the FV method. It shows that under normal operation, reasonable wind spectrum selection is more important than viscous effects. Furthermore, while the inclusion of viscous effects generally results in a reduction of platform motions and mooring line tensions compared to potential flow models, these modest reductions still play a significant role in enhancing the fatigue performance of the system.

6. Power characteristics: Using the TaidaFloat with the IEA 15 MW wind turbine, the API spectrum, and the FV methods, the weighted power output is 7.68 MW, with a standard deviation of 0.83 MW. This corresponds to a weighted capacity factor of 0.512, which is close to the theoretical power output, with a difference of 1.8%, showing that to roughly estimate power output, theoretical values can be used.

doi:10.6342/NTU202403052

References

[1] "Annual Report 2023: Record year for windpower in 2023," World Wind Energy Association, 2023.

[2] Zheng, C. W., Xiao, Z. N., Peng, Y. H., Li, C. Y., and Du, Z. B., "Rezoning Global Offshore Wind Energy Resources," *Renewable Energy*, vol. 129, pp. 1-11, 2018.

[3] Chang, P. C., Yang, R. Y., and Lai, C. M., "Potential of Offshore Wind Energy and Extreme Wind Speed Forecasting on the West Coast of Taiwan," *Energies*, vol. 8, no. 3, pp. 1685-1700, 2015.

[4] "The Taiwan Wind Energy Assessment Manual," Green Energy and Environment Research Laboratories ITRI, 2011.

[5] Hsu, I. J., Ivanov, G., Ma, K. T., Huang, Z. Z., Wu, H. T., Huang, Y. T., and Chou, M., "Optimization of Semi-Submersible Hull Design for Floating Offshore Wind Turbines," presented at the 41st International Conference on Ocean, Offshore and Arctic Engineering, Hamburg, Germany, June, 2022.

[6] Bilgili, M., Yasar, A., and Simsek, E., "Offshore Wind Power Development in Europe and Its Ccomparison with Onshore Counterpart," *Renewable and Sustainable Energy Reviews*, vol. 15, no. 2, pp. 905-915, 2011.

[7] Nikolaos, N., "Deep Water Offshore Wind Technologies", Master's thesis, Dept. Mechanical Engineering, University of Strathclyde, Glasgow, Scotland, 2004.

[8] Barltrop, N., "Multiple Unit Floating Offshore Wind Farm (MUFOW)," *Wind Engineering*, pp. 183-188, 1993.

[9] Henderson, A. R. and Patel, M. H., "Floating Offshore Wind Energy," 20th BWEA Conference, London, UK, 1998.

[10] Tong, K. C., "Technical and Economic Aspects of a Floating Offshore Wind Farm," *Journal of Wind Engineering and Industrial Aerodynamics*, vol. 74, pp. 399-410, 1998.

[11] Castro-Santos, L. and Diaz-Casas, V., Eds. *Floating Offshore Wind Farms.* Berlin/Heidelberg, Germany, 2016.

[12] Lee, Y. J., Ho, C. Y., Huang, Z. Z., and Wang, Y. C., "Improvements on the Output of a Spar-Type Floating Wind Turbine Influenced by Wave-Induced Oscillation," *Journal of Taiwan Society of Naval Architects and Marine Engineers*, vol. 34, no. 2, pp. 55-62, 2015.

[13] Huang, Z. Z., "Dynamic Response of Floating Offshore Wind Turbine," Master's thesis, Dept. Engineering Science and Ocean Engineering, National

doi:10.6342/NTU202403052

Taiwan University, Taipei, Taiwan, 2013.

[14] Wang, Y. C., "Motion Characteristics and Power Evaluation on Floating Offshore Wind Turbine," Master's thesis, Dept. Engineering Science and Ocean Engineering, National Taiwan University, Taipei, Taiwan, 2011.

[15] Li, B., Liu, K., Yan, G., and Ou, J., "Hydrodynamic Comparison of a Semi-Submersible, TLP, and Spar: Numerical Study in the South China Sea Environment," *Journal of Marine Science and Application*, vol. 10, no. 3, pp. 306-314, 2011.

[16] Jonkman, J., Butterfield, S., Musial, W., and Scott, G., "Definition of a 5-MW Reference Wind Turbine for Offshore System Development," National Renewable Energy Lab, Golden, CO, USA, NREL/TP-500-38060, 2009.

[17] Bak, C., Zahle, F., Bitsche, R., Kim, T., Yde, A., Henriksen, L. C., Hansen, M. H., Blasques, J. P. A. A., Gaunaa, M., and Natarajan, A., "The DTU 10-MW Reference Wind Turbine," Dept. Wind Energy, Technical University of Denmark, 2013.

[18] Gaertner, E., Rinker, J., Sethuraman, L., Zahle, F., Anderson, B., Barter, G., Abbas, N., Meng, F., Bortolotti, P., Skrzypinski, W., Scott, G., Feil, R., Bredmose, H., Dykes, K., Shields, M., Allen, C., and Viselli, A., "Definition of the IEA Wind 15-Megawatt Offshore Reference Wind Turbine," National Renewable Energy Lab, Golden, CO, USA, NREL/TP-5000-75698, 2020.

[19] Chen, C. Y., "Comparative Study on Semi-Submersible Floating Platforms for Offshore Wind in Taiwan Strait," Master's thesis, Dept. Engineering Science and Ocean Engineering, National Taiwan University, Taipei, Taiwan, 2020.

[20] Hong, J. J., "Performance Prediction of a Disk-Type Semi-Submersible Floating Platform in Taiwan Strait," Master's thesis, Dept. Engineering Science and Ocean Engineering, National Taiwan University, Taipei, Taiwan, 2022.

[21] Kou, C. L., "Comparative Study of Three Semi-Submersible Platform Designs on Normal Operating Performance of 13.2 MW Floating Wind Turbine in the Hsinchu Offshore Area," Master's thesis, Dept. Engineering Science and Ocean Engineering, National Taiwan University, Taipei, Taiwan, 2022.

[22] Tong, H. Y., "Normal Operating Performance Study of a 15 MW Floating Wind Turbine System Using Semi-Submersible TaidaFloat Platform in the Hsinchu Offshore Area," Master's thesis, Dept. Engineering Science and Ocean Engineering, National Taiwan University, Taipei, Taiwan, 2022.

[23] Cai, Y. S., "Normal Operating and Extreme Condition Performance Study of 15MW Floating Wind Turbine System Using Semi-Submersible Taida Floating Platform with 3×2 and 3×3 Mooring Design in the Hsinchu Offshore Area," Master's thesis, Dept. Engineering Science and Ocean Engineering, National Taiwan University, Taipei, Taiwan, 2023.

doi:10.6342/NTU202403052

[24] *Coupled Analysis of Floating Wind Turbines*, DNVGL-RP-0286, DNV GL, Olso, Norway, 2019.

[25] *Harnessing offshore mooring experience and anchoring technology for the floating renewable energy systems*, Vryhof Anchors B.V., 2020. [Online] Available:https://www.kivi.nl/uploads/media/5ae711f5178c0/SOZKIVI%20-lecture%20-%20Anchoring%20Technologies%20for%20FOWT%20by%20Vry- of%20Anchors.pdf

[26] Ikhennicheu, M., Lynch, M., Doole, S., Borisade, F., Matha, D., Dominguez, J. L., Vicente, R. D., Habekost, T., Ramirez, L., Potestio, S., Molins, C., and Trubat, P., *Review of the State of the Art of Mooring and Anchoring Designs, Technical Challenges and Identification of Relevant DLCs*, CoreWind Project, Barcelona, Spain, Tech. Rep. 815083, 2020.

[27] Gaertner, E., Rinker, J., Sethuraman, L., Zahle, F., Anderson, B., Barter, G. E., ... & Viselli, A., "Definition of the IEA Wind 15 Megawatt Offshore Reference Wind Turbine," National Renewable Energy Lab., Golden, CO, USA, Tech. Rep. TP-5000-75698, 2020.

[28] Haskind, M. D., "The Oscillation of a Ship in Still Water," *Izv. Akad. Nauk SSSR, Otd. Tekh. Nauk*, vol. 1, pp. 23-34, 1946.

[29] Haskind, M. D., "The Hydrodynamic Theory of Ship Oscillations in Rolling and Pitching," *Prikl. Mat. Mekh*, vol. 10, pp. 33-66, 1946.

[30] Wehausen, J. V. and Laitone, E. V., "Surface Waves in Fluid Dynamics III," *Handbuch der Physik*, vol. 9, no. 3, pp. 446-778, 1960.

[31] Simcenter STAR-CCM+ User Guide, ver. 2206, Siemens, Berlin, Germany, 2023.

[32] Boussinesq, J., "Essai sur la Théorie des Eaux Courantes," *Mémoires Présentés par Divers Savants à l'Académie des Sciences*, vol. 23, no. 1, pp. 1-680, 1877.

[33] Hirt, C. W. and B. D. Nichols, "Volume of Fluid Method for the Dynamics of Free Surface," *Journal of Computational Physics*, vol. 39, pp. 201-225, 1981.

[34] Goldstein, S., "On the Vortex Theory of Screw Propellers," Proceedings of the Royal Society of London. Series A, Containing Papers of a Mathematical and Physical Character, vol. 123, no. 792, pp. 440-465, 1929.

[35] Hansen, M. H., Hansen, A., Larsen, T. J., Øye, S., Sørensen, P., and Fuglsang, P., "Control Design for a Pitch-Regulated, Variable Speed Wind Turbine," Risø National Laboratory, Roskilde, Danmark, RISØ-R-1500(EN), 2005.

[36] OrcaFlex Documentation Version 11.4a, Orcina, UK, 2023.

doi:10.6342/NTU202403052

[37] Chen, T. L., Lee, C. I., Lin, T, Y., "Experiment on Hydrodynamic properties of Semi-Submersible Floating Platform," presented at the 36th SNAME, Kaohsiung, 2024.

[38] "Data Bouy Observation Data Annual Report 2011-2020," Central Weather Bureau, 2011-2020.

[39] Chuang, T. C., Yang, W. H., and Yang, R. Y., "Experimental and Numerical Study of a Barge-Type FOWT Platform under Wind and Wave Load," *Ocean Engineering*, vol. 230, pp. 109015, 2021.

[40] Baniotopoulos, C., Borri, C. and Stathopoulos, T. *Environmental wind engineering and design of wind energy structures*. Springer Science & Business Media, 2011.

[41] Ghafari, H. and Dardel, M., "Parametric study of catenary mooring system on the dynamic response of the semi-submersible platform," *Ocean Engineering*, vol. 153, no. 3, pp. 319-332, 2018.

[42] "World Meteorological Organization Manual on Codes Volume I.1 Annex II to the WMO Technical Regulations Part A – Alphanumeric Codes" edition, section E, pp. 379, 2019.

doi:10.6342/NTU202403052